DIPLOMARBEIT

Implementation of emittance and transmission measurement and analysis procedures along the MedAustron accelerator

zur Erlangung des akademischen Grades

Diplom-Ingenieur

im Rahmen des Studiums

Masterstudium Biomedical Engineering

eingereicht von

Laurids ADLER, BSC
Matrikelnummer 01325910

ausgeführt am **E141 - Atominstitut**, Stadionallee 2, 1020 Wien
der Technischen Universität Wien

in Kollaboration mit **EBG MedAustron GmbH**, Marie Curie-Strasse 5, 2700 Wiener Neustadt

unter der Betreuung von
Ao.Univ.Prof. Dipl.-Ing. Dr.techn. Christina STRELI
Dipl.-Ing. Dr.techn. Christoph KURFÜRST (MedAustron)

6. Dezember 2018

(Unterschrift Verfasser)

(Unterschrift Betreuerin)

Abstract

MedAustron is an ion therapy and research center situated in Wr. Neustadt, Lower Austria. The facility features a synchrotron based accelerator, which allows to provide proton beams in the range of 62-800 MeV and carbon ion beams in the range of 120-400 MeV/n. As of 2018 the commissioning of three horizontal beam lines (two for treatment, one for research) and the vertical beam line is finished for protons while the commissioning process for carbon ions is ongoing.

The volume a beam of charged particles occupies in the phase space can be described by its emittance. Measurement and control of the beam emittance is crucial for successful particle therapy, since the emittance is a major defining parameter for the spot size of the beam at the isocenter. By defining the betatron amplitudes of the particles, it also plays an important role in the setup of the third order resonant extraction used at MedAustron. Additionally the emittance needs to be matched between the different parts of the accelerator and the transfer lines. It therefore has a strong influence on the transmission efficiency of the charged particles which in turn plays an important role in the efficiency of the dose delivery to the patient.

In this thesis multiple measurement and analysis procedures to obtain the emittance and transmission through the various stages of the accelerator have been implemented. The specialized analysis tools were written in Python and developed inside MedAustron's dedicated measurement analysis framework. A special focus has been set on the characterization of the developed analysis tools to understand the achievable accuracy in emittance reconstruction. The used procedures for the emittance measurement are: slit-grid method in the Injector, quadrupole tuning in the medium and high energy beam transfer lines and emittance reconstruction via the insertion of copper scraper plates in the synchrotron. The transmission is measured via several current transformers for pulsed and continuous beam. The usability of the developed tools has been proven during the commissioning of the carbon ion beam, as well as for repetitive beam parameter measurements of the proton beam.

Acknowledgments

First and foremost I would like to thank Prof. Christina Streli and Dr. Albert Hirtl of TU Vienna for supervising this thesis. Special thanks go to Christoph Kurfürst for supervision, support, guidance and countless fruitful, pleasant, motivating and instructive discussions and to Alexander Wastl for numerous tips on programming with Python and the PACMAN framework, as well as his expertise with MADX and the hunt for the elusive bar of charge. I would furthermore like to thank all other members of MedAustron's accelerator group (in alphabetical order): Andrea De Franco, Fabio Farinon, Nadia Gambino, Greta Guidoboni, Szymon Myalski, Mauro Pivi, Claus Schmitzer and Ivan Strasik who made my first steps into the world of accelerator physics not only educational but also very enjoyable. Last but not least I would like to thank EBG MedAustron GmbH for the opportunity to conduct this thesis.

Contents

Acronyms

CNAO	Centro Nazionale di Adroterapia Oncologica
CTA	Current transformer
CTS	Current transformer synchrotron (for DC measurements)
DC	Direct Current
DDS	Dose Delivery System
ECR	Electron Cyclotron Resonance
FWHM	Full Width at Half Maximum
HEBT	High Energy Beam Transfer
IRx	Irradiation Room x
LEBT	Low Energy Beam Transfer
LINAC	LINear ACcelerator
MAPTA	MedAustron Particle Therapy Accelerator
MEBT	Medium Energy Beam Transfer
MR	Main Ring
OpApp	Operational Application
PACMAN	Python Algorithms Coded for Measurement data ANalysis
PGX	Profile Grid Monitor
PIMMS	Proton Ion Medical Machine Study
PU	Pick-Up
RFQ	Radio Frequency Quadrupole
RMS	Root Mean Square
SEM	Secondary Electron EMission
SFX	Scintillating Fibre Hodoscope
SLC	Synchrotron Low level RF Cavity

Introduction

The goal of this thesis was the implementation of measurement and analysis procedures to reconstruct the particle beam emittance in the MedAustron synchrotron and the transfer lines, as well as to obtain the transmission of the beam intensity, which is closely related to the emittance, through the different sections of the accelerator. Since the emittance is decisive for the spot size of the beam at the isocenter and the transmission has a direct impact on the delivered dose and therefore also treatment times, the measurement and control of these beam properties is of utmost importance for the successful treatment of patients with ion therapy. The measurement analysis tools have been developed alongside the ongoing commissioning of the carbon ion beam and were extensively used during this whole time. The analysis procedures were also thoroughly tested and characterized with simulated data.

The thesis is structured as follows: in chapter 1 selected topics of accelerator physics, which were relevant to this thesis, will be presented including an introduction into the concept of the particle phase space and emittance. Chapter 2 will give an overview over the MedAustron facility, including design beam properties followed by a description of the used beam diagnostic devices and monitors in chapter 3. In chapter 4 the ideas and physics behind the used emittance and transmission measurement concepts will be presented. Chapter 5 covers the description of the developed analysis tools and algorithms, as well as testing of the tools with simulated data. In chapter 6 the main measurement analysis results will be presented.

1 Accelerator Physics

In this chapter some basics of accelerator physics will be presented. This should in no means represent a complete derivation of the topics presented here. Much more in-depth information can be found in the books of Wiedemann [1], Lee [2] and Bryant and Johnsen [3], out of which most information in this chapter is taken.

1.1 Introduction

A synchrotron is a ring-shaped accelerator, comprised of magnetic and electric components, which guide a beam of charged particles within a vacuum chamber. A particle trajectory in a synchrotron that closes on itself after a complete revolution is called a *closed orbit*. The orbit of the particles, defined by the elements of the synchrotron lattice (dipoles, quadrupoles, sextupoles, ...) is called the *reference orbit* and a particle following the reference orbit is referred to as the *reference particle*.

The design of a synchrotron can be such, that the particles should follow a different closed orbit, referred to as the *design orbit*. The particle following this defined path is referred to as the *design particle*.

At MedAustron the particles follow a trajectory which is closer to the center of the synchrotron than the center of the vacuum pipe. This means that the particles have a lower energy than the reference particle and therefore this mode of operation is referred to as *off-momentum* operation. The reason for this chosen mode of operation lies in the used extraction method explained in Sec. 1.3.2.

In a synchrotron a charged particle is subject to the Lorentz force:

$$\vec{F} = q \cdot \left(\vec{E} + \vec{v} \times \vec{B}\right)$$

with the charge of the particle q (in the following always assumed to be positive), the velocity v, electrical field $\vec{E}$ and the magnetic field $\vec{B}$. On the reference orbit there is an equilibrium between Lorentz (without acceleration only contribution from magnetic fields) and centrifugal force:

$$qvB = -\frac{\gamma_{rel} m_0 v^2}{\rho} \tag{1.1}$$

with the Lorentz factor γ_{rel}, the rest mass of the particle m_0 and the radius of curvature of the reference orbit ρ. Rearranging this equation with the definition of the relativistic momentum $p = \gamma m_0 v$ one obtains the definition of the so called *beam rigidity* $B\rho$:

$$B\rho = \frac{p}{|q|} \tag{1.2}$$

From this equation the name-giving property of the synchrotron can be seen, namely that in order to keep the orbit radius stable, the B-field needs to be increased synchronously with increasing particle momentum.

1.1.1 Coordinate system and magnetic field sign conventions [4]

The MedAustron accelerator complex uses the MAD-X[1] coordinate system. It is a local curvilinear right handed coordinate system (x, y, s) where the local s-axis is the tangent to the reference orbit. The other two axes are normal to the reference orbit and are labelled x (in the bending plane) and y (perpendicular to the bending plane). The used coordinate system is shown in Fig. 1.1.

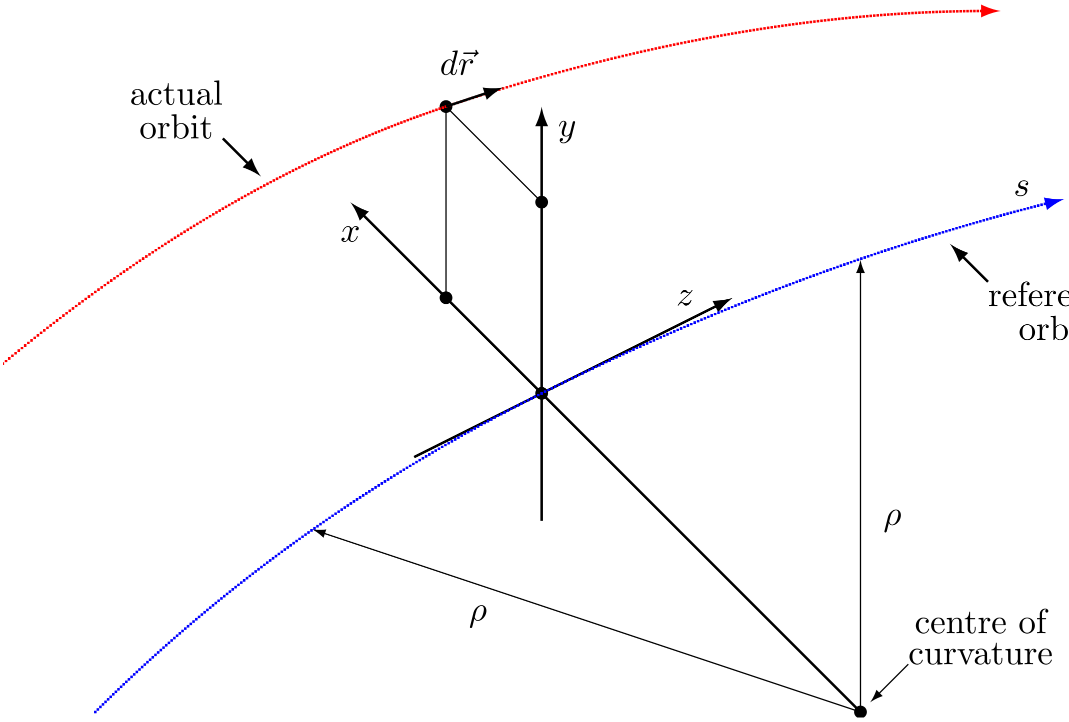

Figure 1.1: MAD-X coordinate system. Source: Grote and Schmidt [4] page 11.

A dipole field B_0 with a positive value in the positive y direction bends a positively charged particle to the right. A positive value of the quadrupole coefficient $B_1 = (\partial B_y / \partial x)$ corresponds to horizontal focusing of a positively charged particle.

1.2 Transverse beam dynamics

This section is besides the books of Wiedemann [1], Lee [2] and Bryant and Johnsen [3] also based on the works of Holzer [5].

While dipole magnets keep the beam on its closed orbit, quadrupole magnets are used to exert focusing forces on the particles to keep their trajectories close to the ideal orbit. This can be achieved by the linearly, with distance from the center, increasing field of the quadrupoles:

$$B_y = gx \quad \text{and} \quad B_x = gy$$

---

[1] The MAD (Methodical Accelerator Design) program is a general-purpose tool for charged-particle optics design and studies in alternating-gradient accelerators and beam lines [4].

where g is the gradient of the quadrupole magnet.

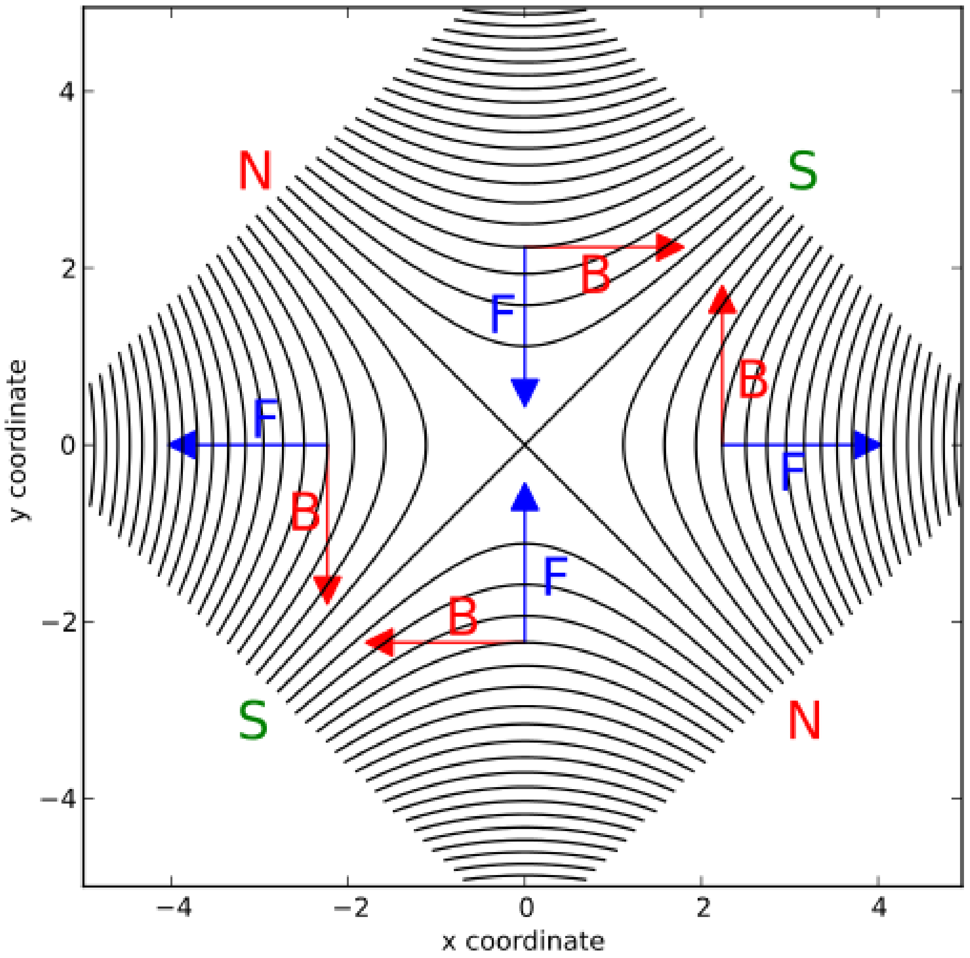

Figure 1.2: Field lines of a quadrupole magnet showing the focusing and defocusing forces. Source: Andre Holzner, Wikipedia

In contrast to optical lenses, quadrupole magnets act as a focusing lense for one plane while defocusing the other one, as can be seen by the force vectors in Fig. 1.2.

1.2.1 Equations of motion

A Taylor expansion of the magnetic field up to the linear term (examplary for one plane) yields:

$$B_y(x) = B_{y0} + \frac{dB_y}{dx}x$$

And with normalization to the particle momentum (see eq. 1.2):

$$\begin{aligned}\frac{B(x)}{p/q} &= \frac{B_0}{B_0\rho} + \frac{g}{p/q}x \\ \frac{B(x)}{p/q} &= \frac{1}{\rho} + kx\end{aligned}$$

with the normalized quadrupole strength $k = \frac{g}{p/q}$.

Looking at a particle with a general trajectory $\rho \to \rho + x$ one obtains the following equation of motion (see the force equilibrium in eq. 1.1):

$$F = m\underbrace{\frac{d^2}{dt^2}(\rho + x)}_{1} = \underbrace{qB_y v}_{2} + \underbrace{\frac{mv^2}{\rho + x}}_{3} \qquad | : m$$

$$\begin{aligned}&1 : \text{as } \rho = \text{const.} \;\; \Rightarrow \frac{d^2}{dt^2}(\rho + x) = \frac{d^2x}{dt^2} \\ &2 : qB_y v = qv(B_0 + gx) \\ &3 : \text{develop for small x as } x \ll \rho \Rightarrow \frac{1}{\rho + x} = \frac{1}{\rho}\left(1 - \frac{x}{\rho}\right)\end{aligned}$$

$$\frac{d^2x}{dt^2} - \frac{v^2}{\rho}\left(1 - \frac{x}{\rho}\right) = \frac{qvB_0}{m} + \frac{qvxg}{m} \qquad | : v^2$$

Change the independent variable from t to the coordinate along the circumference s:

$$\frac{d^2x}{dt^2} = \frac{d^2x}{ds^2}\frac{d^2s}{dt^2} = x''v^2$$

$$x'' - \frac{1}{\rho}\left(1 - \frac{x}{\rho}\right) = \frac{qB_0}{mv} + \frac{qxg}{mv} \qquad | \; mv = p, \frac{B_0}{p/q} = -\frac{1}{\rho}, \frac{g}{p/q} = k \tag{1.3}$$

$$x'' - \frac{1}{\rho} + \frac{x}{\rho^2} = \frac{1}{\rho} + kx$$

Thus one obtains the equation of motion in the horizontal plane:

$$x'' + \left(\frac{1}{\rho^2} - k\right)x = 0 \tag{1.4}$$

And for the vertical plane with $\frac{1}{\rho^2} = 0$ due to no dipoles being present in general and the quadrupole fields changing sign $k \to -k$:

$$y'' + ky = 0 \tag{1.5}$$

1.2.2 Matrix solutions for the equations of motion

The equations of motion eq. 1.4 and eq. 1.5 can be transformed into differential equations of an harmonic oscillator with a spring constant K, with the definitions:

$$\begin{aligned}K_{(hor)} &= \frac{1}{\rho^2} - k\\ K_{(ver)} &= k\end{aligned}$$

For a horizontally focusing quadrupole with $K > 0$ the solutions are:

$$\begin{aligned}x(s) &= x_0 \cos\left(\sqrt{|K|}s\right) + x_0' \frac{1}{\sqrt{|K|}} \sin\left(\sqrt{|K|}s\right)\\ x'(s) &= -x_0\sqrt{|K|}\sin\left(\sqrt{|K|}s\right) + x_0' \cos\left(\sqrt{|K|}s\right)\end{aligned}$$

or in matrix notation:

$$\begin{pmatrix} x \\ x' \end{pmatrix}_{s=l} = \underbrace{\begin{pmatrix} \cos\left(\sqrt{|K|}l\right) & \frac{1}{\sqrt{|K|}}\sin\left(\sqrt{|K|}l\right) \\ -\sqrt{|K|}\sin\left(\sqrt{|K|}l\right) & \cos\left(\sqrt{|K|}l\right) \end{pmatrix}}_{M_{foc}} \begin{pmatrix} x \\ x' \end{pmatrix}_{s=0} \tag{1.6}$$

Similarly for a defocusing quadrupole with $K < 0$ one obtains:

$$\begin{pmatrix} x \\ x' \end{pmatrix}_{s=l} = \underbrace{\begin{pmatrix} \cosh\left(\sqrt{|K|}l\right) & \frac{1}{\sqrt{|K|}}\sinh\left(\sqrt{|K|}l\right) \\ \sqrt{|K|}\sinh\left(\sqrt{|K|}l\right) & \cosh\left(\sqrt{|K|}l\right) \end{pmatrix}}_{M_{defoc}} \begin{pmatrix} x \\ x' \end{pmatrix}_{s=0} \tag{1.7}$$

The transfer matrix for a field-free drift space ($K = 0$) is:

$$M_{drift} = \begin{pmatrix} 1 & l \\ 0 & 1 \end{pmatrix} \tag{1.8}$$

1.2.2.1 Thin lens approximation

Often the focal length of the quadrupole is much bigger than the length of the magnet itself:

$$f = \frac{1}{kl} \gg l$$

Therefore if one does the $\lim\limits_{l\to 0}$ while $kl = \text{const.}$ one obtains the thin lens approximation matrices:

$$M = \begin{pmatrix} 1 & 0 \\ \pm\frac{1}{f} & 1 \end{pmatrix} \tag{1.9}$$

1.2.3 Hill's equation

In a synchrotron the lattice of the magnets defines periodic focusing properties as a function of s. Therefore the equation of motion is a Hill-type differential equation:

$$x''(s) - k(s)x(s) = 0 \quad \text{with} \quad k(s+L) = k(s)$$

with the circumference of the synchrotron L. The general solution of Hill's equation is:

$$
\begin{aligned}
x(s) &= \sqrt{\epsilon}\sqrt{\beta(s)}\cos(\Psi(s)+\Phi) \\
x'(s) &= -\frac{\sqrt{\epsilon}}{\sqrt{\beta(s)}}\left(\alpha(s)\cos(\Psi(s)+\Phi)+\sin(\Psi(s)+\Phi)\right)
\end{aligned}
\tag{1.10}
$$

where ϵ (emittance, see also sec. 1.4) and Φ (initial phase) are integration constants determined by initial conditions, $\beta(s)$ a periodic function given by the focusing properties of the lattice (i.e. quadrupoles), $\alpha(s) = -\frac{1}{2}\beta'(s)$ and $\Psi(s) = \int_0^s \frac{ds}{\beta(s)}$ the so called *phase advance* of the oscillation between two points in the lattice.

Another important property of a synchrotron is the so called *Tune* which is equal to the number of oscillations per turn of a particle (i.e. the total phase advance during one turn around the ring normalized to 360 degrees):

$$Q = \frac{1}{2\pi}\oint \frac{ds}{\beta(s)}$$

The periodic oscillations of the particles around the equilibrium orbit are also called *betatron motion* and their amplitude in phase space (see Sec. 1.4.2 for a description of the phase space) is then called *betatron amplitude*, which is directly related to the emittance ϵ.

1.2.4 The Beta function

From the solution of Hill's equation, eq. 1.10, one can immediately see that the maximum amplitude of a particle is:

$$x_{max}(s) = \sqrt{\epsilon}\sqrt{\beta(s)}$$

Therefore the β-function is an important property of an accelerator, determining the beam size and reflecting the periodicity of the magnet structure.

1.2.5 The Dispersion function

If we go back to Eq. 1.3 on page 5:

$$x'' - \frac{1}{\rho}\left(1 - \frac{x}{\rho}\right) = \frac{qB_0}{mv} + \frac{qxg}{mv}$$

and we assume that the particles have a small momentum error

$$mv = p = p_0 + \Delta p$$

Developing for small momentum errors Δp yields:

$$\frac{1}{p_0 + \Delta p} \approx \frac{1}{p_0} - \frac{\Delta p}{p_0^2}$$

And we obtain:

$$x'' - \frac{1}{\rho} + \frac{x}{\rho^2} = \underbrace{\frac{qB_0}{p_0}}_{-\frac{1}{\rho}} - \frac{\Delta p}{p_0}\underbrace{\frac{qB_0}{p_0}}_{-\frac{1}{\rho}} + \underbrace{\frac{qxg}{p_0}}_{kx} - x\underbrace{qg\frac{\Delta p}{p_0^2}}_{\approx 0}$$

Rearranging leads to the new equation of motion:

$$x'' + \left(\frac{1}{\rho^2} - k\right)x = \frac{\Delta p}{p_0}\frac{1}{\rho} \tag{1.11}$$

Comparing Eq. 1.11 to the equation of motion without momentum error in Eq. 1.4 one can immediately see, that the momentum spread of the beam adds a term on the right hand side of the equation of motion transforming it into an inhomogeneous differential equation.

The general solution looks like:

$$x(s) = x_h(s) + x_i(s)$$

with

$$\begin{aligned} x_h''(s) + K(s)x_h(s) &= 0 \\ x_i''(s) + K(s)x_i(s) &= \frac{\Delta p}{p_0}\frac{1}{\rho} \end{aligned}$$

The so called dispersion function is the normalization of the inhomogeneous part of the solution with respect to the momentum spread:

$$D(s) = \frac{x_i(s)}{\frac{\Delta p}{p}} \tag{1.12}$$

The orbit of any particle is the sum of the homogeneous solution of the equation of motion and the dispersion. Since the dispersion is just another orbit, it is as well subject to the focusing and defocusing properties of the magnetic lattice.

1.3 Third order resonant extraction

The currently used extraction scheme at MedAustron will be explained here, because it has significant influence on the horizontal emittance of the extracted beam (see Sec. 1.4.6). This section is based on the description in the PIMMS study by Bryant et al. [6].

1.3.1 General Resonance Condition

Hill's equation is quasi-harmonic and therefore the danger of exciting resonances exists. In particle accelerators multiple possible resonance exciting sources exists, for example: magnet imperfections, time varying fields, non-linear magnets, collective effects, etc.

The general resonance condition for the tunes in both planes can be written as:

$$kQ_x + lQ_y = m \tag{1.13}$$

where k, l and m are integers. The order of resonances can be categorized by the value of k or l. For $k = 3$ the driving field is a sextupole field and the resonance is called *third order resonance.*

1.3.2 Extraction at MedAustron

At MedAustron the beam extraction from the synchrotron is performed via a so called *betatron core driven third order resonance extraction.* In this extraction scheme a betatron core sextupole magnet slowly pushes the particles into the horizontal resonant tune of $Q_x = 1.666$. This divides the phase space into a stable and an unstable region (see Fig. 1.3a)

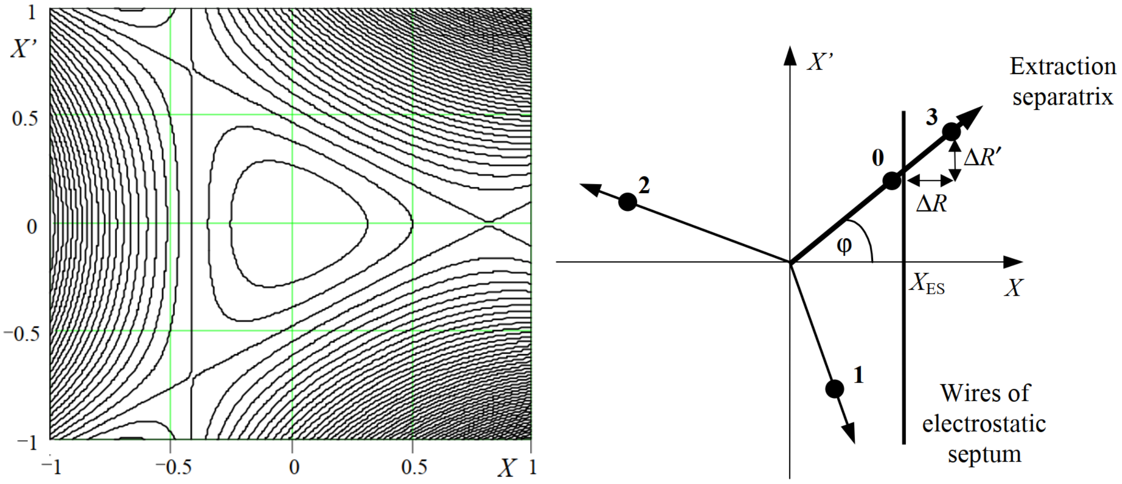

(a) Normalized phase space under resonant conditions. Source: Bryant et al. [6] page 14.

(b) Phase space coordinates for a particle during the last three turns before extraction, starting just inwards of the electrostatic extraction septum (vertical line). Source: Bryant et al. [6] page 31.

As soon as the particles reach the border of the stable region they start to move along the outward facing lines. As soon as they reach the electrostatic extraction septum they are separated from the particles in the ring and get extracted (see Fig. 1.3b). The emittance of the beam plays an important role in the setup of the extraction, since it defines the betatron amplitude of the particles and therefore the crossing of the resonance.

1.4 Emittance of a particle beam

The following sections shall give an overview over the concept of the emittance of a particle beam. An in-depth derivation of the topics presented here can be found in Wiedemann [1], Buon [7], Bryant and Johnsen [3] and Lee [2] on which this section is based.

1.4.1 The canonical phase space

Just like many other physical systems, a beam of particles can be described by its Hamilton function $\mathcal{H}(p_i, q_i, t)$, with the time t, coordinates q_i and the conjugate momenta p_i, where $i = (1, \ldots, f)$ with f degrees of freedom of the system. If the Hamiltonian does not explicitly depend on the time, $\mathcal{H}$ is the invariant total energy of the system.

The canonical phase space is the $2f$-dimensional space with the conjugate coordinates q_i and p_i. The state of the system at a time t is represented by a point $M(t)$ with the respective canonical coordinates in the canonical phase space. As the time increases the representative points $M(t)$ generate a curve, called phase trajectory. When the Hamiltonian is time-independent, there is only one single phase trajectory originating from any point in the phase space and trajectories originating from different points can not cross each other.

Periodic motions (like they happen in a synchrotron) create closed trajectories. For a two-dimensional phase space the existing closed trajectories, combined with the forbidden crossing of trajectories, result in the circumstance, that all trajectories originating from points in a region encompassed by a closed trajectory, are bounded by that trajectory.

1.4.2 Phase space of a particle beam

A beam of N particles is a physical system with $3N$ degrees of freedom[2] and the corresponding canonical phase space therefore is $6N$-dimensional. In the case of identical particles and under the assumption, that they do not interact with each other, the whole problem can be reduced to the 6-dimensional canonical phase space of one particle. Therefore the beam can be represented as N 6-dimensional points instead of one $6N$-dimensional one.

If the longitudinal motion of the beam is decoupled from the motion in the transversal plane (which is usually the case) the phase space can be split into a 2-dimensional longitudinal and a 4-dimensional transverse phase space. If furthermore the transverse motion can be split into two independent motions along two orthogonal directions (usually the horizontal and vertical plane are chosen) the transverse phase space can be split again into two 2-dimensional phase spaces.

1.4.2.1 Trace space

When the transverse momenta p_x and p_y are small compared to the longitudinal momentum p_z the paraxial approximation can be applied relating the transverse angles with respect to the reference orbit x', y' to the transverse momenta according to [7] (for the horizontal momentum):

$$p_x = mv_x + qA_x = m_o c\beta\gamma x' + qA_x$$

with the rest mass m_0 and the charge q of the particle, $x' = \frac{dx}{dz}$ and A_x the horizontal component of the magnetic vector potential. For entirely transversal magnetic fields

---

[2] If internal degrees of freedom, like the spin, can be neglected.

the transversal magnetic vector potential vanishes and the momentum can be written as:

$$p_x = m_o c \beta \gamma x' \tag{1.14}$$

allowing the transformation from the (x, p_x, y, p_y) phase space to the so called (x, x', y, y') trace space. The coordinates and angles are usually given relative to the reference orbit.

1.4.3 Liouville's theorem

Liouville's theorem [1, 7] states, that volumes in the canonical phase space are invariant along the trajectories of a system. From this follows directly[3] that also the phase density in the 6-dimensional phase space is constant.

However, the hypersurface limiting the invariant volume is in general not an invariant and can change its shape along the trajectory. Additionaly, volumes (areas) in a sub phase space are only invariant if their degrees of freedom are uncoupled from the other ones.

1.4.4 Beam emittance

The emittance ϵ of a particle beam is generally defined as the 6-dimensional hypervolume in phase space which is occupied by the beam particles. If the three directions of motion are decoupled (see sec. 1.4.2) the emittance can be defined for each sub-space (e.g. ϵ_x) as the area which is covered by the beam, when projecting the phase space onto the respective phase plane.

Emittance volumes/areas containing all particles are of little practical use, since their values can be dominated by a few particles with extreme angles or positions and therefore become fairly large. Therefore it has become customary to either define the emittance based on the standard deviation, the so called RMS-emittance ϵ_{rms}, or on an ellipse containing an arbitrarily chosen percentage of all particles[4]. Assuming a Gaussian distribution of the beam in both x and x', the RMS-emittance contains 40 % of all particles [2].

The ellipse representing the phase space trajectory of the RMS particle[5] in horizontal (vertical) trace space can be described by the equation [1]:

$$\gamma x^2 + 2\alpha x x' + \beta x'^2 = \epsilon_x \tag{1.15}$$

with the so called *Twiss parameters* $\alpha(s)$, $\beta(s)$ and $\gamma(s)$, with the coordinate along the beam trajectory s. Those are the same ϵ, α and β as already encountered in the solution to Hill's equation in eq. 1.10. From the geometric properties of an ellipse it can be derived that they follow $\gamma = \frac{1+\alpha^2}{\beta}$.

The emittance ϵ_x defined in eq. 1.15 is the aforementioned *RMS* emittance $[\pi\,\mathrm{m\,rad}]$.

---

[3] When neglecting possible particle losses.

[4] This value is usually chosen to be 90 % or 95 %.

[5] Or the particle representing the border of whatever fraction is chosen to limit the emittance.

The area of the ellipse $A = \pi\epsilon$ [m rad] is sometimes also referred to as the emittance. In this thesis the emittance definition resulting in a unit of π m rad will be used.

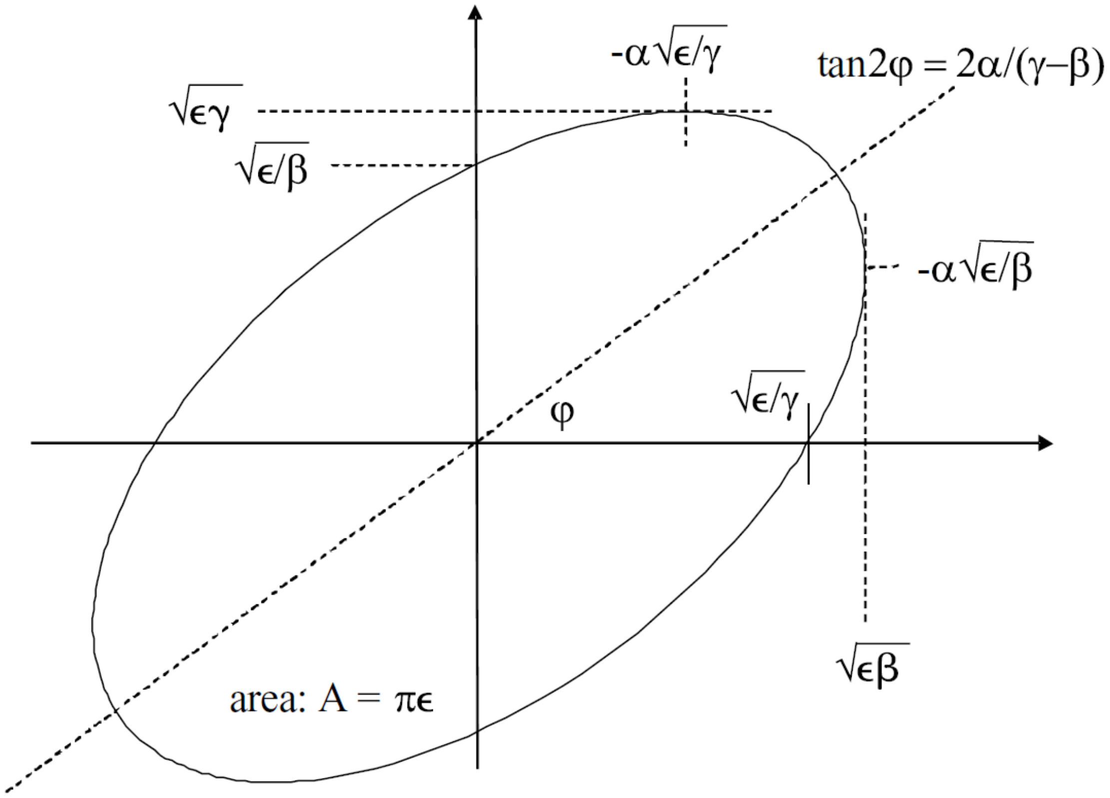

Figure 1.4: Phase space ellipse in the x-x'-plane. Source: Wiedemann [1]

In Fig. 1.4 the dependence of the ellipse shape on the Twiss parameters can be seen: α defines the orientation of the ellipse and therefore whether the beam is divergent or convergent, β [m] is a measure for the beam size and γ for the beams angle spread.

1.4.4.1 Normalized emittance

From eq. 1.14 it can be seen, that the trace space emittance is only invariant as long as the relativistic properties β and γ do not change. For example during acceleration however, the beam angle spread is reduced and therefore the transverse emittance gets smaller. This effect is called *adiabatic damping* and can easily be understood, when considering that during acceleration the longitudinal momentum p_z is increased, while the transverse momenta stay the same. And since $x' \propto \frac{p_x}{p_z}$ the transverse emittance decreases.

To compensate this, one can introduce the so called *normalized emittance*[6]

$$\epsilon_{x,norm} = \beta\gamma\epsilon_x$$

which is an invariant if particle acceleration is the only non-linear effect. The emittance ϵ_x is also referred to as the *geometric emittance*.

---

[6] Here β and γ refer to the relativistic properties and not to the Twiss parameters.

1.4.5 The σ-matrix [2]

The σ-matrix of a beam distribution is defined as

$$\sigma = \begin{pmatrix} \sigma_{11} & \sigma_{12} \\ \sigma_{12} & \sigma_{22} \end{pmatrix} = \begin{pmatrix} \sigma_x^2 & \sigma_{xx'} \\ \sigma_{xx'} & \sigma_{x'}^2 \end{pmatrix}$$

where σ_x and $\sigma_{x'}$ are the rms beam widths and $\sigma_{xx'}$ is the correlation. The σ-matrix transforms from a point s_1 to a point s_2 according to:

$$\sigma(s_2) = \mathbf{R}(s_2|s_1)\sigma(s_1)\mathbf{R}(s_2|s_1)^\top \tag{1.16}$$

where $\mathbf{R}(s_2|s_1)$ is the transfer matrix between points s_1 and s_2 (see sec. 1.2.2 for the transfer matrices). For a normalized particle distribution function $\rho(x, x')$ the rms beam widths can be calculated as:

$$\begin{aligned} \sigma_x^2 &= \int (x - \langle x \rangle)^2 \rho(x, x') dx dx' \\ \sigma_{x'}^2 &= \int (x' - \langle x' \rangle)^2 \rho(x, x') dx dx' \\ \sigma_{xx'} &= \int (x - \langle x \rangle)(x' - \langle x' \rangle) \rho(x, x') dx dx' \end{aligned}$$

with the first moments of the beam distribution:

$$\begin{aligned} \langle x \rangle &= \int x \rho(x, x') dx dx' \\ \langle x' \rangle &= \int x' \rho(x, x') dx dx' \end{aligned}$$

The rms emittance can then be expressed as the determinant of the σ-matrix:

$$\epsilon_{rms} = \sqrt{\det \sigma} = \sqrt{\sigma_x^2 \sigma_{x'}^2 - \sigma_{xx'}^2} \tag{1.17}$$

1.4.5.1 σ-matrix and Twiss parameters [1]

The relationships between the Twiss-parameters and the σ-matrix are:

$$\epsilon\beta = \sigma_{11} \tag{1.18}$$

$$\epsilon\alpha = -\sigma_{12} \tag{1.19}$$

$$\epsilon\gamma = \sigma_{22} = \frac{\epsilon^2 + \sigma_{12}^2}{\sigma_{11}} \tag{1.20}$$

Let $\mathbf{R}$ be the transfer matrix between points s_1 and s_2, then the Twiss-parameters transform according to:

$$\begin{pmatrix} \beta(s_2) \\ \alpha(s_2) \\ \gamma(s_2) \end{pmatrix} = \begin{pmatrix} R_{11}^2 & -2R_{11}R_{12} & R_{12}^2 \\ -R_{11}R_{21} & R_{11}R_{22} + R_{21}R_{12} & -R_{12}R_{22} \\ R_{21}^2 & -2R_{21}R_{22} & R_{22}^2 \end{pmatrix} \begin{pmatrix} \beta(s_1) \\ \alpha(s_1) \\ \gamma(s_1) \end{pmatrix} \tag{1.21}$$

1.4.6 Emittance in the extraction line

This section is based on the description in the PIMMS study by Bryant et al. [6].

The emittance of the beam after the extraction (see Sec. 1.3.2 for a description of the extraction mechanism) differs substantially from the one in the ring. The beam is not only asymmetric in terms of emittance but also asymmetric in its shape in phase space. The vertical emittance in the synchrotron is more or less untouched by the extraction mechanism and will translate directly into the extraction line. While in the vertical plane the beam still occupies the usual elliptical area, in the horizontal plane it looks like a narrow bar, the so called *bar of charge* (see Fig. 1.5). The orientation of this bar is critical since its projection onto the positional coordinate axis determines the spot size for the horizontal plane (see. Fig. 1.6). Therefore the bar of charge must arrive at the patient with a known and controllable orientation.

The set-up of the extraction process therefore defines the horizontal emittance in the extraction line. In return, the horizontal emittance in the ring has a significant influence on the set-up of the extraction, since the emittance defines the betatron amplitudes of the particles and the third order resonant extraction relies on an increase of the amplitudes to cross the resonance lines dividing the stable from the unstable part of the phase space.

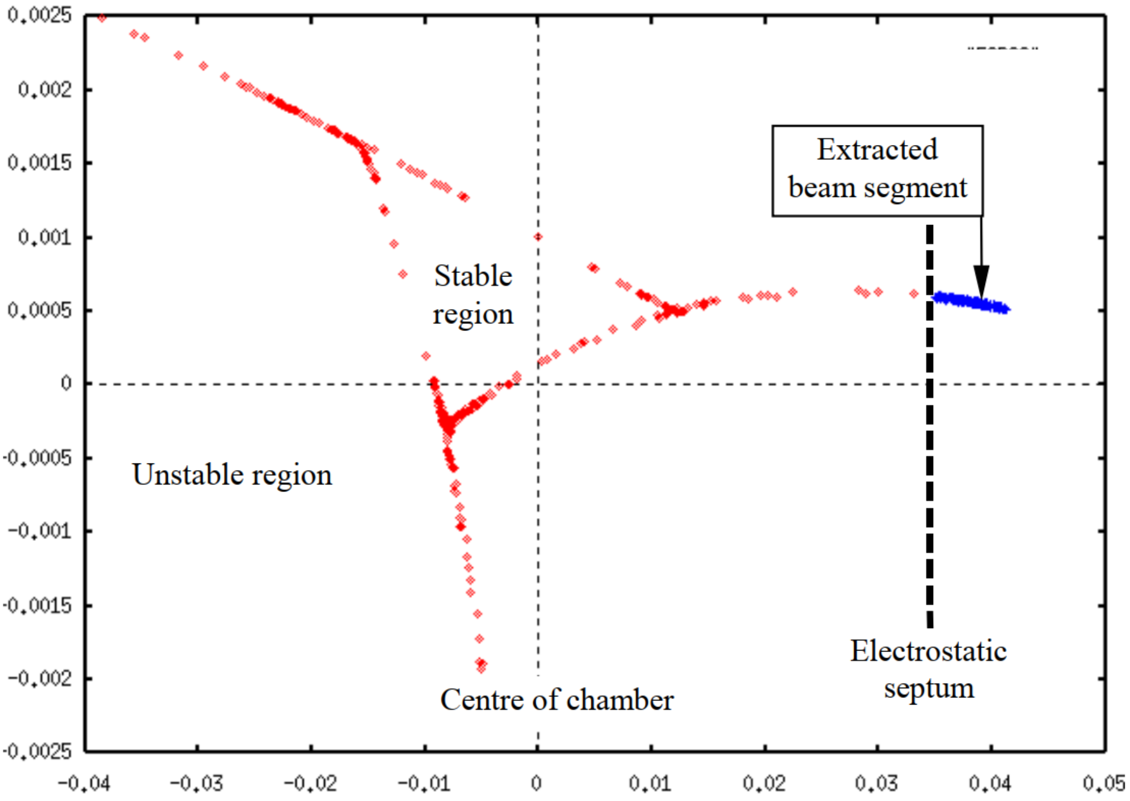

Figure 1.5: Shown are phase space coordinates of particles during the extraction. What can be seen is, that the extracted beam covers only a very narrow bar-shaped area in the phase space. Source: Bryant et al. [6] page 164.

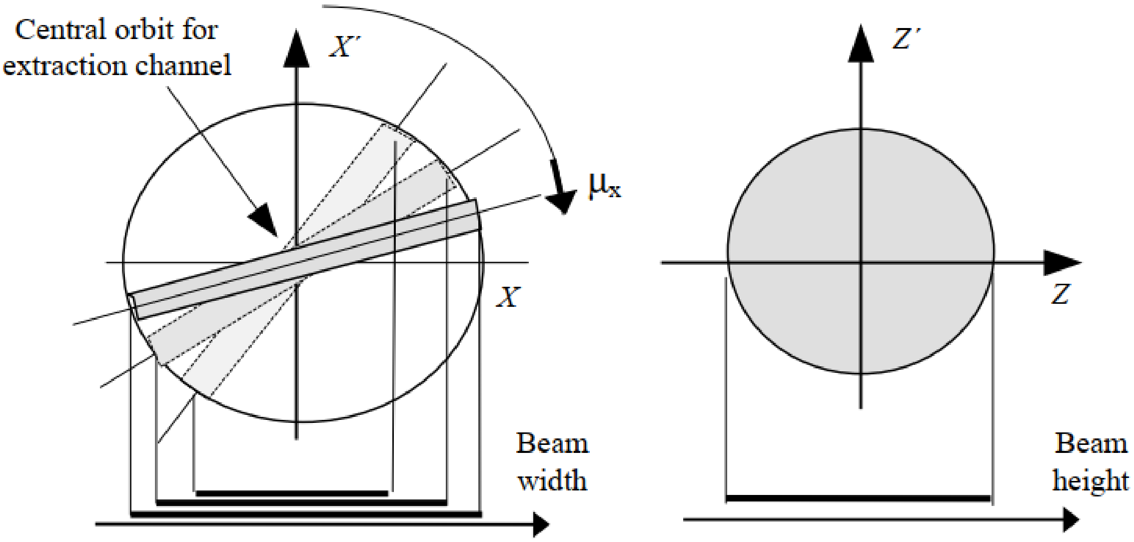

Figure 1.6: Left: bar of charge and impact of the orientation on the beam width. Right: constant beam width for an elliptically shaped beam. Source: Bryant et al. [6] page 169.

2 The MedAustron accelerator and design beam properties

In this chapter a basic overview over the MedAustron accelerator complex and relevant naming conventions and encoding schemes shall be given. Subsequently the clinical requirements on the beam and the design beam properties will be presented.

2.1 The MedAustron facility

MedAustron is a synchrotron based ion therapy and research center located in Wr. Neustadt, Austria. Its design is based on PIMMS[1][6] and CNAO[2][8]. When the commissioning is completely finished it will provide proton and carbon ion beams in the energy ranges of 60 MeV to 250 MeV and 120 MeV/n to 400 MeV/n respectively for clinical treatment and non-clinical research, as well as proton beams up to 800 MeV for non-clinical research.

The facility features four irradiation rooms, three of which are dedicated to clinical operation and a fourth one to non-clinical research (IR1). The three clinical rooms contain two fixed horizontal (IR2&IR3) and a fixed vertical beam line (IR2) as well as a proton gantry (IR4). Commissioning of all fixed lines has been completed for protons, while the commissioning for carbon ions and a proton gantry is ongoing.

The MedAustron accelerator complex features three ECR ion sources, a 400 keV/n RFQ[3] and a 7 MeV/n IH drift tube LINAC feeding the beam into a synchrotron with 77 m circumference.

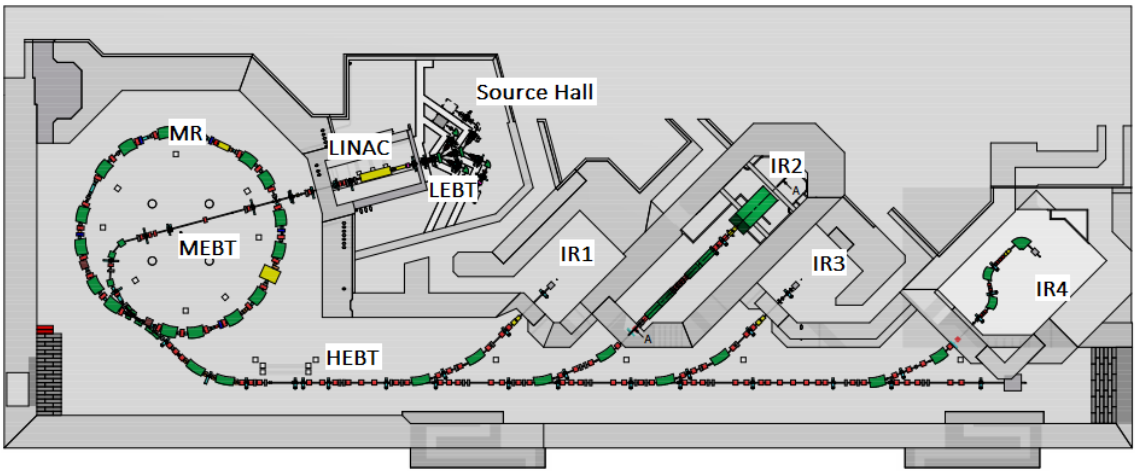

Figure 2.1: Layout of the MedAustron accelerator complex. Source: MedAustron and own annotations.

---

[1] Proton Ion Medical Machine Study

[2] Centro Nazionale di Adroterapia Oncologica

[3] A radio-frequency quadrupole (RFQ) is a linear accelerator component usually used at low beam energies that both accelerates and focuses the beam of charged particles.

2.1.1 Naming convention for accelerator components

All the accelerator components follow a certain naming convention outlined in Fig. 2.2.

Figure 2.2: Example of the applied naming convention on a scintillating fiber hodoscope beam profile monitor in the transfer line to IR3.

The first two characters describe the beam line in which the component is situated. The beam line names are: Sx (for the source branches with x being the number of the source), LE (LEBT), LI (LINAC), ME (MEBT), MR (Main Ring), EX (extraction line), T1 (IR1), T2 (common branch of IR2), H2 (IR2 horizontal beam line), V2 (IR2 vertical beam line), T3 (IR3) and T4 (IR4). Next are two integers specifying the section of the beam line followed by three integers which comprise a running number for all components in the section and lastly three characters specifying which class of component it is.

2.1.2 Cycle Codes

When beam of a certain property is requested to a beam target (in most cases an irradiation room) the request of the beam properties is handed to the accelerator control system via a so called *cycle code*. This is a 16 digit hexadecimal string encoding all necessary information about the: beam line, degrader setting, energy, extraction method, gantry angle, beam size, operational mode, particle type, used source, spill length, variant and version.

2.2 Clinical requirements

From a clinical perspective there are certain requirements on the particle beam, which partly differ between protons and carbon ions. In Table 2.1 the clinical requirements on the energy, number of particles and spot size are presented[4]. The spot size is closely related to the emittance of the beam, while the intensity in the irradiation room depends on the transmission through the individual sections of the accelerator, which in turn is related to the emittance. The requirements have all been taken from [9] (state as of 28th March, 2018).

---

[4] The dose requirement is formulated such, that it should be possible to deliver 2 Gy in less than 120 s to a 2 l tumor volume.

Requirement	$\mathbf{p^+}$	$\mathbf{C^{6+}}$
Range in water [mm]	30-370	36-270
Energy range corresponding to range in water [MeV]	60-250	120-400
Dose requirement	2 Gy/120 s	2 Gy/120 s
Number of particles/spill to fulfill dose requirement	$1 \cdot 10^{10}$	$4 \cdot 10^{8}$
Nominal spot size (FWHM) [mm]	6 (-0/+4)	6 (-0/+4)

Table 2.1: Overview over the clinical requirements

2.3 Design beam properties

2.3.1 Sources

The sources installed in the MedAustron Injector are so called *Supernanogan* ECR ion sources, capable of producing both hydrogen and carbon ions. At the moment three identical sources are installed: S1 for the proton beam, S2 for the carbon ion beam and S3 which is currently a standby source with an envisioned future use for the production of other light ion beams.

The ionization is produced by heating electrons via microwave power on a surface defined by the ECR resonance condition

$$\omega_{RF} = \frac{eB}{m_e}$$

where e is the charge of the electron, B the magnetic field, and m_e the electron mass. The ionization is produced via stepwise electron impact resulting in the production of various high charge states [10].

To fulfill the acceptance of the LINAC, ions with a charge to mass ratio of 1/3 are extracted for both the proton and the carbon ion beam. From the wide array of extracted particles and charge states the H_3^+ and the C^{4+} species are selected via a spectrometer dipole magnet.

To obtain the different ion species, S1 is filled with a H_2 gas, while S2 is filled with a mix of CO_2 and He which acts as a support gas.

The design beam properties for the beam exiting the sources are shown in Table 2.2.

Requirement	$\mathbf{p^+}$	$\mathbf{C^{6+}}$
Current from source [μA]	500	200
$\geq 90\,\%$ beam emittance [π mm mrad]	180	180

Table 2.2: Overview over the extracted beam design parameters. Source: Sargsyan [11]

2.3.2 RFQ and LINAC

The acceleration of the 8 keV/n extracted beam to 400 keV/n is performed by a radio frequency quadrupole (RFQ) which is situated inside the LINAC bunker. The relevant design beam properties for the RFQ are summarized in Table 2.3.

Requirement	Value
Transmission	$> 95\,\%$
Reference input emittance	$0.75\,\pi$ mm mrad (total, normalized)
Maximum output emittance	$1.15\,\pi$ mm mrad (99 % beam, normalized)

Table 2.3: Overview over the RFQ beam requirements. Source: Sargsyan [11]

The linear accelerator used at MedAustron is a so called Interdigital H-mode Drift Tube Linac. Accelerators of this type consist of small conducting, and therefore field-free, tubes with drift space in between. The charged particles are accelerated between the tubes and as soon as they enter the field-free region the polarity of the accelerating field changes its sign to allow further acceleration at the exit of the tube [12]. The LINAC accelerates the particles from 400 keV/n to 7 MeV/n and is designed for a charge to mass ratio of 1/3. The design beam properties of the LINAC are shown in Table 2.4.

Requirement	Value
Transmission	$> 80\,\%$
Reference input emittance	$0.115\,\pi$ mm mrad (rms, normalized)

Table 2.4: Overview over the LINAC beam requirements. Source: Sargsyan [11]

After the acceleration through the LINAC the 7 MeV/n beam is focused on a thin carbon stripping foil, where the H_3^+ and C^{4+} are stripped into three H^+ or one C^{6+} respectively. The injection energy of 7 MeV/n has been selected, because at this energy the stripping efficiency for carbon ions is the highest. Overall a beam stripping efficiency over 90 % is to be expected [11].

2.3.3 MEBT

The medium energy beam transfer line (MEBT) starts after the stripping foil and is an approximately 41 m long section which transports the beam to the synchrotron for the injection process. The MEBT houses the so called *degrader*, a pepper-pot like device which is used to reduce the injected number of particles. The degrader allows four settings: 10 %, 20 %, 50 % and 100 % where the value of the setting indicates the remaining percentage of the beam current (a degrader setting of 100 % therefore means no degradation). Only degrader settings 10 % and 20 % are currently used for clinical operation.

The design RMS emittance in the MEBT is $1.7\,\pi$ mm mrad [13].

2.3.4 Synchrotron

The beam is injected into the synchrotron over multiple turns, gradually filling the available phase space. This technique partially decouples the MEBT from the ring, with the advantage that small changes in the MEBT emittance only affect the injected beam current but not the synchrotron emittance and thus the spot size at the patient.

The design values for the synchrotron emittances are shown in Table 2.5. During the design the emittances were chosen according to the following considerations [14]:

- The normalized vertical emittance for protons and carbon ions is chosen such, that the two species have approximately equal geometrical emittances over the full range of available extraction energies, to have as similar as possible extraction conditions.

- The numerical values for the emittances are chosen to achieve the specified beam spot sizes at the irradiation rooms focal point: $\sqrt{5}\sigma = 4$ to 10 mm.

- Transverse linac emittances are typically small and can be diluted in a flexible and controllable way to meet the above requirements.

Protons	60 MeV/n	250 MeV/n
RMS norm. emittance	0.519	0.519
RMS geom. emittance	1.4286	0.6679
Carbon ions	**120 MeV/n**	**400 MeV/n**
RMS norm. emittance	0.7482	0.7482
RMS geom. emittance	1.4286	0.7324

Table 2.5: Design emittances of the MedAustron synchrotron in π mm mrad for the bottom and top medically used extraction energies. Source: Dorda and Bryant [14]

In the high energy beam transfer line (HEBT) the vertical emittance is directly defined by the vertical emittance in the synchrotron, because it maps approximately one to one, whereas the horizontal emittance is the so called bar of charge and is defined by the extraction set-up.

3 Beam diagnostics devices

The MedAustron beam diagnostics system is based on sixteen different monitor types (153 devices in total) which allow the measuring of all relevant beam parameters from the sources to the irradiation rooms. Table 3.1 gives an overview over the different types of monitors, where they are located and in which number [15]:

Beam Monitor	**Beam Line**	**Number**
Wire Scanners	LEBT	28
Slit Plates	LEBT, MEBT	40
Faraday Cups	LEBT, MEBT	11
Cylindrical Faraday Cups	LEBT	1
Current Transformers	LEBT, MEBT, MR	5
Profile Grid Monitors	LEBT, MEBT	7
Position Pick-ups	MEBT, MR	21
Stripping Foils	MEBT	1
Degraders	MEBT	3
Schottky Pick-ups	MR	2
Scintillating Plates	MR	2
Septum Shadow Monitor	MR	1
Silicon Diode	MR	1
Scintillating Fibre Hodoscopes	HEBT	29
Qualification Monitor	HEBT	1

Table 3.1: Overview beam monitors

The following sections shall give an overview over the working principles of the different monitor types. Only those beam diagnostic devices which were relevant during this thesis will be covered. The description for the different monitor types is based on Forck [16], if not cited differently.

3.1 Beam current and number of particles

The beam current and accordingly the number of particles is a very important parameter for the successful operation of a particle accelerator, especially for the use in particle therapy. To effectively treat tumors, the number of extracted particles from the accelerator needs to be within certain limits to ensure patient safety and guarantee a successful treatment.

In the following sections some of the diagnostics devices used to determine the beam current and number of particles at MedAustron will be presented. Although the ionization chambers are mentioned in this section their form of implementation at MedAustron not only allows the measurement of the beam intensity but also of the beam profile and position.

3.1.1 Current transformers for pulsed beams

The particles in an accelerator form a current which is defined by the number of particles N, with charge q per unit of time t:

$$I = \frac{qN}{t}$$

This relation can also be expressed over a length l with a particle velocity of v as:

$$I = \frac{qNv}{l}$$

The magnetic field of this current can be calculated according to the Biot-Savart law

$$d\vec{B} = \mu_0 I \cdot \frac{d\vec{l} \times \vec{r}}{4}$$

where μ_0 is the vacuum permeability, $d\vec{l}$ the length in direction of the beam and $\vec{r}$ the distance between the beam central point and the point at which the field is measured. For the cylindrical symmetry of the beam only the azimuthal component of the field has to be considered:

$$\vec{B} = \mu_0 \frac{I}{2\pi r} \cdot \vec{e}_\phi$$

Via monitoring the field one can therefore determine the beam current. One way to accomplish this is via a current transformer: the beam passes through a torus and serves as the primary winding and a wire wound around the torus serves as the secondary winding (see Fig. 3.1). The reason for choosing a torus geometry for the transformer core, is that this geometry guides the field-lines in a way which enables to only measure the azimuthal component of the $\vec{B}$-field and makes the signal strength nearly independent from the beam position inside the torus.

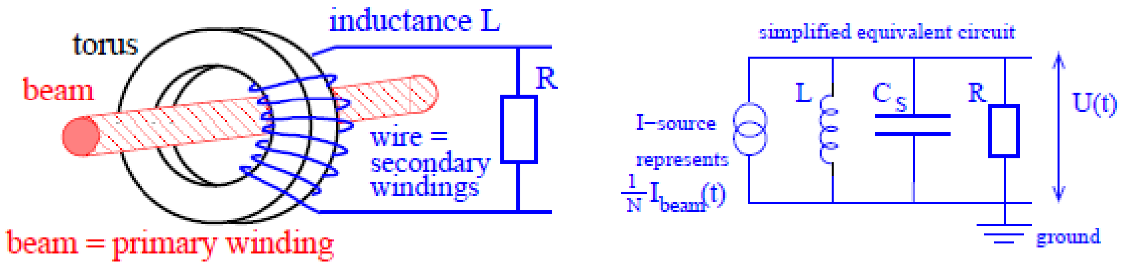

Figure 3.1: Sketch of a torus current transformer (left) and the corresponding simplified equivalent circuit (right). Source: Forck [16], p. 11

A remark which should be made is, that to shield the transformer against external magnetic fields, a metal housing is installed (see Fig. 3.2 left). In combination with an interruption of the electrical conductivity of the beam pipe, for example through an insulator like ceramics or plastic, the flow of image current inside the transformer torus is avoided. This current would have the opposite sign and its field would therefore cancel out the magnetic field created by the beam leading to zero signal in the transformer.

From the current the number of particles can easily be calculated as:

$$N = \frac{It}{q}$$

with the beam current I, the charge per particle q and the time t during which the beam was inside the current transformer.

At MedAustron there are four current transformers for pulsed beams (CTAs) installed. They are located at the end of the LEBT, after the LINAC, in the MEBT and in the main ring.

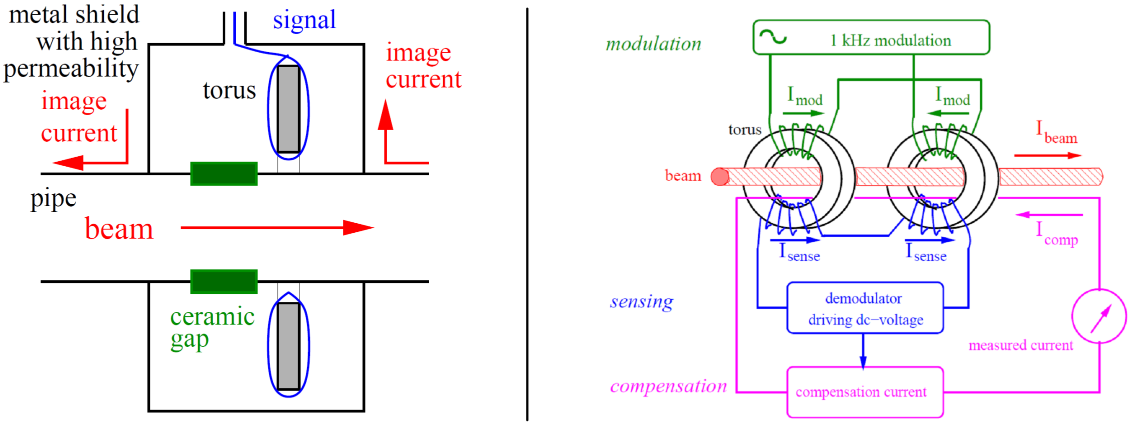

Figure 3.2: Sketch of the transformer shielding (left) and of a torus DC-transformer (right). Source: Forck [16] p. 15 (left) and p. 19 (right)

3.1.2 DC current transformers

The transformer design described in the previous section can, of course, only be used for short times (short bunches) due to the required change in current for induction to occur. If one desires to measure DC-beam current, for example in a synchrotron with longer storage or extraction times in the order of seconds or longer, a DC current transformer needs to be used. The principle of such a transformer is shown in Fig. 3.2 (right). It consists of two tori with opposite modulation windings. The modulation winding is used to drive the torus into magnetic saturation two times per modulation period. The sensing winding acts as a detector for the modulated signal. Due to the opposite modulation winding, the detector signal should be exactly zero if there is no beam current inside the tori (see Fig. 3.3 upper). If a beam (DC) is flowing through the transformer, the hysteresis curve gets asymmetrically shifted due to the additional magnetic field from the beam, which results in the sum signal being different from zero with a modulation twice as high as the applied modulation frequency (see Fig. 3.3 lower). In practice this DC-current is measured via the compensation circuit, which applies a feedback current through the third winding of the tori to keep the detector current I_{sense} at zero.

At MedAustron there is one DC current transformer (CTS) installed in the main ring.

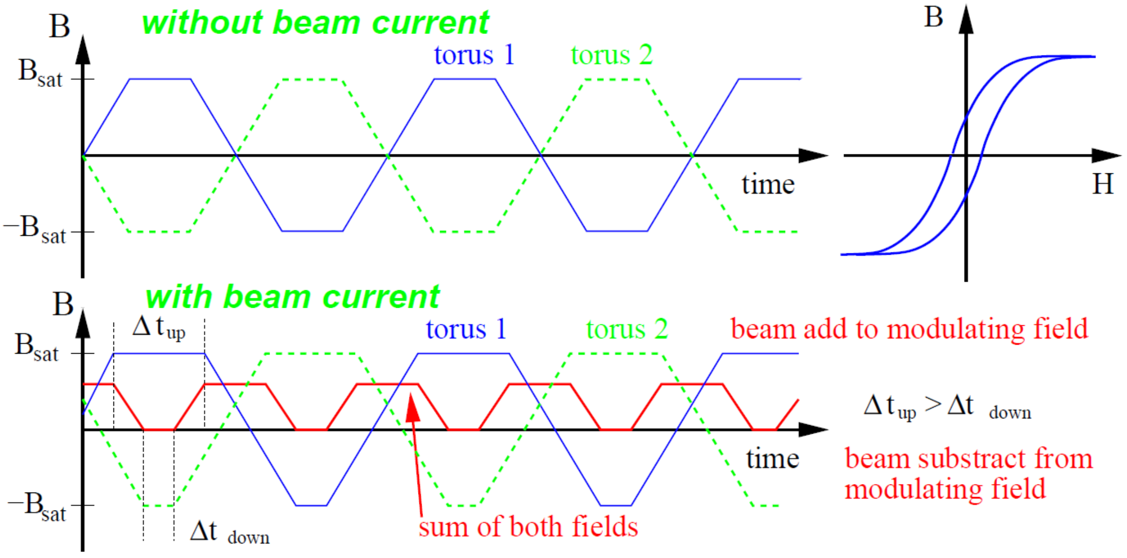

Figure 3.3: Signal of the two tori without beam (upper) and with beam (lower). Source: Forck [16] p. 20

3.1.3 Ionization Chamber

The set up of an ionization chamber resembles that of a capacitor. The beam passes a gas volume confined between two metalized plastic foils which act as the electrodes. Inside the gas, the beam particles produce electron-ion pairs, which are separated via a high voltage applied to the electrodes. At one electrode the amount of secondary charge is measured with a sensitive current amplifier. From this secondary current I_{sec} the beam current I_{beam} and therefore also the number of particles can be calculated according to:

$$I_{sec} = \frac{1}{W} \cdot \frac{dE}{dx} \Delta x \cdot I_{beam}$$

where W is the average energy for the production of an electron-ion pair (which is a well known quantity for many gases) and the calculated energy loss of the beam particles $\frac{dE}{dx}$ over the length of the ionization chamber Δx. Therefore the precision of the measurement is mainly dependent on the accuracy of the energy loss calculation. To reach higher precision a calibration can be done, for example with respect to a scintillator, where absolute measurements can be performed.

At MedAustron each irradiation room is equipped with several ionization chambers which are all part of the so called Dose Delivery System (DDS) which was developed by the Italian National Center of Oncological Hadron-therapy (CNAO). Each of the irradiation rooms DDSs consists of two independent detectors in separate boxes.

The first box contains an integral chamber which has a large area anode to measure the overall beam current and two additional anodes (one for horizontal and one for vertical measurement). They are each divided into 128 strips, 1.55 mm wide and with a gap of 1.65 mm which allow for a position and profile measurement of the beam. The second box contains an integral chamber as well and instead of the strip anodes it contains a chamber with an anode divided into 32 x 32 pixels, for positional and profile measurement. The area of each pixel is 6.5 x 6.5 mm^2 and the pitch is 6.6 mm. [17]

3.2 Beam profile and position

The measurement and control of the beam profile and position is not only important for the production and delivery of the beam but also for the treatment of the patients. In ion therapy it is of utmost importance to have the ability to deliver a beam of a certain dimension to an exact location.

Before diving into the details of the different beam position monitoring devices the distinction between destructive and non-destructive devices should be emphasized. Destructive devices are called that way because they directly interact with the beam and need to be placed into the beam path, or excite the beam to acquire data, whereas non-destructive devices can measure parasitically. Of the monitoring devices mentioned in this section, at MedAustron[1] the wire scanners, scintillating fibre hodoscopes and secondary electron emission grids are all destructive, whereas the pick-ups are non-destructive.

3.2.1 Wire scanners

The functional principle of a wire scanner is simple: a single wire is swept through the beam and the emitted secondary particles are measured. The advantage of this setup, compared to an array of multiple spaced wires, is that the resolution can be much higher, since it is not limited by the wire spacing. But this also comes with a great disadvantage: since only a single wire is used, only a part of the beam can be observed at any instant and not the whole profile.

For low energy proton and ion beams, the beam intensity at a given position can be calculated from the current of the emitted secondary electrons, whereas for beam energies higher than ~150 MeV/n the secondary particles can be measured outside of the vacuum chamber, for example by a scintillator. In this case the secondary particles might be hadrons created by the interaction of the protons or ions with the wire material, which have enough kinetic energy to leave the beam pipe.

A schematic set up of wire scanners can be seen in Fig. 3.4. A rotating wire scanner, as seen in Fig. 3.4 (a), can be used with high wire speeds of up to several m/s with the advantage of short sweeping times (which are necessary for some applications to avoid melting of the wire by the beam) but the disadvantage of worse spatial resolution due to vibrations of the wire. Fig. 3.4 (b) shows the use of two wires in a fork which allows the simultaneous measurement of both transverse beam profiles.

At MedAustron there are 14 wire scanners installed in the Source branches (10) and LEBT (4), each of them containing one wire for horizontal and one for vertical profile measurement.

---

[1] The wire scanners and scintillating fiber hodoscopes find non-destructive uses in other accelerators.

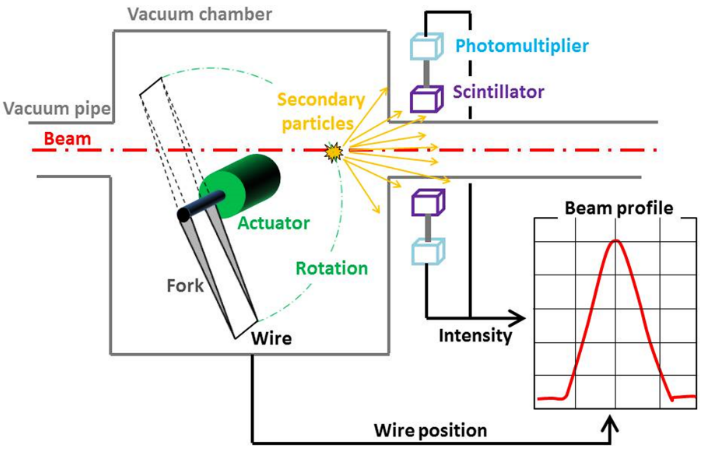

(a) Working principle of a (rotating) wire scanner with secondary particle detection outside of the vacuum chamber. Source: `http://vibrationacoustics.asmedigitalcollection.asme.org/article.aspx?articleid=2522108`

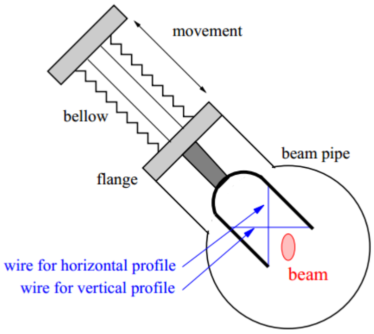

(b) Linear feed-through wire scanner showing the simultaneous use of two wires for measuring the horizontal and the vertical profile within one sweep. Source: Forck [16] p. 48.

Figure 3.4: Wire scanners.

3.2.2 Pick-ups

The position of the beam within the synchrotron can be determined via pick-up plates. The working principle of the pick-up measurement is, that the electric field of the charged beam particles can induce image charges of the same magnitude as the beam charges (but reversed polarity) in an insulated plate.

A capacitive beam position pick-up consists of four isolated plates inserted into the vacuum chamber (two for horizontal and two for vertical beam position determination). The deviation of the beam from the center of the beam pipe can be determined via the induced voltage difference between the two corresponding plates. If the beam is exactly in the middle of the vacuum chamber, the induced voltages in both plates are the same. Should the beam deviate from the center, the induced voltage in the closer pick-up plate will be higher and therefore the position can be determined (see Fig. 3.5 (a) for reference of the corresponding variables) according to:

$$y = \frac{1}{S_y} \cdot \frac{U_{up} - U_{down}}{U_{up} + U_{down}} \tag{3.1}$$

with the so called position sensitivity S_y. This sensitivity can itself be dependent on the beam position, leading to a non-linear voltage response for larger beam displacements. To circumvent this, one can use so called *Shoe box* pick-ups, which consist of a box-like device through which the beam passes. They are particularly well applicable in proton and ion synchrotrons due to the long bunches, which allow long plates and therefore high signal strength.

While the signal in the conventional pick-ups is dependent on the proximity to the plates, in the shoe box pick-ups it is proportional to the path length of the beam through each electrode (see Fig. 3.5 (b) for reference). For a displacement of the beam x the image voltage is proportional to the length l of the beam projected onto the electrodes surface. Therefore:

$$l_{right} = (a + x) \cdot \tan\alpha \quad \text{and} \quad l_{left} = (a - x) \cdot \tan\alpha \Rightarrow x = a \cdot \frac{l_{right} - l_{left}}{l_{right} + l_{left}}$$

due to the dependence of the image voltage on the position the displacement is:

$$x = a \cdot \frac{U_{right} - U_{left}}{U_{right} + U_{left}} \Rightarrow (\text{compare eq. } 3.1) \Rightarrow S_x = \frac{1}{a} \tag{3.2}$$

as one can see in eq. 3.2 the sensitivity is (for this ideal case) constant. This also holds true for the real case, where the shoe box pick-up sensitivity is constant for almost the full range of displacements.

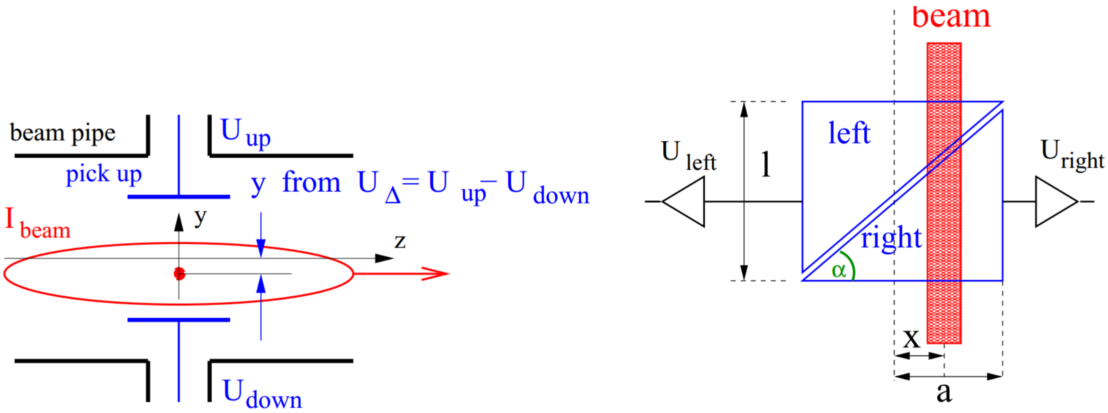

(a) Layout of a plain electrode pick-up.

(b) Layout of a linear cut shoe box pick-up showing the different path lengths of the beam through the electrodes if it deviates from the center.

Figure 3.5: Position pick-ups. Source: Forck [16] p. 84 (a) and p. 88 (b).

At MedAustron there are 21 shoe box pick-ups (12 horizontal and 9 vertical) installed in the main ring.

3.2.3 Scintillating fiber hodoscopes

When a particle hits a scintillating material, the energy loss by the collision with the target electrons can lead to the emission of fluorescence photons. These photons can then be detected by a camera or some other form of detector, amplified by a photo-multiplier and finally counted to get a signal proportional to the number of incident particles.

In the case of scintillating fiber hodoscopes the beam diagnostic device does not consist of one continuous scintillation screen as in the case of classical scintillation detectors, but of an array of scintillating fibers. There are two sets of fibers spanning the whole vacuum chamber: one for the horizontal and one for the vertical direction. The fibers do not emit the fluorescence light but instead they act as optical wave guides, leading the emitted light directly onto the photosensitive part of a CCD camera.

By knowing which fiber connects to which array of pixels on the camera, the overall profile of the beam can be reconstructed allowing for a calculation of the beam position and beam width.

At MedAustron there are 29 scintillating fiber hodoscopes (SFX) installed in the HEBT.

3.2.4 Secondary electron emission (SEM) grid

These beam monitoring devices work quite similar to the wire scanner described in section 3.2.1 on page 25. The most distinct difference is that in the case of a wire scanner one single wire is swept through the beam and the current generated by the secondary particles is measured, whereas a SEM grid consists of an array of stationary wires covering the whole vacuum chamber. Each wire is equipped with its own amplifier.

This setup has the advantage over the wire scanner that it can be used for pulsed beams as well, but with the disadvantage of a worse spatial resolution due to the gaps between the wires.

At MedAustron there are 7 secondary electron emission grids (here called Profile Grid Monitors - PGX) installed in the MEBT and LEBT.

4 Description of relevant beam property measurement concepts

4.1 Beam emittance

Measurement and control of the emittance of a particle beam is of utmost importance for the commissioning and operation of a particle accelerator. Not only does the emittance tell if the beam will fit in the vacuum chamber or not, it is also one of the key parameters to control when matching individual parts of the accelerator together. In the end by defining the beam size, the emittance also defines the spot size of the particle beam in the irradiation room, which is especially important for the treatment of patients.

The following sections shall give an overview over the different measurement procedures to obtain the emittance in the injector (Source branches, LEBT, MEBT) the synchrotron and the transfer lines (mainly HEBT but also MEBT).

4.1.1 Injector

To measure the emittance after the sources, in the LEBT (Low Energy Beam Transfer) and MEBT (Medium Energy Beam Transfer) lines at MedAustron, the slit-grid method is used. It uses a combination of a slit and a wire scanner (see Sec. 3.2.1 on page 25 for information on the wire scanners) in the source branches and the LEBT and a combination of a slit and a secondary electron emission grid (see Sec. 3.2.4 on page 28 for information on the profile grids) in the MEBT. The slit-grid method is especially useful for low energy beams, because it is a direct measurement of the x and x' distribution and can therefore be used to show aberrations in the beam distribution.

The basic principle of this method is to determine the trace space of the particle beam by artificially restricting its spatial extension and measuring the corresponding beam angles. For this, a small gap in the beam pipe is formed by two slit plates, letting only a small portion of the beam pass. A beam profile monitor is positioned a certain distance ds downstream of the slits to measure the change of the particle position dx (this of course also works the same way for the vertical plane) after the particles traveled ds. Using the paraxial approximation the beam angle $x' = \frac{dx}{ds}$ can be determined. Subsequently the slits are moved to slice the beam at the next position and this whole process is repeated until the whole beam has been covered. Fig. 4.1 illustrates the process.

The resolution of this method is limited by the width of the chosen slit gap, the length of the drift space between the slit and the beam profile monitor, and the resolution of the beam profile monitor itself. Especially the noise on the monitor is a limiting factor due to the circumstance, that the use of the slits reduces the beam current measured by the profile monitor to an order of magnitude of 10^{-2} of

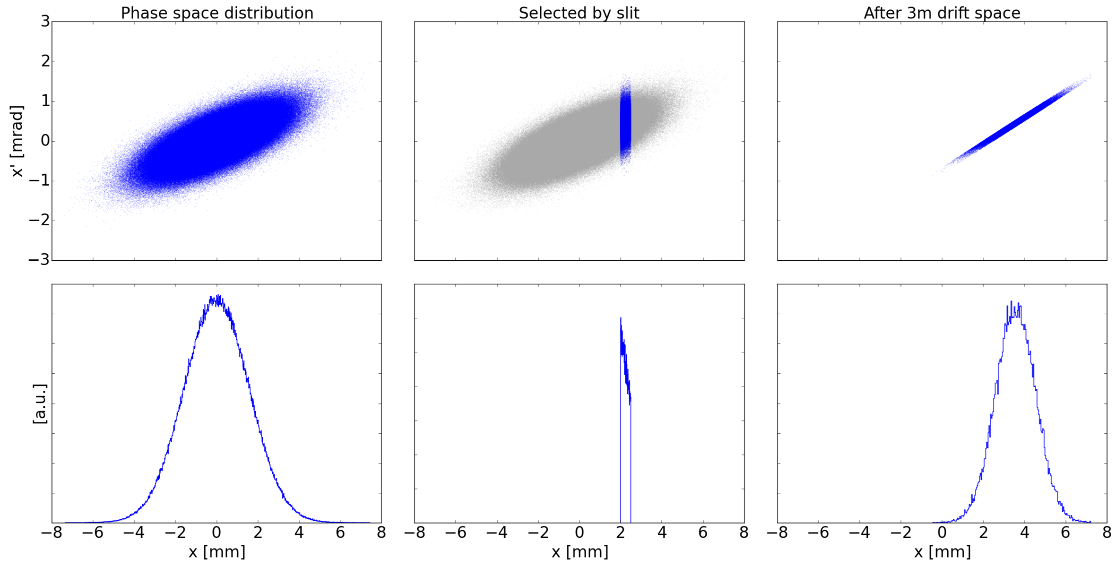

Figure 4.1: Illustration of the process of the slit-grid method. A range in position is selected by a slit from the phase space distribution. The angle spread in this range translates over a drift space into an increase in beam size at a position monitor downstream of the slit.

the overall beam current, which is especially problematic in the regions of the beam halo where it drops to an order of magnitude of 10^{-4}.

4.1.2 Main Ring

In Fig. 1.4 it can be seen, that the maximum positional amplitude of a particle corresponds to $\sqrt{\epsilon\beta}$. Hence if the β-function is known, the emittance can be determined by measuring the beam width in the synchrotron. Emittance ϵ and beam width σ are related according to [18]:

$$\epsilon_x = \frac{1}{\beta_x(s)}\left[\sigma_x^2 - \left(D(s)\frac{\Delta p}{p}\right)^2\right] \quad \text{and} \quad \epsilon_y = \frac{\sigma_y^2}{\beta_y(s)} \tag{4.1}$$

with the dispersion function D (see Sec. 1.2.5) and the particle momentum spread $\frac{\Delta p}{p}$.

To determine the beam width, a so called scraper plate is moved through the beam pipe while the beam current signal is continuously observed. As the scraper moves through the beam path, the particles hit the plate and get lost, thereby reducing the overall beam current. Two vertical and two horizontal copper scraper plates are installed in dispersion free regions of the ring. Both plates of each pair are on opposite sides of the vacuum chamber while being at the same longitudinal position. The scraper plates are moved one by one into the path of the circulating beam while measuring the beam intensity losses with a current transformer (CTS, see Sec. 3.1.2 for a description of the current transformer for a DC beam), as can be seen in Fig. 4.2 top.

The numerical derivative of this decreasing beam current (see Fig. 4.2 bottom) is the

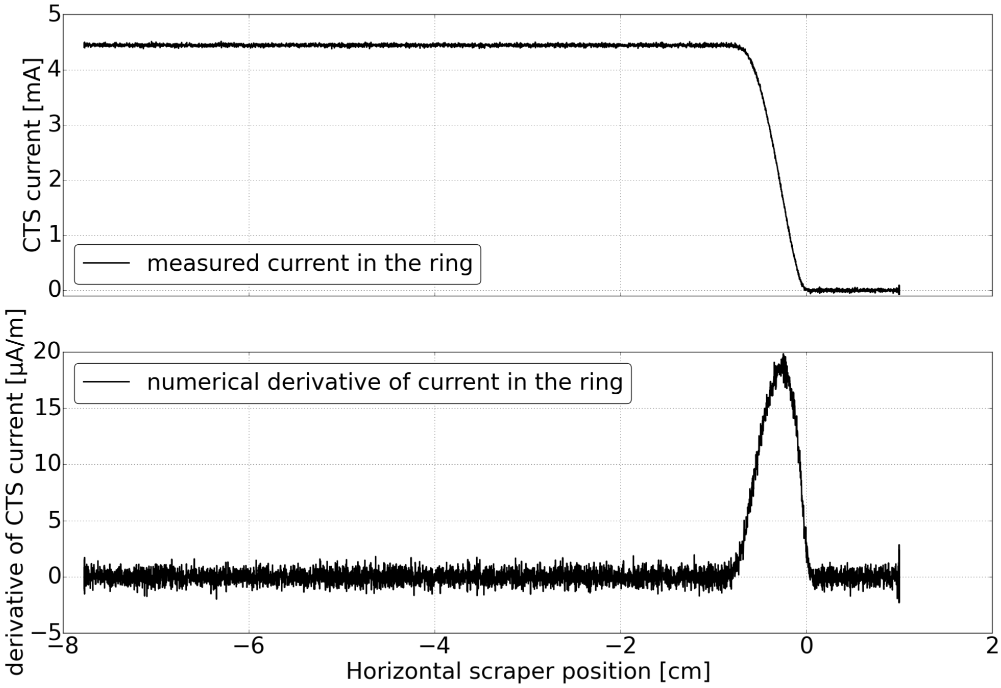

Figure 4.2: Example of a beam current signal (top) and its derivative (bottom) over the position of the scraper. The derivative of the beam current signal represents the betatron amplitude distribution of the particles. The measurement was taken for a 400 MeV carbon ion beam.

distribution of the betatron amplitudes (see Sec. 1.2.3) of the particles. According to [19] the RMS of the betatron amplitude distribution is related to the RMS width of the beam like:

$$\frac{\sigma_{betatron}^2}{\sigma_{beam}^2} = 2 \tag{4.2}$$

Therefore by computing the width of the beatron amplitude distribution and taking into account the fact that the scrapers are in a non-dispersive region of the ring (therefore the second part in the horizontal emittance in eq. 4.1 vanishes) one can immediately obtain the beam emittance in the synchrotron.

4.1.2.1 Intrinsic resolution

Measurements of the transverse beam size by scraping suffer from intrinsic resolution limits related to the speed of the scraping plate, due to the fact that even at irrational fractional tunes the scraping takes a certain number of turns. Due to the movement of the scraper during this time, the particles appear smeared out over a certain fraction of their amplitude. According to Schönauer [20] the scraper advance x_{max} over the maximum number of turns needed for full scraping, relative to the betatron amplitude r can be written as:

$$\frac{x_{max}}{r} = \frac{1}{2}\left(\frac{3\pi d}{r}\right)^{2/3}$$

with the advance d of the scraper plate per beam revolution period. This holds true, if the tune difference δ of the fractional part of the tune from the closest resonance

M/N fulfills the following inequality:

$$\delta > \frac{\left(3\pi\frac{d}{r}\right)^{1/3}}{\pi N}$$

where N is the order of the resonance. This is fulfilled for all used tune set-points, therefore the above formula is valid.

The results of this resolution limit for several key energies and a scraper speed of 0.02 m/s are summarized in table 4.1. For all possible settings the intrinsic resolution limit is below 0.1 % and is therefore negligible in the analysis of the measurements. Only in larger machines with significantly larger revolution periods this could become a limiting factor, making a limitation of the scraper speed necessary, which would result in higher measurement times. In Sec. A.1 in the appendix, an illustration of the derivation of the intrinsic scraping resolution is shown.

energy [MeV/n]	rev. period [μs]	x_{RMS} [mm]		relative resolution [%]	
		horizontal	vertical	horizontal	vertical
400	0.36	2.53	3.18	0.045	0.038
120	0.56	3.53	4.44	0.048	0.041
252	0.42	2.42	3.04	0.051	0.044
62	0.75	3.54	4.44	0.058	0.05
7	2.13	5.75	7.46	0.085	0.071

Table 4.1: Revolution period, design RMS betatron amplitude and relative intrinsic scraping resolution limit for the top and bottom medically used extraction energies for carbon ions (400 and 120 MeV/n) and protons (252 and 62 MeV), and at the injection energy (7 MeV/n). The speed of the scraper used for this calculations was assumed to be 0.02 m/s.

4.1.3 Transfer lines

As already mentioned in Sec. 1.4.6 the shape of the horizontal emittance in the extraction line differs substantially from the one in the synchrotron. This is due to the fact that the extraction mechanism creates a so called bar-of-charge instead of the classical elliptical shape. Due to this fact the physical interpretation of the value which one obtains for the geometric beam emittance is less straight forward, but since the RMS emittance does not explicitly depend on the shape of the particle distribution the same formalism as for approximately Gaussian beam distributions can still be applied.

In the following, two common methods to determine the emittance in transfer lines shall be presented. Of those two, only the quadrupole tuning method has been implemented and used during this thesis, due to the significant advantage of determining besides the emittance and the Twiss parameters also the offset of the beam.

4.1.3.1 Three profiles [2]

To obtain the rms beam emittance in a transfer line (HEBT or MEBT) one has to determine the three unknowns in eq. 1.17.

One way to achieve this is to measure the beam size at three different spots (with three individual monitors, or a single movable monitor). If one inserts into eq. 1.16 the transformation matrix of a drift space (see eq. 1.8) one obtains the following set of equations for the three monitor positions:

$$\begin{aligned} r_1^2 &= \sigma_{11} \\ r_2^2 &= \sigma_{11} + 2L_1\sigma_{12} + L_1^2\sigma_{22} \\ r_3^2 &= \sigma_{11} + 2(L_1+L_2)\sigma_{12} + (L_1+L_2)^2\sigma_{22} \end{aligned}$$

With r_x^2 being the beam radius at the x-th position, and L_1 and L_2 being the drift distances between monitor positions 1 and 2 respectively 2 and 3, as well as σ_{ij} being the elements of the σ-matrix at the first monitor position.

Upon solving this set of equations one can obtain all elements of the σ-matrix at the position of the first monitor and therefore calculate the RMS-emittance at that position.

The difficulty of that approach is to find a set of three monitors which are only separated by drift-space, since additional quadrupoles in between the monitors would make the calculations more difficult and error prone. One reason for that is for example, that the possible misalignment of the quadrupoles would lead to additional dipole kicks which would need to be considered as well in the transfer matrices.

4.1.3.2 Quadrupole tuning [1]

A second way which only relies on a single beam profile monitor is the so called quadrupole tuning method (also referred to as quadrupole scan).

Using the transfer matrix **Q** of a quadrupole under thin lens approximation (see sec. 1.2.2.1) and a transfer matrix **S** of an arbitrary beam line to a beam profile monitor, then the whole transfer matrix **R** from the entrance of the quadrupole (subscript 1) to the monitor (subscript 2) is:

$$\mathbf{R} = \mathbf{SQ} = \begin{pmatrix} S_{11} & S_{12} \\ S_{21} & S_{22} \end{pmatrix} \begin{pmatrix} 1 & 0 \\ -kl & 1 \end{pmatrix} = \begin{pmatrix} S_{11} - klS_{12} & S_{12} \\ S_{21} - klS_{22} & S_{22} \end{pmatrix}$$

The beam size at the monitor location can be expressed in terms of the transfer matrix **R** when using the transformation properties of the Twiss-parameters (eq. 1.21):

$$\sigma_2^2 = \epsilon\beta_2 = \epsilon(R_{11}^2\beta_1 - 2R_{11}R_{12}\alpha_1 + R_{12}^2\gamma_1) \tag{4.3}$$

With the relationships between the Twiss-parameters and the σ-matrix (eqs. 1.18-1.20) this can also be written as:

$$\sigma_2^2 = R_{11}^2\sigma_{11} + 2R_{11}R_{12}\sigma_{12} + R_{12}^2\frac{\epsilon^2 + \sigma_{12}^2}{\sigma_{11}}$$

After substituting the matrix elements of **R** one arrives at:

$$\sigma_2^2 = (S_{11} - klS_{12})^2\sigma_{11} + 2(S_{11} - klS_{12})S_{12}\sigma_{12} + S_{12}^2\frac{\epsilon^2 + \sigma_{12}^2}{\sigma_{11}}$$

This can be rearranged to:

$$\sigma_2^2 = \sigma_{11} S_{12}^2 \left[\left(\frac{S_{11}}{S_{12}} - kl \right) + \frac{\sigma_{12}}{\sigma_{11}} \right]^2 + S_{12}^2 \frac{\epsilon^2}{\sigma_{11}}$$

Which can be written as:

$$\sigma_2^2 = A(B - kl)^2 + C \tag{4.4}$$

with

$$\begin{aligned} A &= \sigma_{11} S_{12}^2 \\ B &= \frac{S_{11}}{S_{12}} + \frac{\sigma_{12}}{\sigma_{11}} \\ C &= S_{12}^2 \frac{\epsilon^2}{\sigma_{11}} \end{aligned}$$

From this it can be seen that the beam emittance can be calculated as:

$$\epsilon = \frac{\sqrt{AC}}{S_{12}^2}$$

The other Twiss parameters can of course be calculated as well:

$$\begin{aligned} \beta &= \sqrt{\frac{A}{C}} \\ \alpha &= -\beta \left(B - \frac{S_{11}}{S_{12}} \right) \end{aligned}$$

To obtain the RMS-emittance one therefore has to do a measurement series of the RMS-beam width σ_2 on the beam profile monitor as a function of varying quadrupole strength k. To this data a function of the form seen in eq. 4.4 can be fitted to obtain A and C. The only thing left is the S_{12} element of the transfer matrix which in the case of a drift space is simply the length of that space.

To obtain good measurement results, the quadrupole scan should be performed in a way that the beam waist can be measured. This means, that the focal point of the quadrupole is moved from one side of the beam profile monitor to the other side during the scan, resulting in a parabolic shape of the squared beam size as a function of the quadrupole strength. Additionally the best results are to be expected for beams which are broad (large β) and divergent (negative α) at the position of the quadrupole.

An additional advantage of this method is, that with the same set of measurements the centering of the beam, compared to the magnetic center of the quadrupole, can be determined as well. The beam property of interest is in this case not the beam size but rather the position of the beam center.

If we assume that the beam is perfectly centered in the quadrupole, a scan of the quadrupole strength (as performed for the emittance measurement) should only affect the beam size. Should however the beam be slightly misaligned in the quadrupole, it will experience a dipole-kick leading to a linear change of the beam position on the beam profile monitor as a function of the quadrupole strength, with a slope directly proportional to the offset. Fitting a linear curve of the form $x = a \cdot kl + b$ to the beam position as a function of the normalized quadrupole strength kl, allows the computation of the beam offset in the quadrupole according to:

$$\Delta x = -\frac{a_x}{S_{12}} \tag{4.5}$$

$$\Delta y = \frac{a_y}{S_{12}} \tag{4.6}$$

The negative sign in eq. 4.5 is to get the offset of the beam in the quadrupole and not the offset of the monitor. The inverted sign in eq. 4.6 is due to the fact that per convention a positive quadrupole strength means focusing in horizontal plane and therefore the quadrupole acts as defocusing in the vertical plane, inverting the sign of the slope of the linear fit.

4.2 Transmission

The transmission of the number of particles through the individual subparts of the accelerator is an important figure of merit during the commissioning and operation, to judge how well set-up the machine is and if any corrections are needed. Since the transmitted intensity defines the dose delivered to the patient, it is also an important factor in determining the treatment duration.

To measure the number of particles, current transformers for pulsed beam (CTA, see Sec. 3.1.1) are installed in the LEBT, after the LINAC, in the MEBT and in the MR and a current transformer for continuous beam (CTS, see Sec. 3.1.2) in the MR.

The CTAs measure an average current I over a certain pulse time t. From this the number of particles can be calculated via

$$N = \frac{Itn}{e}$$

with the elementary charge e and the number of particles per elementary charge n. Table 4.2 shows the number of particles per elementary charge at the different current transformers. The H_3^+ molecule is considered as three protons. If this was not the case, one would observe an increase in the number of particles at the stripping foil, where the H_3^+ splits into 3 H^+, which would make the calculation of a transmission rather unintuitive.

The determination of the number of particles in the CTS is made difficult by the changing velocity (and therefore current) of the particles during the acceleration. The current I of N particles with a revolution period of τ_{rev} and a charge per particle q is

$$I = \frac{qN}{\tau_{rev}} = \frac{qN\beta c}{L}$$

	n	
CTA	hydrogen	carbon ions
LE	3	1/4
LI	3	1/4
ME	1	1/6
MR	1	1/6

Table 4.2: Number of elementary charges per particle for hydrogen and carbon ions in the different current transformers.

with the relativistic β, the speed of light c and the circumference of the accelerator L

$$\Rightarrow N = \frac{IL}{qc}\frac{1}{\beta} \tag{4.7}$$

The difficulty is to obtain the changing β throughout the whole acceleration cycle. The implemented system to achieve this uses the so called *B-train*. It consists of an additional synchrotron dipole which is connected to the same power supply as the real ones and equipped with magnetic field probes to measure the magnetic field B during the acceleration. The relativistic β can then be obtained starting with the definition of the magnetic rigidity $B\rho$:

$$B\rho = \frac{p}{q} = \frac{\gamma m_0 \beta c}{q}$$

and with $\gamma = \frac{1}{\sqrt{1-\beta^2}}$ this can be rearranged to:

$$\beta = \frac{1}{\sqrt{1 + \left(\frac{m_0 c}{B\rho q}\right)^2}} \tag{4.8}$$

so when inserting eq. 4.8 into eq. 4.7 we arrive at:

$$N = \frac{IL}{qc}\sqrt{1 + \left(\frac{m_0 c}{B\rho q}\right)^2} \tag{4.9}$$

therefore by measuring the B-field of the synchrotron dipoles, the number of particles can be directly calculated from the measured CTS current since all other variables in eq. 4.9 are constant.

In the last step the transmission of the number of particles N_i between a point 1 in the accelerator and a later point 2 is calculated as:

$$T_{1,2} = \frac{N_2}{N_1}$$

4.2.1 RF-train

The analysis of the transmission for the pulsed beam current transformers (CTAs) uses the PACMAN level two `CTA` module. Per design the CTS uses the B-train to calculate the number of particles from the measured current as shown in eq. 4.9. At the moment the B-train unfortunately does not work reliably. To still get reliable particle counts over the whole acceleration cycle, the PACMAN `CTS` module has been upgraded during this thesis, with the implementation of the so called *RF-train*.

The basic idea behind this concept is, that the velocity of the particles can not only be determined by the strength of the B-field needed to keep them on a closed orbit but also by their revolution frequency. The number of particles can then be calculated via:

$$N = \frac{I}{q f_{rev}}$$

When performing the analysis of a CTS measurement, the implemented `RFtrain` function automatically looks for the corresponding SLC[1] measurement and then performs analysis on the measured frequency channels to obtain a matching of the measured CTS current to the measured RF frequency.

In Fig. 4.3 the result of this calculation is shown for a proton beam. It can be clearly seen, that while the current increases during the acceleration, the number of particles stays constant (apart from losses).

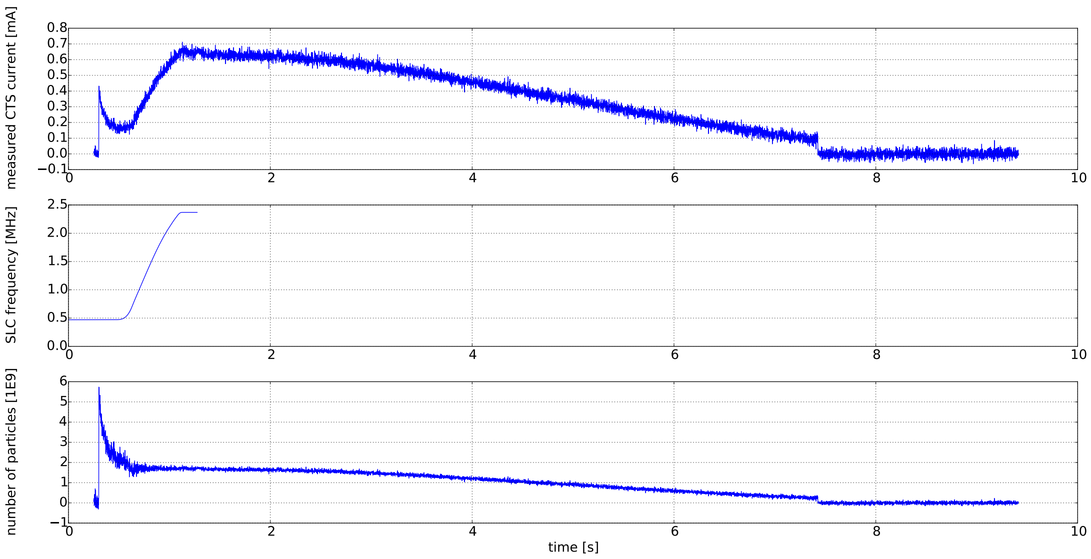

Figure 4.3: Measured CTS current (top), measured SLC frequency (middle) and computed number of particles (bottom) for a 252.7 MeV proton beam.

---

[1] Synchrotron Low level RF Cavity

5 Measurement analysis procedures

In this chapter the analysis tools developed and used during this thesis will be presented. For the developed tools, simulations were performed to test the accuracy and estimate the errors in the analysis.

5.1 PACMAN - The MedAustron measurement data analysis framework

Since the measurement analysis tools developed and used over the course of this work are implemented as part of MedAustron's PACMAN framework, the following section shall give an overview over the structure of this whole framework [21].

During the commissioning and the operation of the accelerator, various digital signals from the different beam monitors and other accelerator components need to be analyzed. To streamline this process and provide a standardized implementation of complex analysis procedures, a dedicated analysis framework has been developed at MedAustron: *PACMAN* - Python Algorithms Coded for Measurement data ANalysis.

All modules in the PACMAN framework follow a common level structure consisting of four levels (outlined below) and a common support modules library. The support modules provide functionality like a logger, specific error handling, helper functions for file filtering and decryption of control system codes as well as various other functionality for curve fitting, fast Fourier transformation or implementation of external code such as MAD-X.

Level one
This level handles the reading of different input file formats. Most of the data acquired by the beam diagnostics measurement devices follow the MedAustron Exchange File Format (`.msr`-files). It defines the file structure including header, meta data and measurement data to be stored in a human readable style.

Level two
Modules of this level analyze the data of a single measurement. For each measurement device (beam diagnostic monitor) there is a specific module. All level two measurement device classes follow a standardized analysis workflow to ease the combination of measurements from different device types.

Level three
Modules of this level process and analyze the data of multiple single measurements. Typically they also follow the standardized structure of the level two tools, albeit not necessarily as strictly.

Level four

This level presents the functionality of some PACMAN modules in the frame of a graphical user interface to the users. It acts as an application launcher for PACMAN modules.

5.2 Injector emittance analysis

The development of the analysis tool for slit-grid measurements as described in Sec. 4.1.1 has not been part of this thesis. The used tool `InjectorEmittance.py` is a level three tool in the PACMAN framework developed at MedAustron. Over the course of this thesis only minor adaptations to the analysis code and measurement procedure were performed. A detailed description of the analysis tool can be found in Kerschbaum [22], the basic principles will however be summarized in the following.

The analysis procedure is based on so called self-consistent unbiased elliptical exclusion analysis (SCUBEEx). This method reduces the data used for the computation of the emittance by creating a so called exclusion ellipse and ignoring all data outside of the ellipse for the RMS emittance calculation. The data outside of the exclusion ellipse is used to estimate the offset of the profile monitor measurement.

Since the slit-grid method directly measures the trace-space, the σ-matrix of the beam distribution (see Sec. 1.4.5) can be calculated directly from the data inside of the exclusion ellipse. The RMS emittance is equal to the square root of the determinant of the σ-matrix (see eq. 1.17). The Twiss parameters α, β, γ can be calculated as well with their relationships to the σ-matrix as seen in eqs. 1.18 - 1.20.

5.3 Main Ring emittance analysis procedure

The analysis tool for the synchrotron emittance measurements developed over the course of this thesis, has been implemented as a level three module in the PACMAN framework named `MRemittance.py`. Additionally level two functionality for some of the used measurement devices (scraper plates - SCX) has been implemented as well, since the PACMAN framework did not contain classes to handle measurement data from these devices. One goal of this analysis tool was, to be able to obtain the transverse synchrotron emittance from a single sided scraping measurement[1]. This allows the use of only partially complete data and has the advantage of reducing the influence of cycle-to-cycle variations due to being only dependent on a single acceleration cycle.

Part of this work has been presented at the 7th International Beam Instrumentation Conference in Shanghai in Adler et al. [23].

---

[1] This means that the analysis can be performed independently for each scraper plate (which move in from opposite directions) and allows the use of measurements even if only one of the two scraper plates produced a valid measurement.

5.3.1 Analysis outline

In section 4.1.2 on page 30 the basic measurement procedure to obtain the transverse synchrotron emittance via scraping has been described. To recapitulate, the emittance can be calculated as

$$\epsilon = \frac{\sigma_{beam}^2}{\beta}$$

and with the relationship between the RMS of the betatron amplitude distribution and the beam size

$$\frac{\sigma_{betatron}^2}{\sigma_{beam}^2} = 2$$

this becomes

$$\epsilon = \frac{\sigma_{betatron}^2}{2\beta} \tag{5.1}$$

To obtain the synchrotron emittance the analysis work flow therefore follows these steps:

1. Map the beam current signal from the CTS to the corresponding position of the scraper plate.
2. Process the obtained signal to make it usable.
3. Estimate the center of the beam from the signal curve.
4. Calculate the numerical derivative of the signal.
5. Compute the RMS of the obtained betatron amplitude distribution.
6. Calculate the geometric and normalized emittance from the betatron amplitude RMS.

5.3.2 Simulation procedure

In the following the accuracy and the errors introduced by the different analysis steps shall be investigated. This has been done by simulating a beam current signal while scraping from an assumed Gaussian particle distribution (Gaussian both in x and x'). Therefore before diving deeper into the analysis procedure the basic algorithm for carrying out these simulations shall be presented, while specific simulation constraints will be discussed in the respective sections.

All simulations were completely done in Python 3.4[24] and since they do not rely on any external particle tracking code the simulation code was built directly into the `MRemittance.py` module, to also serve as a unit testing tool for future releases.

The simulation algorithm takes the following input parameters:

- Geometric emittance ϵ [m rad]
- Twiss α-function
- Twiss β-function [m]
- Number of simulated particles
- Movement range of the scraper [m]
- Speed of the scraper [m/s]
- Whether noise on the signal should be simulated as well [True/False]
- Magnitude of the noise [standard deviation relative to signal height]

The beam parameters used for the simulations were the design values of $\alpha = -0.13$ and $\beta = 8.76\,\mathrm{m}$, and geometric emittance values between 0.66 and $1.43\,\pi\,\mathrm{mm\,mrad}$ representing the highest and lowest design emittances.

At first the particle distribution is created using ϵ, α and β and the number of particles, assuming a Gaussian distribution in both the x and x' plane. Then the scraper plate is moved through its specified movement range with the specified speed. All particles which have a betatron amplitude larger than the aperture limitation given by the scraper blade are assumed to be scraped. This is a reasonable assumption, since the particles have a revolution period in the order of μs and the scraper and CTS have a sampling rate of 1 ms, therefore allowing the particles to at least make a few hundred turns, after which it is almost certain that the particle on its trajectory along the phase space ellipse will have hit the scraping plate. The estimation of the error made by this assumption has already been covered in Sec. 4.1.2.1 on page 31 and is below 0.1 %.

Fig. 5.1 shows an example of this simulated scraping with 10^5 simulated particles.

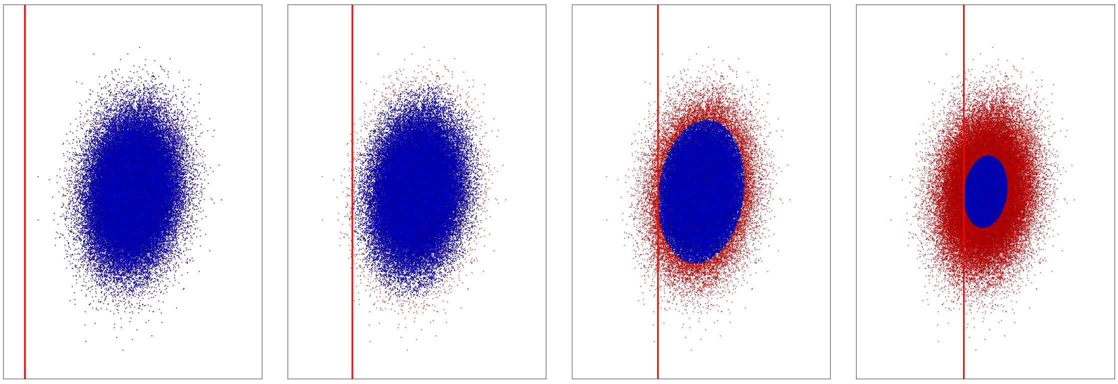

Figure 5.1: Example of a simulated particle distribution (blue dots) and a scraper (red line) moving through it from the left. The red dots show the particles which have been scraped.

5.3.2.1 Number of simulated particles

All simulations in the following sections were carried out using 10^5 particles. The reasoning for this decision can be seen in Fig. 5.2. A simulated particle count of 10^5 shows a reconstruction reliability comparable to higher particle numbers while still having a relatively short simulation time with just over 4 s.

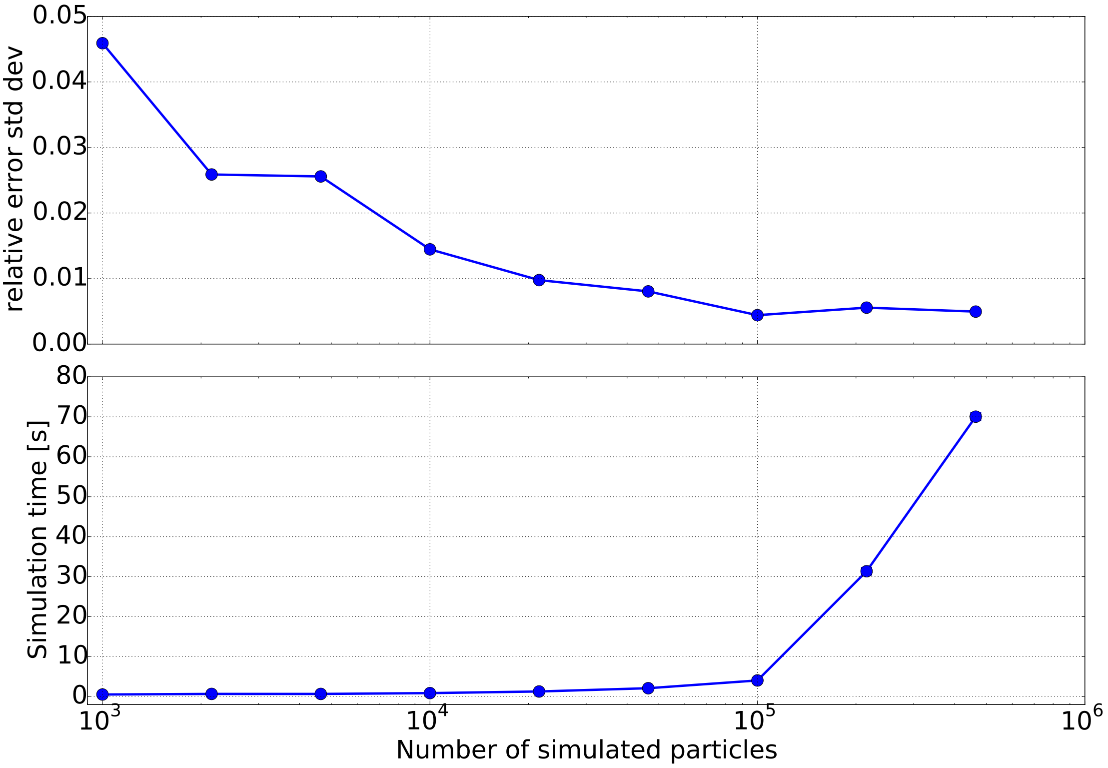

Figure 5.2: The value plotted in the top graph shows the standard deviation of the relative error $(\epsilon_{out} - \epsilon_{in})/\epsilon_{in}$ for 10 simulation runs. It represents a figure of merit for how different the reconstructed emittance results are between individual simulation runs and should be as small as reasonably achievable. On the bottom the needed time for one single simulation run is shown as a function of the number of simulated particles.

5.3.3 Mapping of the signal to the scraper position

The mapping of the CTS signal to the position of the scraper is straight-forward, since the accelerator control system broadcasts all timing events (including the starting of the scraper movement). Since the CTS and the scraper have a sampling rate of 1 ms, the mapping of the two signals is just a matter of synchronization, which can easily be done via the timing events which both components receive and report.

The timing events can also be used to extract from the measurement data directly whether the scraping was performed at flatbottom or at flattop[2]. If the *StartScraping*

---

[2] The names *flatbottom* and *flattop* refer to the beginning and end of the acceleration cycle respectively. The frequency of the circulating particles is kept constant during and shortly after the injection (flatbottom) and between the end of the acceleration and the beginning of the extraction from the synchrotron (flattop). Therefore the emittance at flatbottom is interesting with regards

timing event arrives before the *StartAcceleration* timing event, a flatbottom measurement was performed and therefore different β-functions and a different beam energy need to be taken into account for the further analysis.

5.3.4 Signal processing

Before being able to calculate the numerical derivative of the CTS current signal to obtain the betatron amplitude distribution, the signal needs to be smoothed via a moving average filter to suppress the influence of the noise. The use of a high frequency filter was also tested, but led to less favorable results than the moving average smoothing.

The need for this smoothing can be immediately seen in Fig. 5.3, where the obtained derivative is shown with and without moving average smoothing of the CTS signal. Even in the case of a measurement with a degrader setting of 100 % (no degradation), representing the best possible signal to noise ratio, the derivative is completely dominated by the noise, leading to the betatron amplitude distribution being hardly detectable.

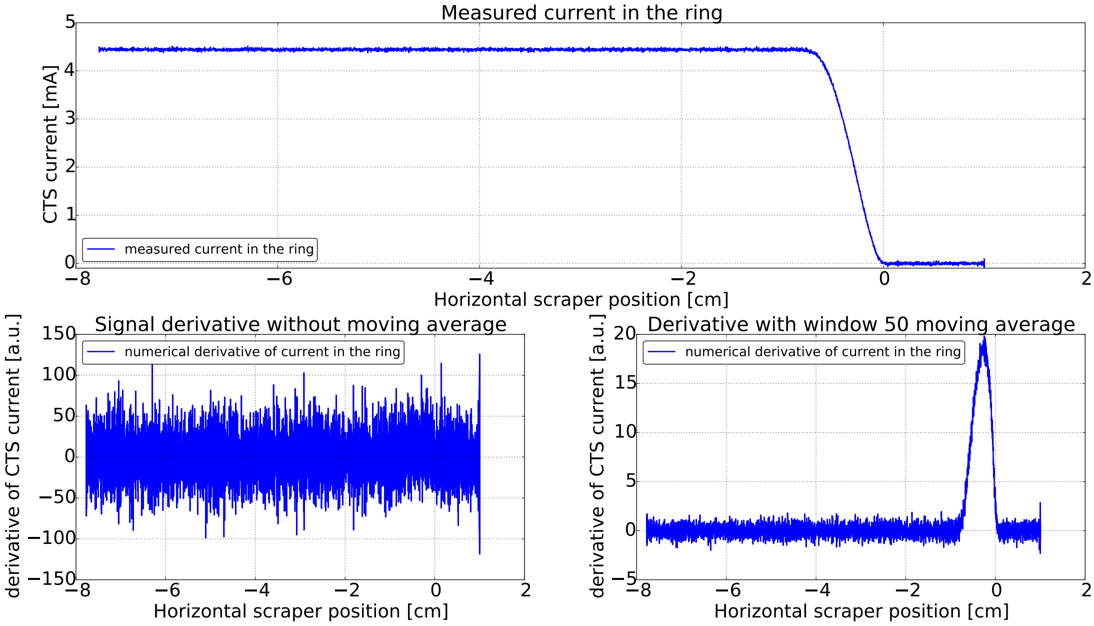

Figure 5.3: Raw CTS signal for a DEG100 400 MeV/n carbon ion beam (top). Numerical derivative of the signal (bottom left) and numerical derivative with a moving average filter with an averaging window of 50 applied to the signal before derivation (bottom right).

5.3.4.1 Systematic error introduced by moving average

Introducing a moving average smoothing will introduce a systematic error in the emittance reconstruction as well. The effect is two-fold: Firstly the edge of the beam is smoothed out and therefore the point where the CTS signal drops to zero is shifted

---

to the injection setup, while a deviation of the flattop emittance can hint at problems during the acceleration to a later scraper position, introducing an error in the estimation of the beam center (this will be covered in Sec. 5.3.5.3 where the different methods to estimate the beam center are investigated). Secondly the smoothing alters the signal and could therefore introduce an error in the reconstruction.

To separate the two factors and determine solely the influence of the second effect, the error of the emittance reconstruction has been determined as a function of the moving average window as seen in Fig. 5.4. For these simulations the real beam center is assumed to be known and therefore the systematic error introduced by the "smearing out" of the beam edge should have no influence.

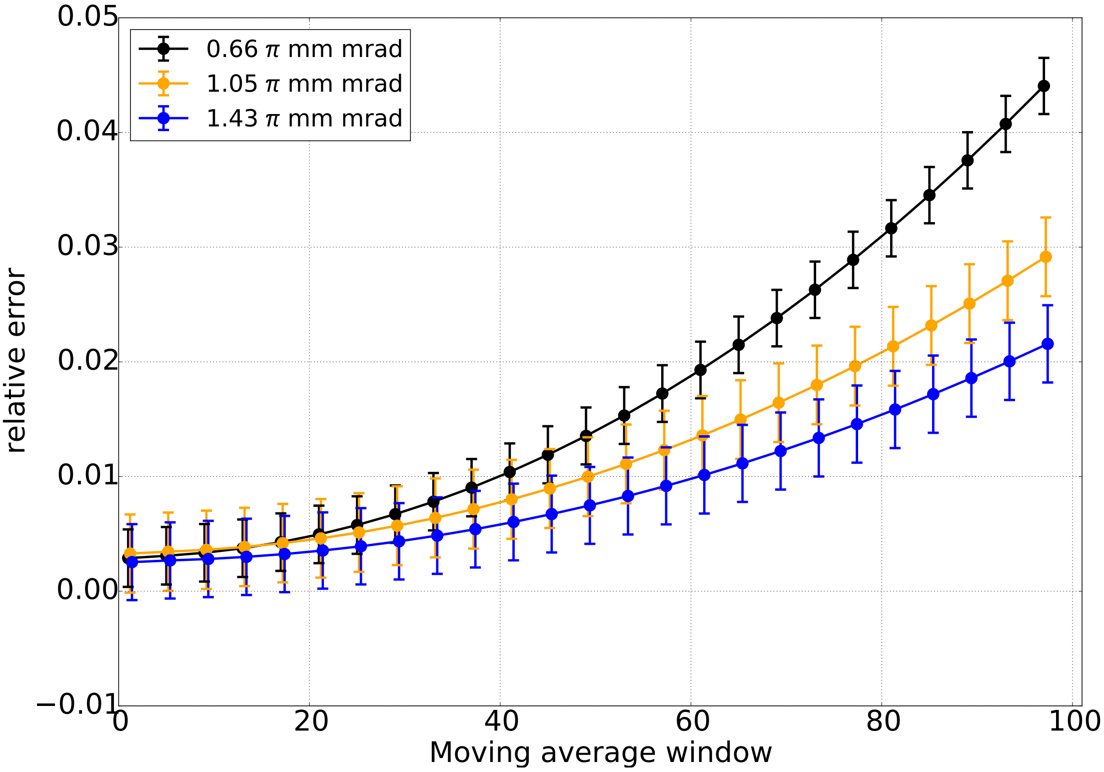

Figure 5.4: Relative error in emittance reconstruction for simulated data as a function of the moving average window showing only the influence of the signal alteration. The beam center is assumed to be known to separate the effect of the shifting of the beam center from the effect of the signal alteration. Each datapoint represents the average of ten individual simulation runs.

It can be seen that, as expected the reconstruction error increases with more aggressive smoothing of the signal. The introduced error is also larger, the smaller the emittance which can be intuitively understood: the smaller the emittance (i.e. the smaller the beam), the shorter the time during which the scraper is inside the beam and therefore the less relevant signal is obtained. The shorter the signal, the stronger the influence of the smoothing.

For typical moving average windows of 30 to 70 (the choice for these values will be explained in Sec. 5.3.8) the error introduced by this effect is fairly small, staying below 2.5 %.

5.3.4.2 Simulation of the noise

In Fig. 5.5 a zoomed section of the CTS signal shown in Fig. 5.3 is depicted along with its Fourier transform and the distribution of the current. From the Fourier transform and the histogram it can be seen, that the noise on the CTS signal is Gaussian white noise. Based on this, for simulations including the signal noise it was simulated as additive normally distributed noise with a mean of 0 and a standard deviation depending on the to be simulated degrader setting.

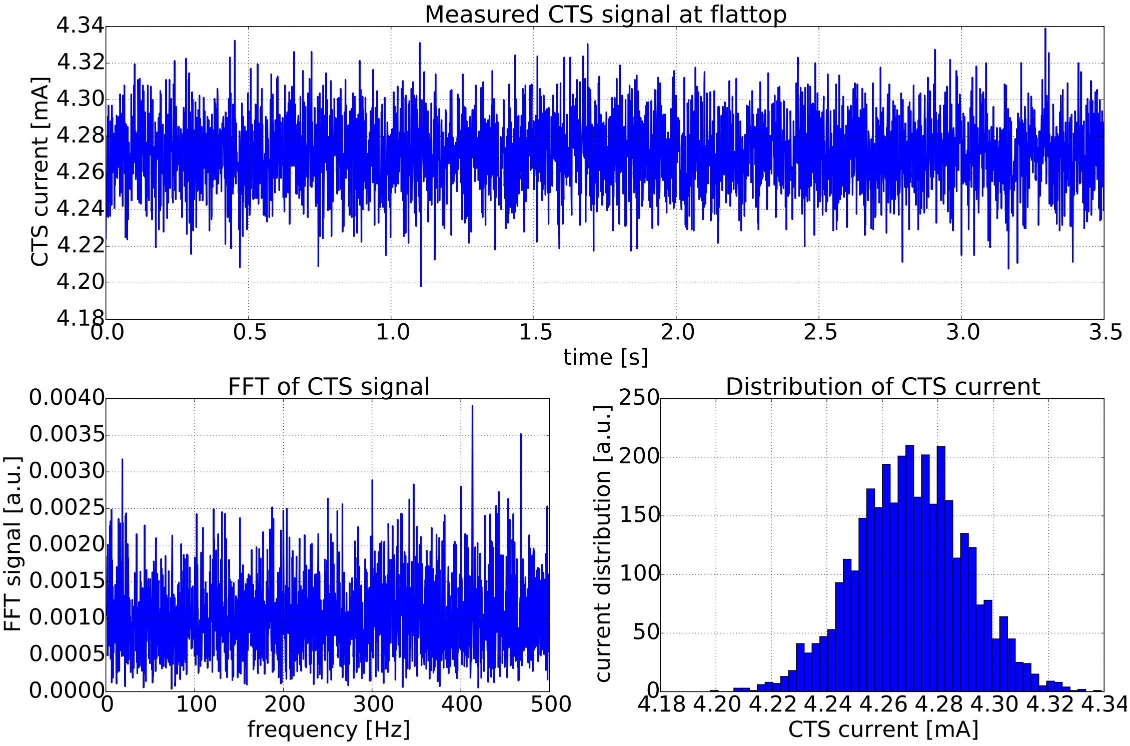

Figure 5.5: CTS signal at flattop (top), Fast Fourier Transform (FFT) of the signal (bottom left) and histogram of the CTS current (bottom right).

The magnitude of the signal noise does not depend on the strength of the signal, therefore yielding higher signal to noise ratios for higher CTS current, as can be seen in Fig. 5.6. Since the simulations for different degrader settings yield the same "signal strength" (due to the constant number of particles used for the simulations), the distinction between the different degrader settings has to be introduced via the standard deviation of the added Gaussian noise. Table 5.1 summarizes the chosen noise standard deviations used for the different degrader settings.

5.3.5 Estimation of the beam center

The emittance of the beam is according to eq. 5.1 on p. 40 directly dependent on the variance of the betatron amplitude distribution, which due to its asymmetric shape is strongly influenced by the estimated center of the beam.

In Fig. 5.7 the significant influence of the accuracy of the beam center estimation on the emittance reconstruction is shown. For example for an acceptable error in

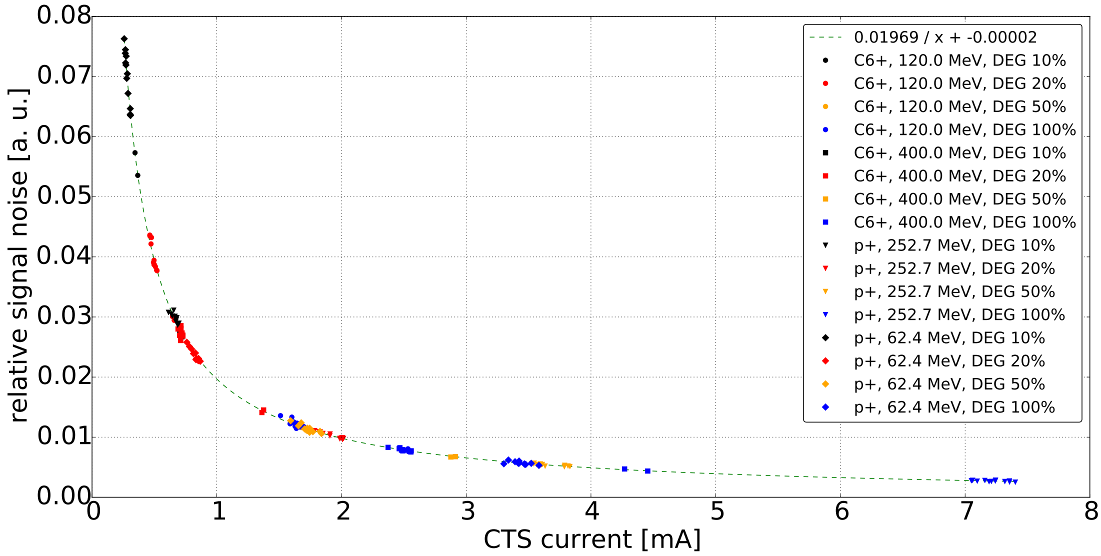

Figure 5.6: Relative standard deviation of the signal as a function of the signal strength for protons and carbon ions of the respective top and bottom clinically used extraction energies and all degrader settings.

Degrader	rel. noise stdev
100 %	0.005
50 %	0.01
20 %	0.025
10 %	0.05

Table 5.1: Relative noise standard deviation used for the different degrader settings.

the emittance reconstruction of 10 %, the beam center must be estimated with an accuracy below 0.15 mm.

To guarantee a good and robust estimation of the beam center, multiple algorithms have been implemented which will be presented in the following:

- Position measurement with pick-up
- First negative
- Curve fit
- Flank detection
- Manual modes

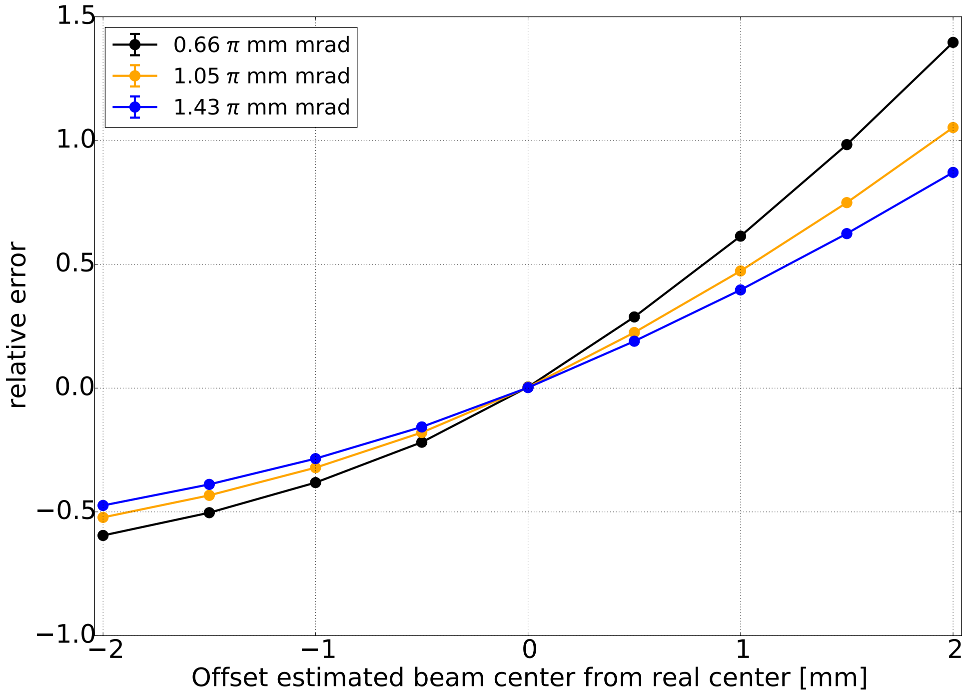

Figure 5.7: Impact of the accuracy of the beam center estimation on the emittance reconstruction. For this simulation the beam center has been hardcoded into the analysis algorithm. Each datapoint is an average of ten individual simulation runs.

5.3.5.1 Position measurement with pick-up

In the synchrotron there are shoebox pick-ups installed close to the scraping plates (see Sec. 3.2.2 on page 26 for a description of the pick-ups). They record the mean position of the particles (and therefore the beam center) as long as the beam is bunched (i.e. captured by the synchrotron RF cavity). Unfortunately during the scraping measurement the RF cavity is turned off so the particles can move freely longitudinally and therefore no position signal during the scraping process is recorded. However, the last position before the shut off of the cavity can be taken as an estimation of the beam center. The beam center obtained with this method can also be used as a starting parameter input for a curve fit described in Sec. 5.3.5.3.

5.3.5.2 First negative

The simplest implemented algorithm for the estimation of the beam center searches for the first scraper position where the CTS signal is negative. The reasoning behind that is, that the signal can only get negative due to the noise and only when there are almost no particles left. Since this method gives surprisingly unreliable results in the emittance reconstruction, it is only used as an input for the starting parameter for the curve fit described in Sec. 5.3.5.3 if the pick-up signal is not available.

5.3.5.3 Curve fit

If one assumes the beam profile to be Gaussian and includes the fact that the measurement is done in a non-dispersive region of the ring, the beam current signal can be analytically described by a function of the form

$$\frac{I(x)}{I_0} = \left(1 - \exp\left(-\frac{(x-x_0)^2}{2\beta\epsilon}\right)\right)\Theta\left(x - x_0\right) \tag{5.2}$$

with the Heavyside-function Θ and the center of the beam x_0. The idea of describing the CTS signal by this curve is basically to approximate the beam by a Gaussian distribution with a standard deviation of $\sqrt{\beta\epsilon}$. Since β and the order of magnitude of ϵ are assumed to be known, fitting eq. 5.2 to the beam current signal gives quite reliable estimations of the beam center, as can be seen for a real measurement in Fig. 5.8 where eq. 5.2 is fitted to the signal shown in Fig. 5.3 (top).

For measurements at flatbottom where the beam is not yet captured by the synchrotron RF cavity, the problem of natural beam losses has to be taken into account. The circulating beam loses particles approximately linearly over time even without scraping. To still allow a meaningful curve fit, the curve shown in eq. 5.2 is extended by an additional linear term with a slope k, which is 1 at the starting position of the scraper x_{Start}. The curve used for flatbottom measurements is shown in eq. 5.3.

$$\frac{I(x)}{I_0} = \left(1 - \exp\left(-\frac{(x-x_0)^2}{2\beta\epsilon}\right)\right)(1 - k(x - x_{Start}))\Theta\left(x - x_0\right) \tag{5.3}$$

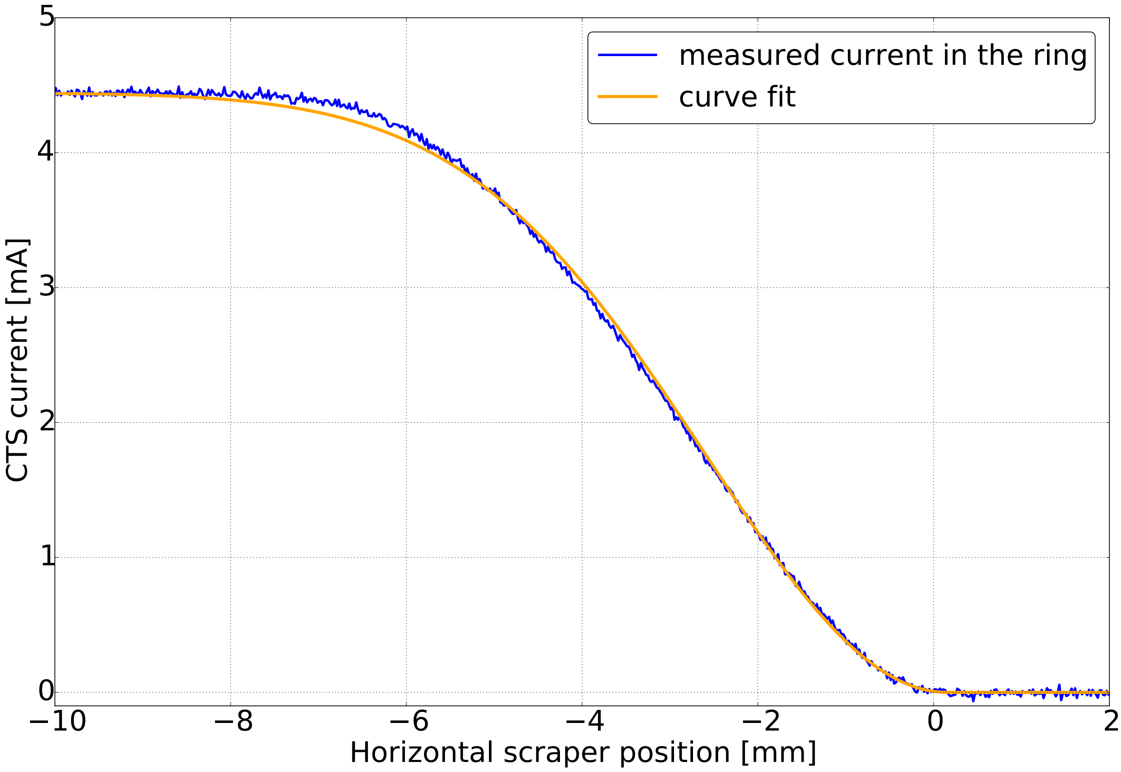

Figure 5.8: Eq. 5.2 fitted to a real measured CTS signal of a 400 MeV/n carbon ion beam at 100 % degrader setting. Especially in the most relevant region of the beam center the curve fits very well.

For simulations without any noise, this method gives excellent reconstruction accuracy with relative errors below 1 %, as can be seen in Table 5.2.

ϵ	reconstructed ϵ	relative error [%]
0.66	0.662 ± 0.005	0.35 ± 0.71
1.045	1.049 ± 0.009	0.47 ± 0.85
1.43	1.435 ± 0.009	0.38 ± 0.63

Table 5.2: Relative errors in reconstruction for the ideal case simulation with no noise. Geometric emittances given in π mm mrad.

As mentioned in Sec. 5.3.4.1 the systematic error introduced by the moving average smoothing is also influenced by the fact that the beam center is smeared out to later scraping positions. The combined effect of the signal alteration (see Fig. 5.4) and the shifting of the beam center can be seen in Fig. 5.9. It can be seen that it should be desirable to choose a moving average window as small as possible to reduce the systematic error.

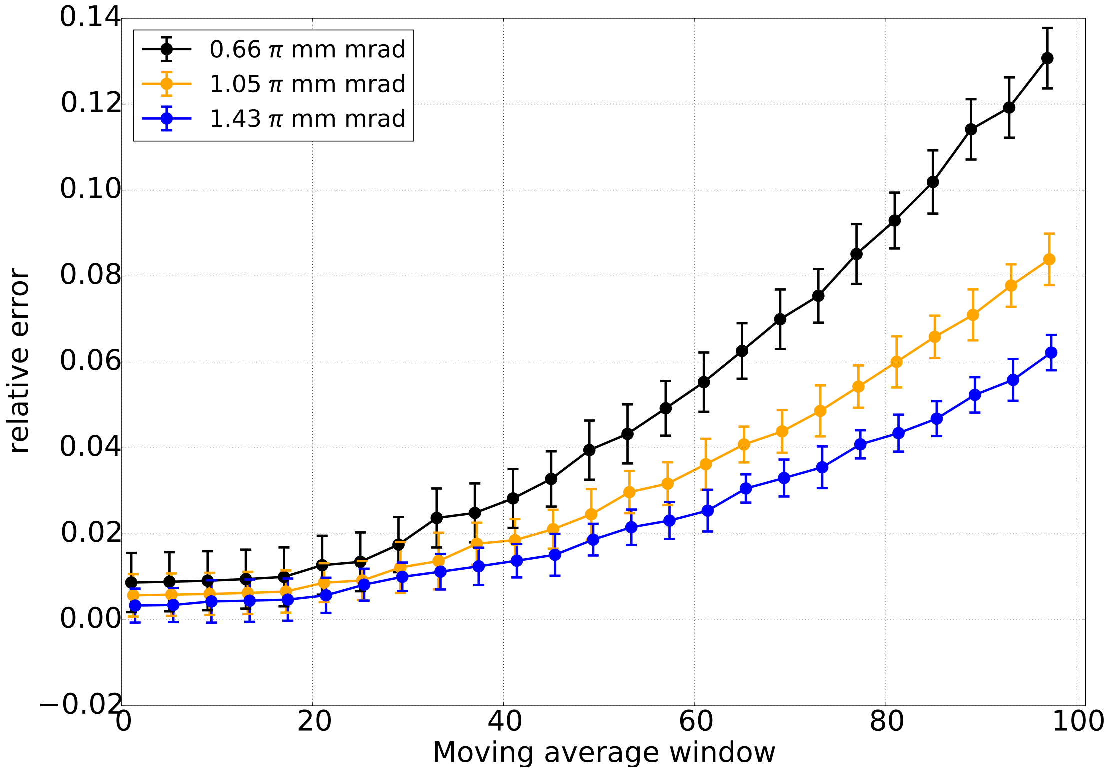

Figure 5.9: Relative error in emittance reconstruction for simulated data as a function of the moving average window showing the combined effect of the shifting of the beam center and the signal alteration as described in Sec. 5.3.4.1. The beam center is computed via the curve fit algorithm. Each datapoint represents the average of ten individual simulation runs.

5.3.5.4 Flank detection

A basic algorithm to compute the beam center was also implemented. It "walks" through the CTS signal from the scraped (i.e. zero signal) end and checks whether a number of consecutive points are above a threshold defined by the standard deviation of the signal noise. If that is the case, the rising flank of the signal has been detected, which should coincide with the beam center.

Naturally this method becomes less reliable the lower the signal to noise ratio on the CTS, a circumstance which can be seen in Fig. 5.10, where the relative emittance reconstruction error gets very large for lower degrader settings.

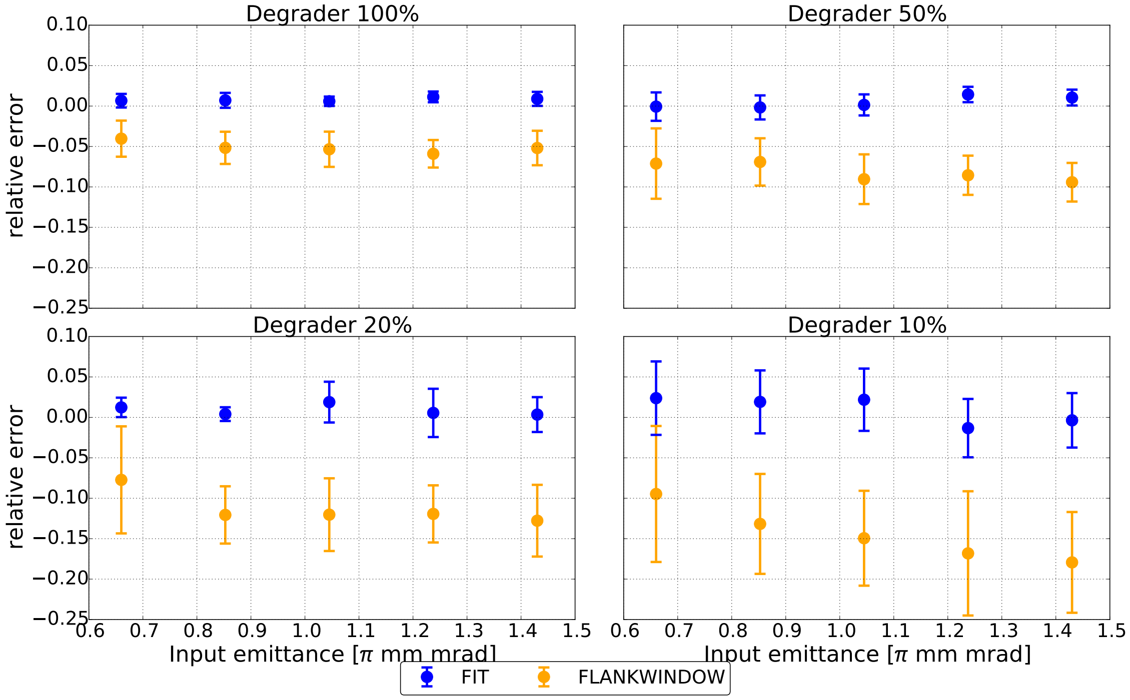

Figure 5.10: Comparison of the curve fit ('FIT') and flank detection ('FLANKWINDOW') beam center estimation methods. What can be seen directly is, that the curve fit gives much more reliable results, especially for lower degrader settings.

5.3.5.5 Manual modes

Should none of the above methods give satisfying results, two ways to get the beam center via user input have been implemented: the first one allows a simple input of the beam center as an analysis parameter and the second one presents the user with a plot of the raw signal with the possibility to manually select the estimated position of the beam center.

5.3.5.6 Conclusion

The curve fit and flank detection algorithms are on average approximately equal for low noise measurements, with the curve fit offering higher reliability in the reconstruction (see the smaller errorbars in Fig. 5.10). For lower degrader settings (higher relative noise) however, the accuracy of the flank detection dramatically drops, while the curve fit does not worsen as much on average. The reliability of the curve fit, also gets worse the lower the degrader setting. This fact may be seen much clearer, by the large error bars for low degrader settings in Fig. 5.11.

Therefore to obtain the best emittance reconstruction results, the usage of the curve fit method in conjunction with the fit input of the pick-up signal is recommended.

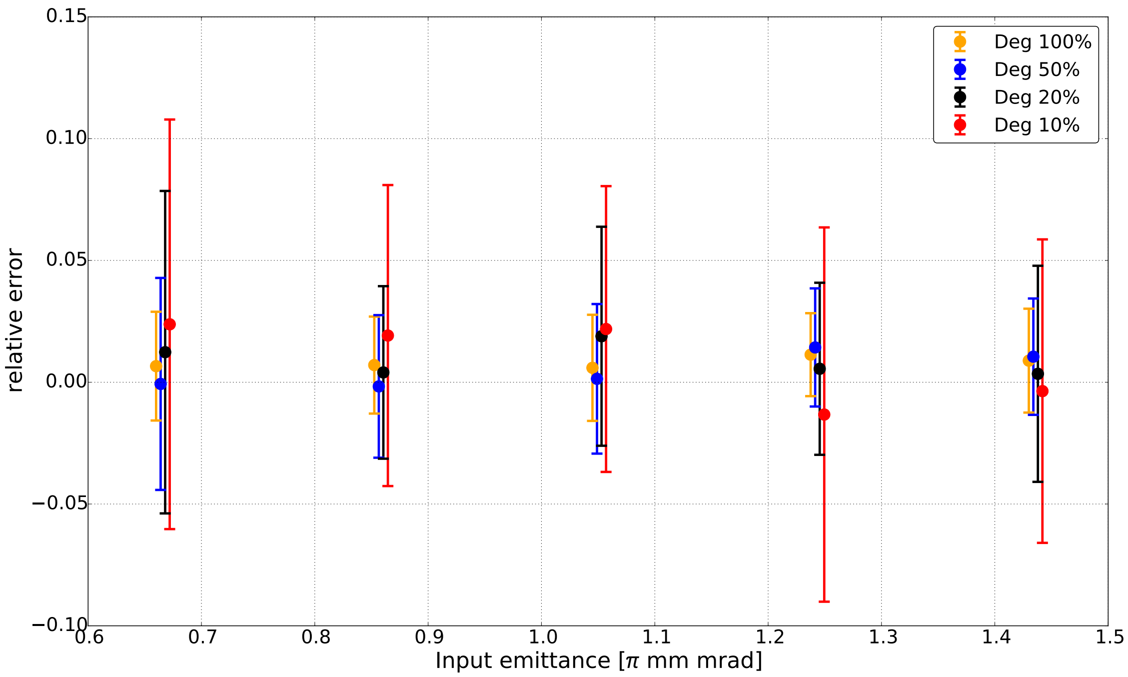

Figure 5.11: Accuracy of the emittance reconstruction of the curve fit method for different degrader settings.

5.3.6 Computation of the emittance

After calculating the numerical derivative of the CTS signal (which can be done directly using Python's numpy module), the only thing missing before being able to compute the geometric emittance is the calculation of the RMS of the betatron amplitude distribution.

For this computation, only the part of the distribution between the estimated beam center and the beginning of the falling flank of the CTS signal is considered. All values which have a probability smaller than zero are set to zero since they are only an effect of the noise.

After obtaining the geometric emittance by dividing the RMS by two times the assumed β-function, the normalized emittance (see Sec. 1.4.4.1 on p. 12) has to be calculated to make measurements taken at different beam energies comparable. Since the cycle code encodes the beam energy per nucleon and is included in the measurement data files the relativistic β and γ can be calculated easily via:

$$\gamma_{rel} = \frac{E_{tot}}{E_{rest}}$$

$$\beta_{rel} = \sqrt{1 - \frac{1}{\gamma_{rel}^2}}$$

$$\epsilon_{norm} = \beta_{rel}\gamma_{rel}\epsilon_{geo}$$

5.3.7 Reconstruction of the positional distribution

The result of the scraping measurement is the distribution of the betatron amplitude of the particles. But if we go back to the solution of Hill's equation of motion (eq. 1.10 on p. 7):

$$x(s) = \sqrt{\epsilon}\sqrt{\beta(s)}\cos(\Psi(s) + \Phi)$$

one can see, that the position of the particles $x(s)$ varies in a cosine like motion dependent on the betatron phase advance $\Psi(s)$ with an amplitude equal to their betatron amplitude $\sqrt{\epsilon\beta(s)}$.

So in order to obtain the average positional distribution of the particles, one has to modulate the betatron amplitude distribution with the spectrum of a cosine distribution of equally distributed angles (phase advances). This is shown graphically in Fig. 5.12. The way this is done computationally is by creating a uniform distribution of angles in $[0; 2\pi]$ and assigning the angles to each betatron amplitude, by relative weight. The product of the cosine of the so assigned angles with their respective amplitude results in the average positional distribution of the particles.

This has no impact on the computation of the emittance, but the beam shape can still be a factor of interest. Especially for measurement which are difficult to analyze, the shape of the resulting positional distribution can serve as a quick feedback to the user, since artifacts of a wrong beam center estimation can be immediately seen.

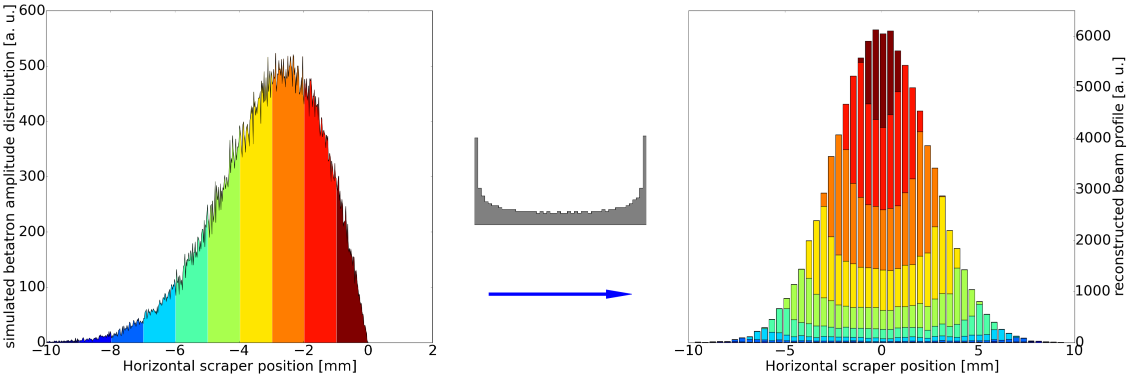

Figure 5.12: Basic principle of the reconstruction of the positional particle distribution (right) from their betatron amplitude distribution (left) by modulating with a cosine spectrum (center) for a simulated Gaussian particle distribution.

5.3.8 Optimal analysis parameters

In Sec. 5.3.5.6 we already found, that the best analysis mode is using the curve fit method with an input of the pick-up signal. The other significant analysis parameter left to determine is the window of the moving average which should be used for the different degrader settings. As shown above, the moving average introduces a systematic emittance reconstruction error while also reducing the disturbing effects of the noise. Therefore the goal should be to find a good compromise between these two effects, which is expected to be different for varying noise levels.

Fig. 5.13 shows the relative error in emittance reconstruction as a function of the moving average window for different simulated degrader settings. The proposed moving average windows were chosen in order to give comparable results for all emittances and to be consistent over as many degrader settings as possible. The results are summarized in table 5.3.

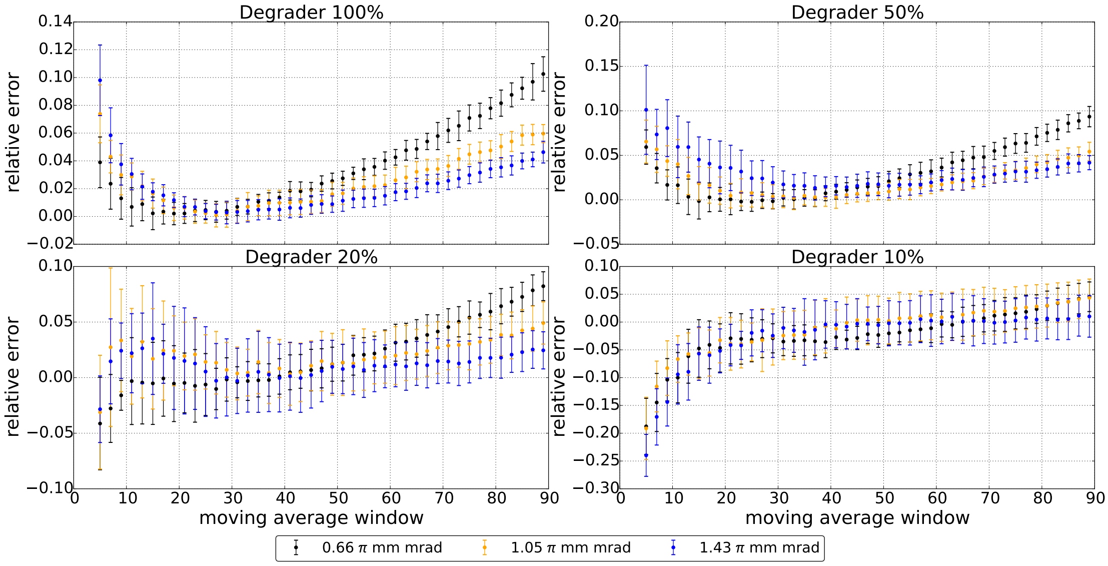

Figure 5.13: Relative emittance reconstruction error for different simulated degrader settings as a function of the moving average window to determine the optimum trade-off point between the systematic error of the smoothing and the effect of the noise.

Degrader	mov. avg. window
100 %	30
50 %	30
20 %	50
10 %	50-70

Table 5.3: Proposed optimal moving average window sizes for the four degrader settings.

5.3.9 Visualization

After the analysis is finished, the results as well as the raw data are presented to the user in a combined plot. An example for such a plot can be seen in Fig. 5.14. The figure is separated into three subplots and a table containing the analysis results and beam parameters.

The top subplot shows the CTS current over the scraper position for both scraper plates (in this case h1 and h2). If the curve-fit analysis method has been selected, the result of the analytic fit is also shown. Two colored boxes show the region of interest for the computation of the betatron amplitude RMS. Only data points within these regions are considered. Ideally the distance between the inner edges of the two boxes should be as small as possible, indicating a good agreement between the two individual scraping measurements.

The middle subplot shows the numerical derivative of the CTS signal, the regions of interest, as well as the derivative of the analytic curve-fit (if this method has been selected). The derivative of the curve-fit has no influence on the analysis result and merely acts as a visual feedback to the user how well the curve fits the data.

The bottom subplot shows the computed positional distribution of the particles. Any potential error in the beam center estimation can be immediately spotted here, due to the curves visibly deviating from an approximately Gaussian shaped distribution. An underestimation of the beam center would lead to a central spike and an overestimation to two symmetric spikes in the distribution.

The table on the right side shows information about the measured particle beam by displaying the cycle code (CC), energy, degrader setting and particle type. This is followed by three analysis parameters, namely the assumed horizontal and vertical β-functions and the selected analysis mode. The last three rows show the computed geometric and normalized emittances per scraper plate as well as the estimated beam center. Behind the brackets the method which was used to find the center is displayed. In most cases this should coincide with the selected analysis method, but if for whatever reason one of the methods fails, the tool automatically defaults to the next one in order of accuracy.

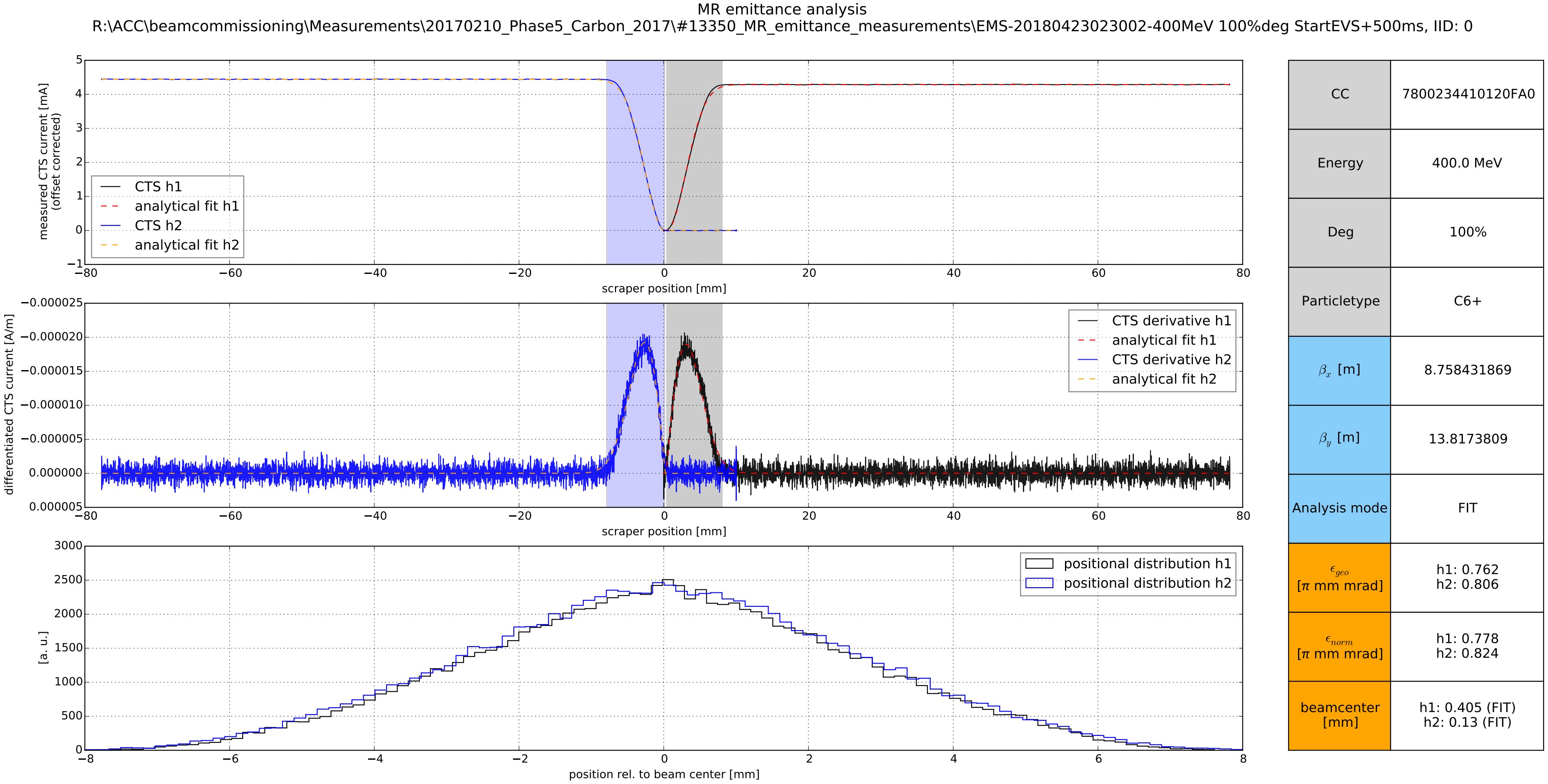

CC	7800234410120FA0
Energy	400.0 MeV
Deg	100%
Particletype	C6+
β_x [m]	8.758431869
β_y [m]	13.8173809
Analysis mode	FIT
ϵ_{geo} [π mm mrad]	h1: 0.762 h2: 0.806
ϵ_{norm} [π mm mrad]	h1: 0.778 h2: 0.824
beamcenter [mm]	h1: 0.405 (FIT) h2: 0.13 (FIT)

Figure 5.14: Example of a summary plot produced by the `MRemittance.py` tool.

5.4 Transfer line emittance analysis procedure

As part of this thesis, a new python module for the analysis of quadrupole scan data has been developed, named `QuadScan.py`. Due to the fact that it also relies substantially on MAD-X python implementations, it has not been incorporated into the PACMAN framework. The tool is still structured like any level three PACMAN module as well as being version controlled.

The reliable analysis of quadrupole scan data is very important during the commissioning of the transfer lines to obtain the Twiss parameters and center the beam in the quadrupole. It is also very useful for quality assurance purposes, especially since the offset of the beam in the quadrupoles can be determined as well, which might change over time.

The used monitors for this type of measurement are scintillating fiber hodoscopes (SFX, see Sec. 3.2.3 on page 27) in the HEBT and secondary electron emission grids (PGX, see Sec. 3.2.4 on page 28) in the MEBT. Both of these monitor types have a wire spacing of 1 mm in both planes.

5.4.1 Analysis outline

To obtain the Twiss parameters and especially the emittance, a function of the form:

$$\sigma_2^2 = A(B - kl)^2 + C$$

as derived in eq. 4.4 has to be fitted to the squared RMS beam sizes (which are equal to the variance of the beam profile distribution) as a function of the quadrupole strength k. The fit parameters together with the transfer matrix between the quadrupole and the monitor are sufficient to calculate α, β and ϵ. Additionally the offset of the beam in the quadrupole can be estimated by applying a linear fit to the beam center positions as a function of the quadrupole strength as outline in eqs. 4.5 and 4.6.

To summarize, the necessary steps to obtain the analysis results are:

1. Correlate the measured quadrupole strengths with the individual beam profile measurements.

2. Obtain the beam distribution for each quadrupole strength by summing up all individually measured single frames.

3. Calculate the mean and variance of the distributions and their uncertainties using Gaussian error propagation.

4. Calculate the transfer matrix using MAD-X and lattice files.

5. Fit the quadratic and linear functions to their respective quantities and calculate the Twiss parameters and the offset from the fit results.

The above outlined steps shall now be explained in further detail:

1. The first step can be achieved with the use of the so called *loopfile*. This file serves as an input to the *Operational Application*[3] providing the quadrupole strengths which are to be measured and their order. The analysis tool subsequently needs to perform a mapping of this strength order to the order in which the individual measurements were taken.

2. The second step can be carried out directly with the use of the respective PGX or SFX PACMAN modules which can return the summed up counts per fiber for each plane.

3. The mean and the variance can be calculated with the standard formulas for weighted measurements:

$$m = \frac{1}{\sum_i w_i} \sum_i w_i x_i$$

$$v = \frac{1}{\sum_i w_i} \sum_i w_i (x_i - m)^2$$

where x_i are the positions of the individual fibers and w_i their respective weights (counts). To estimate the standard error on the mean and variance, the uncertainty introduced by the binning due to the wire spacing has to be propagated using Gaussian error propagation. The complete derivation of the following formulas has been carried out in the appendix in Sec. A.2.

The uncertainty of the position on each single fiber is equal for all fibers and with a wire spacing of 1 mm amounts to (see eq. A.2):

$$\sigma_x = \frac{1}{\sqrt{12}} \, \mathrm{mm}$$

Using this and neglecting any uncertainty in the counts, the standard error on the mean can be calculated as (see eq. A.3):

$$\sigma_m = \sigma_x \sqrt{\frac{\sum_i w_i^2}{\left(\sum_i w_i\right)^2}}$$

And following that, the standard error on the variance (see eq. A.4):

$$\sigma_v = \frac{2}{\sum_i w_i} \sqrt{\sigma_x^2 \sum_i w_i^2 (x_i - m)^2 + \sigma_m^2 \left(m \sum_i w_i - \sum_i w_i x_i \right)^2}$$

The curve fit is later performed using the `scipy`[25] package. This package allows the propagation of error on the data and returns the standard uncertainties on the fit parameters.

---

[3] The Operational Applications are a software framework developed at MedAustron to automatically perform repetitive beam measurements, e.g. changing a quadrupole strength and measuring a beam profile.

4. The calculation of transfer matrices is a standard procedure of MAD-X. The position of elements in the MedAustron accelerator are specified in so called *lattice files*. A python wrapper for MAD-X exists, using the `cpymad`[26] library. Loading the correct lattice file and finding the quadrupole and beam monitor allows the calculation of the transfer matrix. This loading of the correct files and locating of the elements is done completely automatic and does not require any input from the user.

5. Fitting the function from eq. 4.4 to the beam variance and a linear function to the beam position is done using the `scipy` package. Special care has to be taken to invert the strength for the vertical plane due to the sign convention of the quadrupole strength being positive for a horizontally focusing quadrupole.

The `scipy` package returns the standard errors on the fit parameters, which are then translated into the standard errors on the Twiss parameters as well as the offset using Gaussian error propagation.

The normalized emittance can be calculated from the geometrical emittance as already shown for the synchrotron emittance analysis in Sec. 5.3.6.

5.4.2 Simulation procedure

To test the accuracy of the developed analysis tool, varying beam distributions created with python were tracked through a basic beam line using MAD-X. The beam line was kept as simple as possible to speed up the particle tracking, while still resembling a realistic set-up. The beam line consists of a single quadrupole of length $l = 0.25\,\mathrm{m}$ at position $x = 0$ and a beam profile monitor with a wire spacing of 1 mm at position $x = 3\,\mathrm{m}$, leaving a drift space of 2.75 m between the exit of the quadrupole and the monitor. The monitor was simulated to resemble a scintillating fiber hodoscope as installed in MedAustron's HEBT, meaning 64 fibers with a wire spacing of 1 mm resulting in a coverage of the profile monitor of ±32 mm. The layout of the simulated beam line can be seen in Fig. 5.15.

All simulations using particle tracking were carried out with 10^4 particles per beam distribution.

5.4.3 Accuracy of the beam offset reconstruction

To simulate how accurate the analysis procedure can reconstruct an offset of the beam from the quadrupole optical axis, a series of simulations were run, adding a flat offset in the range of ±10 mm to the beam distribution. The Twiss parameters for the used beam distribution were: $\alpha = 0$, $\beta = 5\,\mathrm{m}$ and $\epsilon = 1\,\pi\,\mathrm{mm\,mrad}$. The results of these simulations can be seen in Fig. 5.16, where the absolute error of the offset reconstruction is shown as a function of the offset. For expected offsets from the optical axis in the range of ±5 mm the error is reasonably small, being in the order of 0.2 mm for higher offsets.

For a normal distribution with a standard deviation of $\sqrt{\beta\epsilon} \approx 2.2\,\mathrm{mm}$ the standard

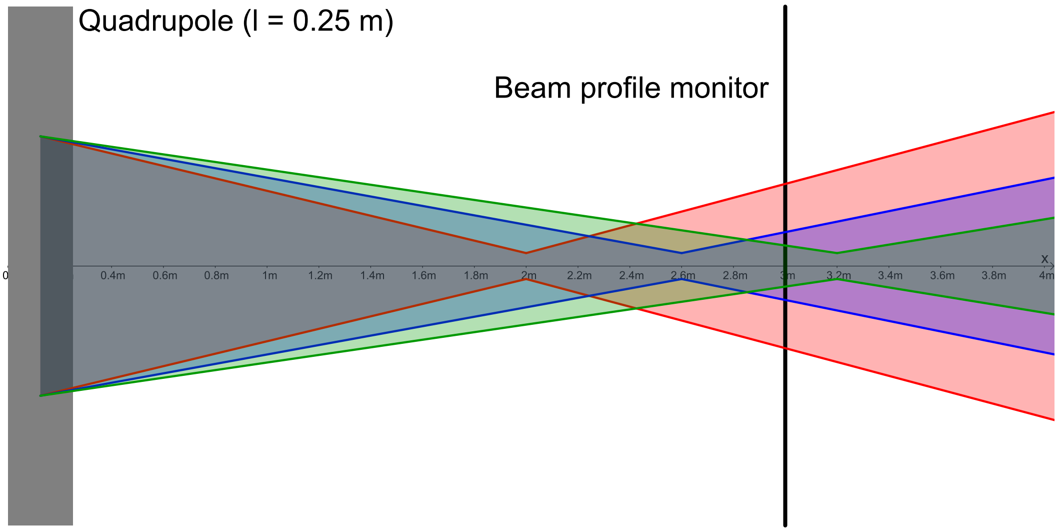

Figure 5.15: Layout of the simulated beam line showing the positions of the quadrupole and the beam profile monitor as well as an example of a beam envelope for three different quadrupole strengths, showing the varying beam width at the profile monitor.

error on the beam center (with a wire spacing of 1 mm) is according to eq. A.3 $\approx$ 0.11 mm. Therefore the error in the offset reconstruction is of this order of magnitude and only marginally larger than the possible achievable accuracy of the beam center measurement.

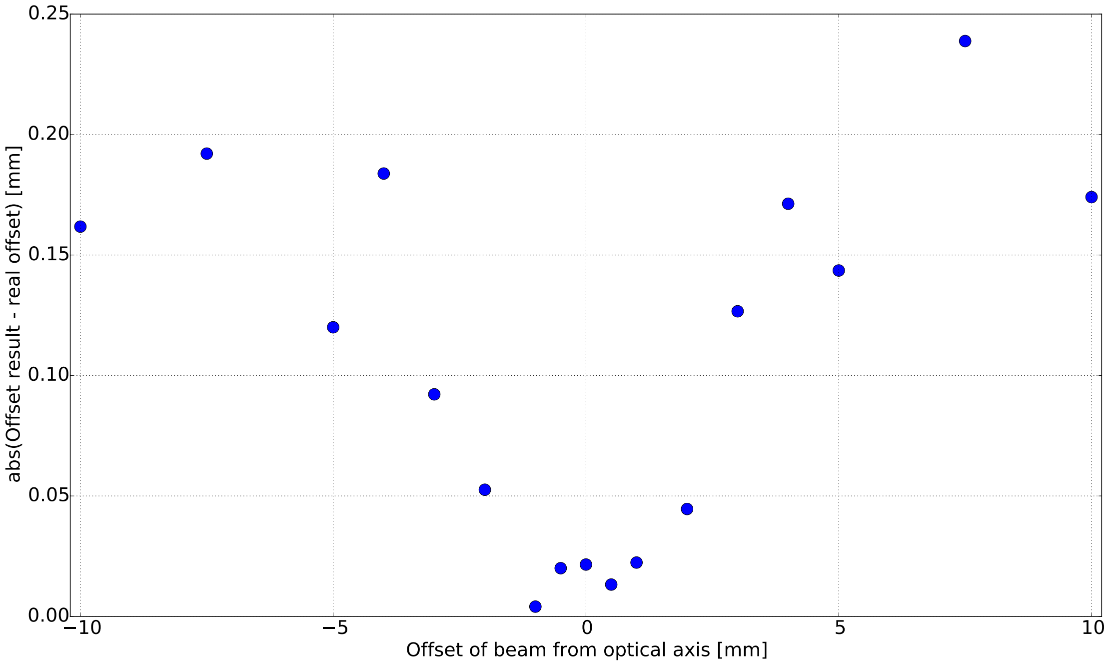

Figure 5.16: Absolute error in the offset reconstruction as a function of the offset.

5.4.4 Accuracy of the Twiss parameter reconstruction

To test how reliable the developed analysis tool can reconstruct the Twiss parameters, 25 Gaussian beam distributions with Twiss parameters of $\epsilon = 1\,\pi\,\mathrm{mm\,mrad}$, $\beta = [1, 2, 5, 8, 10]\,\mathrm{m}$ and $\alpha =$ [-1, -0.5, 0, 0.5, 1] were tracked. The initial distributions can be seen in Fig. 5.17. The quadrupole scan was simulated using 15 different normalized quadrupole strengths k ranging from -2 m^{-2} to 3.6 m^{-2}.

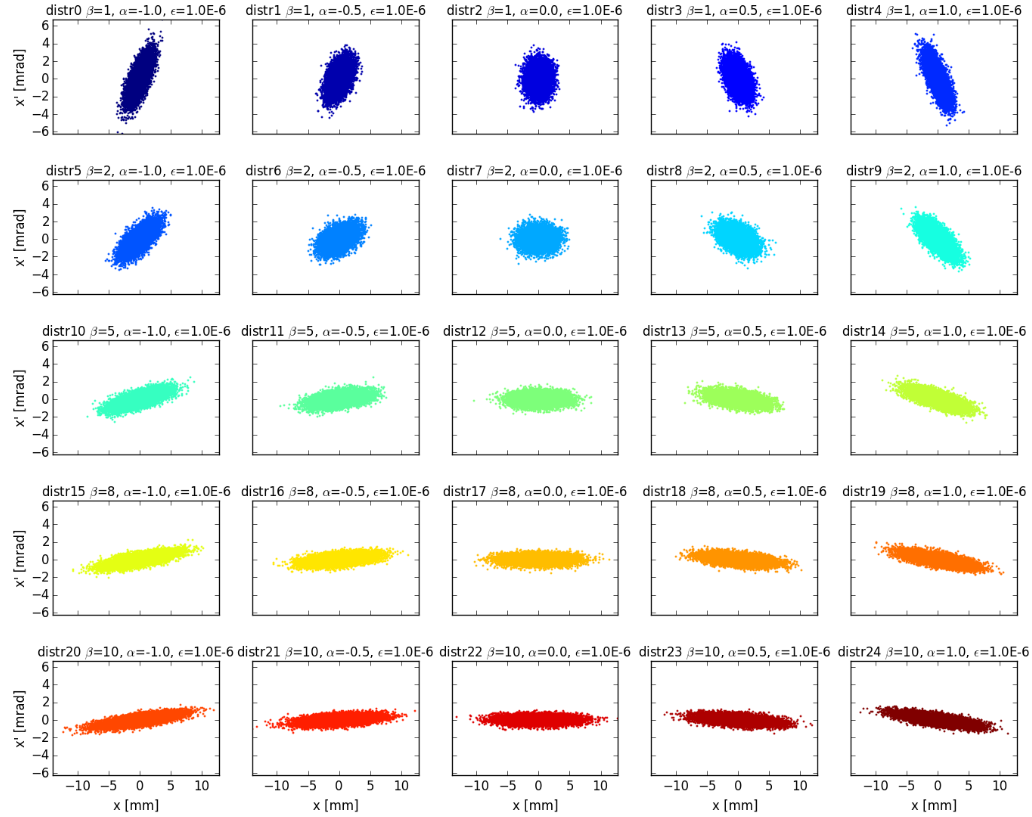

Figure 5.17: Different tracked beam distributions to cover all cases of small to large beam sizes and converging as well as diverging beams.

5.4.4.1 Accuracy of the fitting

The error in the reconstruction can have two sources: errors stemming from the measurement acquisition (i.e. resolution limit of the monitor, parts of the beam not covered by monitor, ...) and errors stemming from the analysis procedure itself (i.e. errors in the fitting or applied formulas). To separate these two sources, we should go back to the derivation of the fit function of the quadrupole scan, where it was shown in eq. 4.3 on page 33, that the beam size at the monitor σ_2 can be expressed in terms of Twiss parameters at the quadrupole (subscript 1) and the transfermatrix **R** as:

$$\sigma_2^2 = \epsilon(R_{11}^2\beta_1 - 2R_{11}R_{12}\alpha_1 + R_{12}^2\gamma_1)$$

Using this expression one can calculate the theoretical beam size σ_2 at the monitor analytically without tracking any particles and free of measurement errors, to test the accuracy of the analysis procedure alone.

The relative error in the Twiss parameter reconstruction for all distributions shown in Fig. 5.17 is in the order of 10^{-14} and therefore completely negligible (as was to be expected).

5.4.4.2 Twiss parameter reconstruction accuracy for a centered beam

In Figs. 5.18-5.20 the relative (or absolute) error of the Twiss parameter reconstruction is shown as a 2D map of the beam distribution parameters shown in Fig. 5.17. The top left and right corner fields show cases where the scan could not be performed around the beam waist, resulting in much higher errors than for any other cases.

As mentioned in Sec. 4.1.3.2 on page 33, the best results can be obtained for high β and negative α (large and divergent beam). For these cases the relative error in emittance reconstruction is at or below 3 %. In general it can be said, that the relative error in the Twiss parameter reconstruction for relatively large and diverging beams is around 10 %.

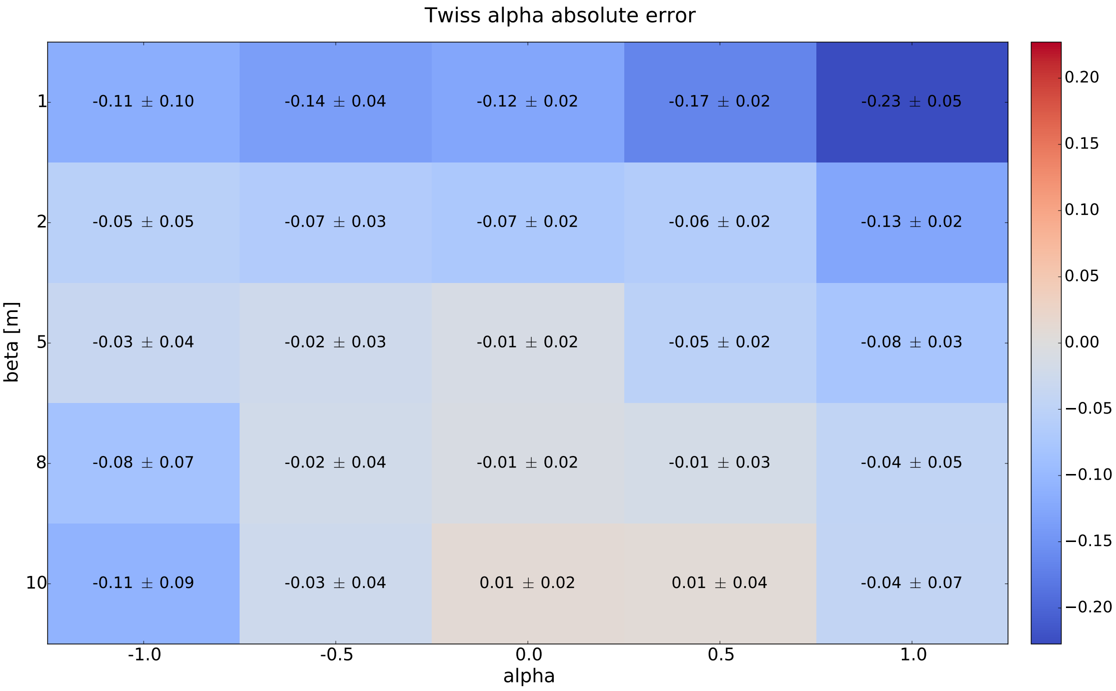

beta [m] \ alpha	-1.0	-0.5	0.0	0.5	1.0
1	-0.11 ± 0.10	-0.14 ± 0.04	-0.12 ± 0.02	-0.17 ± 0.02	-0.23 ± 0.05
2	-0.05 ± 0.05	-0.07 ± 0.03	-0.07 ± 0.02	-0.06 ± 0.02	-0.13 ± 0.02
5	-0.03 ± 0.04	-0.02 ± 0.03	-0.01 ± 0.02	-0.05 ± 0.02	-0.08 ± 0.03
8	-0.08 ± 0.07	-0.02 ± 0.04	-0.01 ± 0.02	-0.01 ± 0.03	-0.04 ± 0.05
10	-0.11 ± 0.09	-0.03 ± 0.04	0.01 ± 0.02	0.01 ± 0.04	-0.04 ± 0.07

Figure 5.18: Absolute error of the reconstructed Twiss α depending on the input beam distribution parameters. The definition of a relative error does not make sense in this case, since α is also zero. The uncertainty shown is the result of the error propagation.

5.4.4.3 Twiss parameter reconstruction accuracy for an off-centered beam

If the beam has an offset from the optical axis of the quadrupole, the particles will experience a dipole-kick depending on their distance from the axis. To test how

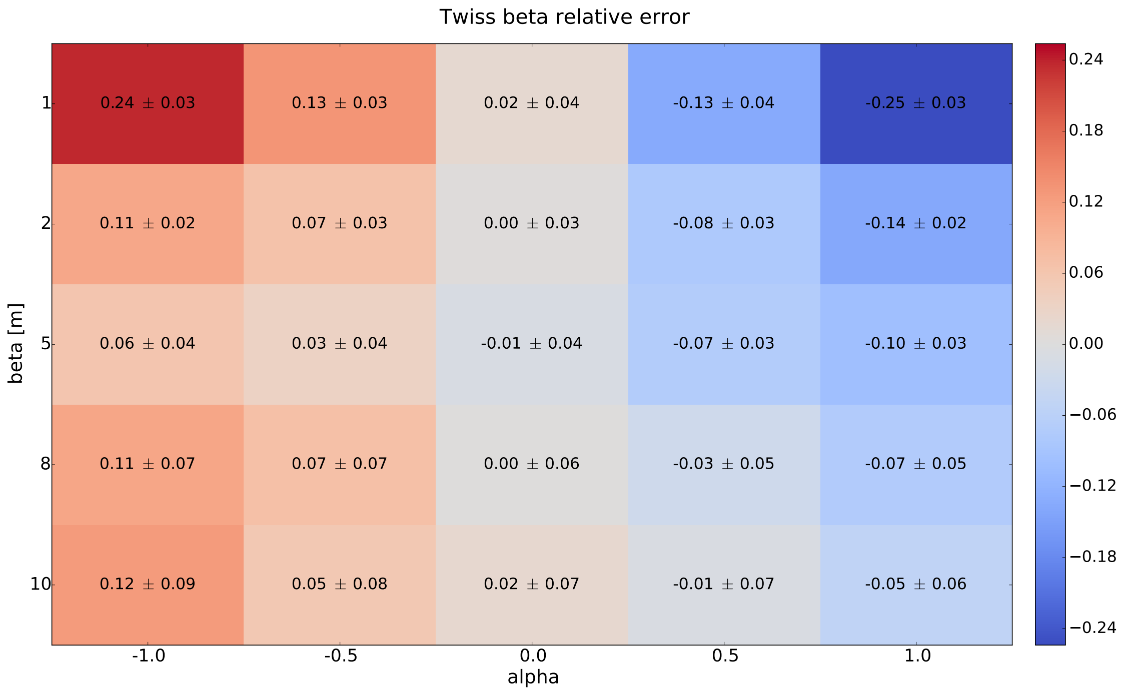

beta [m] \ alpha	-1.0	-0.5	0.0	0.5	1.0
1	0.24 ± 0.03	0.13 ± 0.03	0.02 ± 0.04	-0.13 ± 0.04	-0.25 ± 0.03
2	0.11 ± 0.02	0.07 ± 0.03	0.00 ± 0.03	-0.08 ± 0.03	-0.14 ± 0.02
5	0.06 ± 0.04	0.03 ± 0.04	-0.01 ± 0.04	-0.07 ± 0.03	-0.10 ± 0.03
8	0.11 ± 0.07	0.07 ± 0.07	0.00 ± 0.06	-0.03 ± 0.05	-0.07 ± 0.05
10	0.12 ± 0.09	0.05 ± 0.08	0.02 ± 0.07	-0.01 ± 0.07	-0.05 ± 0.06

Figure 5.19: Relative error of the reconstructed Twiss β depending on the input beam distribution parameters. The uncertainty shown is the result of the error propagation.

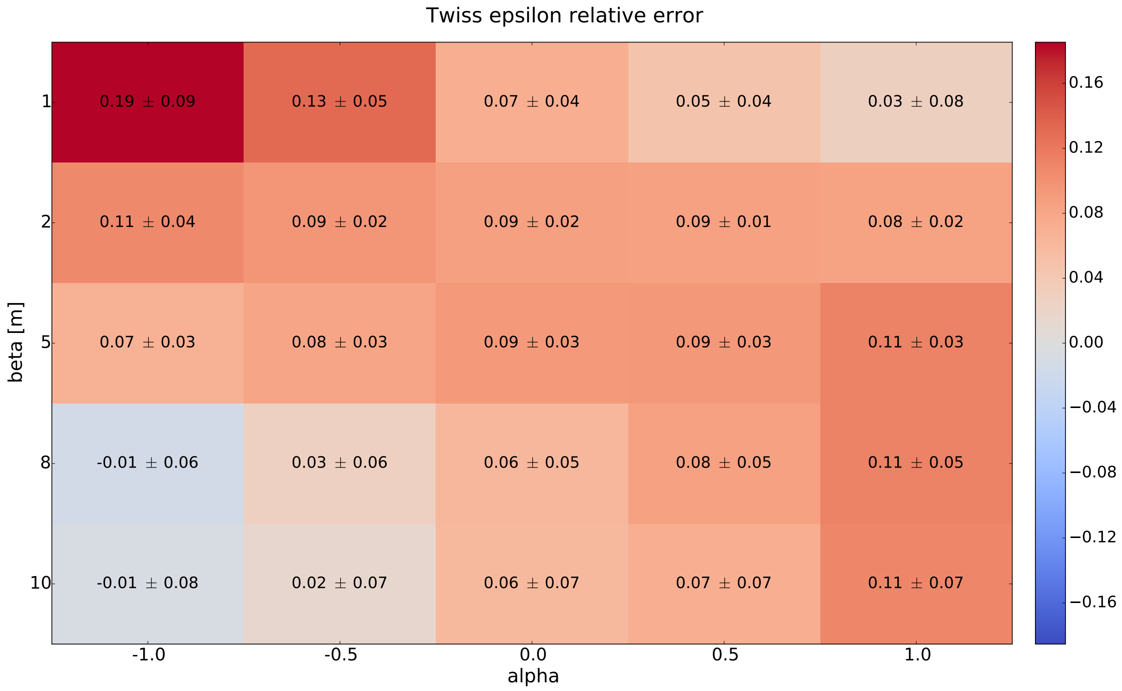

beta [m] \ alpha	-1.0	-0.5	0.0	0.5	1.0
1	0.19 ± 0.09	0.13 ± 0.05	0.07 ± 0.04	0.05 ± 0.04	0.03 ± 0.08
2	0.11 ± 0.04	0.09 ± 0.02	0.09 ± 0.02	0.09 ± 0.01	0.08 ± 0.02
5	0.07 ± 0.03	0.08 ± 0.03	0.09 ± 0.03	0.09 ± 0.03	0.11 ± 0.03
8	-0.01 ± 0.06	0.03 ± 0.06	0.06 ± 0.05	0.08 ± 0.05	0.11 ± 0.05
10	-0.01 ± 0.08	0.02 ± 0.07	0.06 ± 0.07	0.07 ± 0.07	0.11 ± 0.07

Figure 5.20: Relative error of the reconstructed Twiss ϵ depending on the input beam distribution parameters. The uncertainty shown is the result of the error propagation.

this offset influences the Twiss parameter reconstruction, the same data set used for the beam offset reconstruction accuracy in the previous subsection was used. The results are shown in Fig. 5.21. For an expected offset in the range of ±5 mm there does not seem to be a significant dependency on the beam offset.

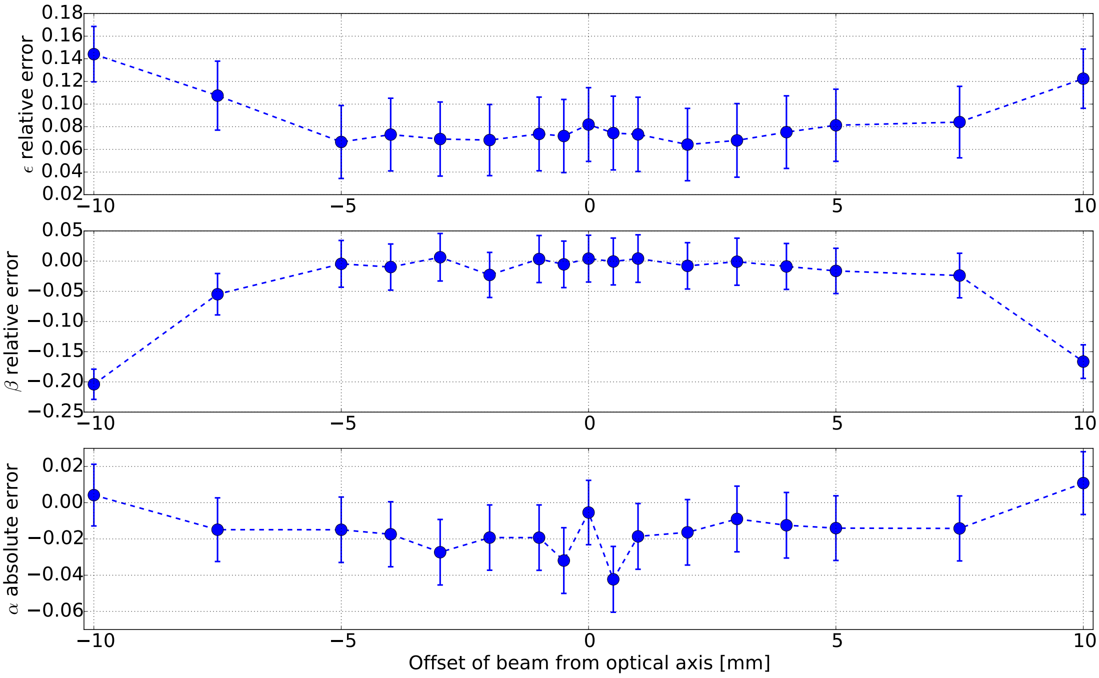

Figure 5.21: Error in the reconstruction of the Twiss parameters as a function of the offset of the beam from the quadrupole axis. The input parameters of the distribution were: $\alpha = 0$, $\beta = 5\,\mathrm{m}$ and $\epsilon = 1\,\pi\,\mathrm{mm\,mrad}$. The uncertainty shown is the result of the error propagation.

5.4.5 Radiation damage

The scintillating fibers in the SFXs installed in the HEBT experience damage of their optical properties due to the ion beams. The overall effect of the damage is proportional to the exposure dose. It leads to a loss in light yield and a reduction of the fluorescence. At higher dose exposures, it was shown that the radiation damage can lead to discoloration of the plastic, shifting of absorbing components and an increasing loss of light yield [27]. For the scintillating fibers in the extraction line this causes a significant problem: the central fibers are irradiated much stronger, leading to a non-uniform decrease in sensitivity over the range of the monitor. This subsequently leads to a distortion of the measured beam profile.

In this section the effect of the uncorrected radiation damage on the reconstruction accuracy shall be investigated. The simulations were done using the radiation damage curves for two scintillating fiber hodoscopes, namely the EX-00-000-SFX, which shows the most severe radiation damage and is therefore a worst case estimation, and the EX-01-001-SFX which is essential to the commissioning of the extraction line and therefore of special interest. The radiation damage curves for these two monitors are shown in Fig. 5.22. In the last simulation step when binning the tracked particle positions to the fiber positions, the obtained histogram was multiplied with this curve.

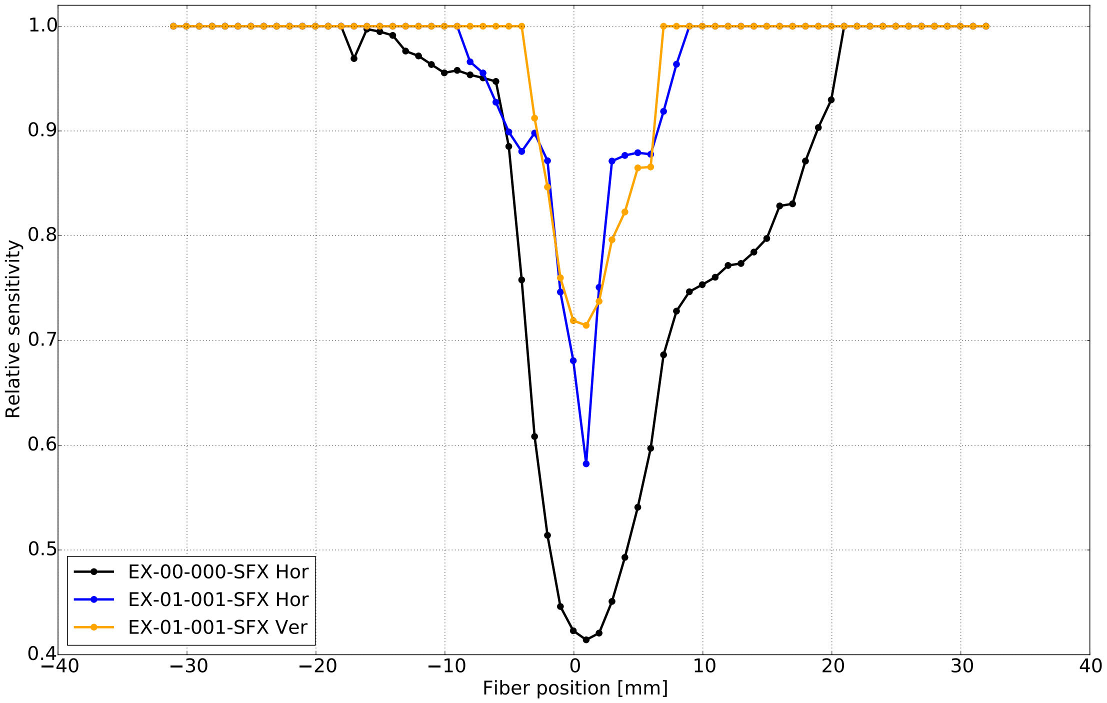

Figure 5.22: Relative fiber sensitivity of the EX-00-000-SFX and EX-01-001-SFX. The curves were obtained by scanning a beam over the monitor and normalizing the obtained intensity with the extracted current from the ring (measured by the CTS). For the EX-00-000-SFX a vertical scan can not be performed easily, due to the lack of a corrector magnet.

In Figs. 5.23-5.25 the effect of the EX-00-000-SFX radiation damage curve being applied to the 2D-scan data from Fig. 5.17 is shown. The maximum error in the reconstruction of α and β for the valid scans shows a doubling of the error to the range of 10-20 %. For the reconstruction of the emittance however, the radiation damage increases the error to up to 40 %. The reason for that is, that the decrease of the sensitivity in the central fibers gives higher weight to the external fibers, leading to a consistent increase of the beam size over the whole scan range. Since the emittance is directly proportional to the square root of the offset of the fitted parabola C, an overall increase in measured beam size leads to an increase in reconstructed emittance.

The effect of the radiation damage can also be clearly observed when looking on the error in Twiss parameter reconstruction as a function of the beam offset from the quadrupole axis as shown in Fig. 5.26. While the beam is in the center of the radiation damaged part, the already observed increase of the measured emittance can be clearly seen. When the beam is a little off-center, one edge gets higher weight than the other one, leading to an artificial angle in the beam which leads to a higher error in the α reconstruction while also underestimating the β function. As soon as the beam gets out of the most damaged part there is again a good agreement

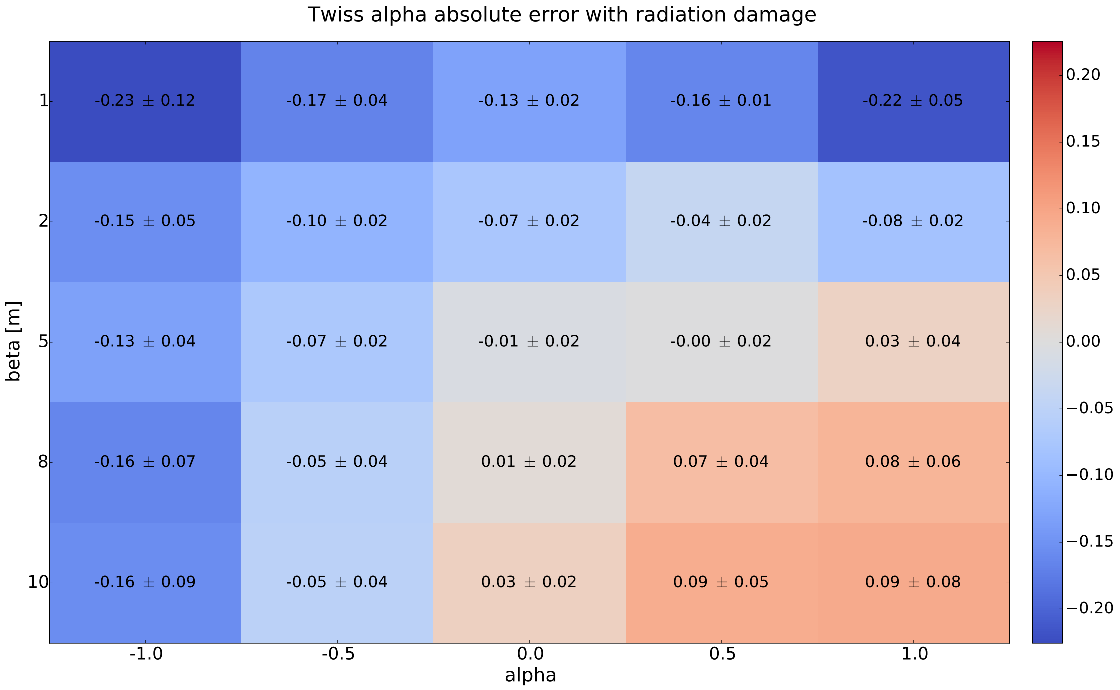

Figure 5.23: Absolute error of the reconstructed Twiss α depending on the input beam distribution parameters, with radiation damage curve included. The definition of a relative error does not make sense in this case, since α is also zero. The uncertainty shown is the result of the error propagation.

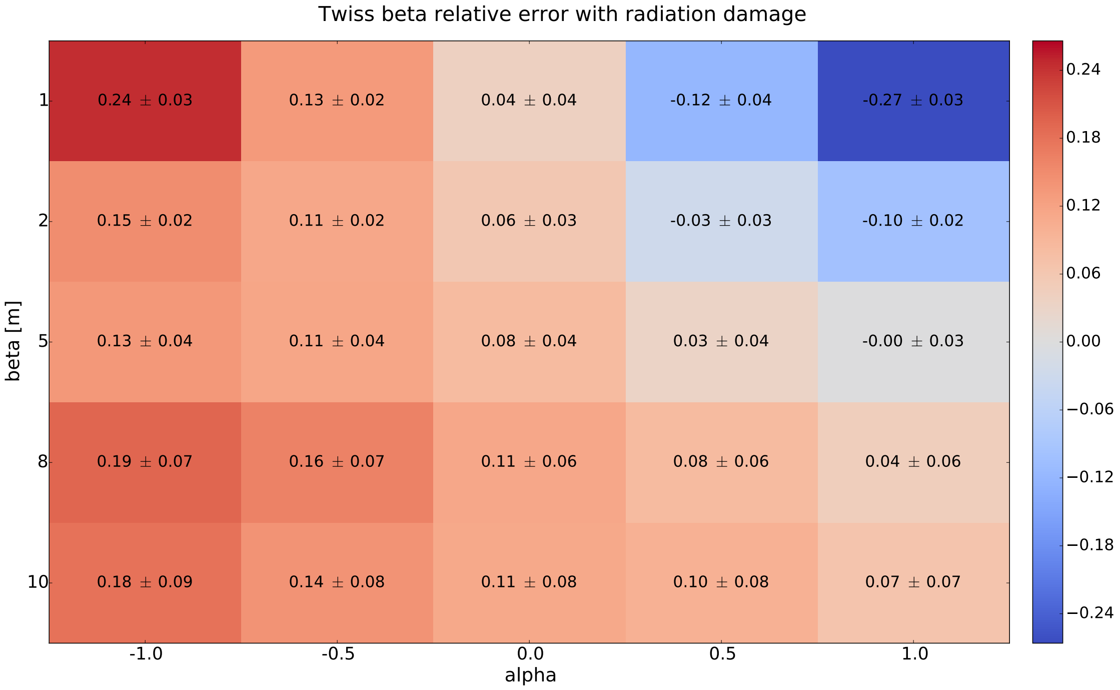

Figure 5.24: Relative error of the reconstructed Twiss β depending on the input beam distribution parameters, with radiation damage curve included. The uncertainty shown is the result of the error propagation.

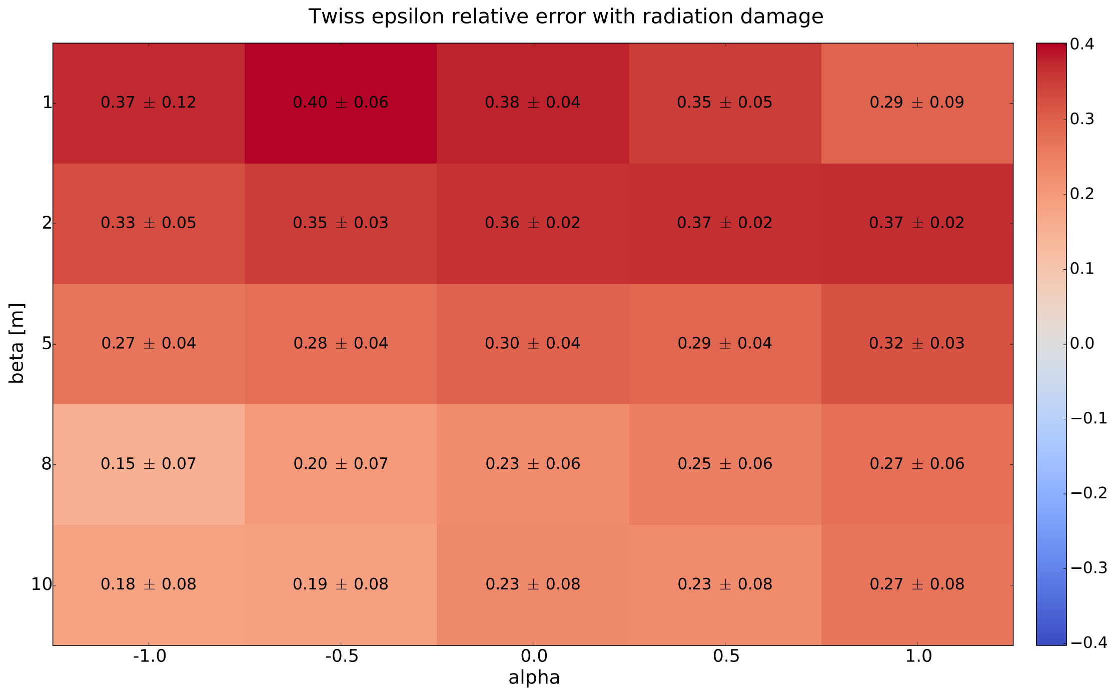

Figure 5.25: Relative error of the reconstructed Twiss ϵ depending on the input beam distribution parameters, with radiation damage curve included. The uncertainty shown is the result of the error propagation.

between the damaged and non-damaged curves.

The distortion of the beam profile also has an effect on the measured center of the beam, if the beam has an offset from the optical axis. Due to the offset the beam is moved across the monitor during the quad scan and the beam profile is distorted as a function of the quadrupole strength. The effect this has on the error of the beam offset reconstruction can be seen in Fig. 5.27.

5.4.6 Bar of charge

The horizontal beam in the extraction line does not resemble a Gaussian distribution, but the aforementioned bar of charge. To test the accuracy of the analysis tool for bar of charge like beams, the same distribution input parameters as already shown for the Gaussian case in Fig. 5.17 were used. The bar of charge was simulated as a uniform distribution in both x and x'. Since there is no standard definition of the emittance for such a beam distribution, the same properties as for the Gaussian beam were used, namely that the RMS particles have a position of $\sqrt{\beta\epsilon}$. In Fig. 5.28 the used beam distributions are shown.

The results of this tracking are shown as 2D maps in Figs. 5.29 - 5.31. Overall the difference in accuracy between the Gaussian and bar of charge distributions is fairly small, with the biggest absolute difference in error being 4 %. The accuracy in the α and β reconstruction is sometimes even better for the bar of charge case, while the emittance reconstruction is on average marginally worse and consistently over-estimating the emittance. This shows, that the analysis tool can also reliably

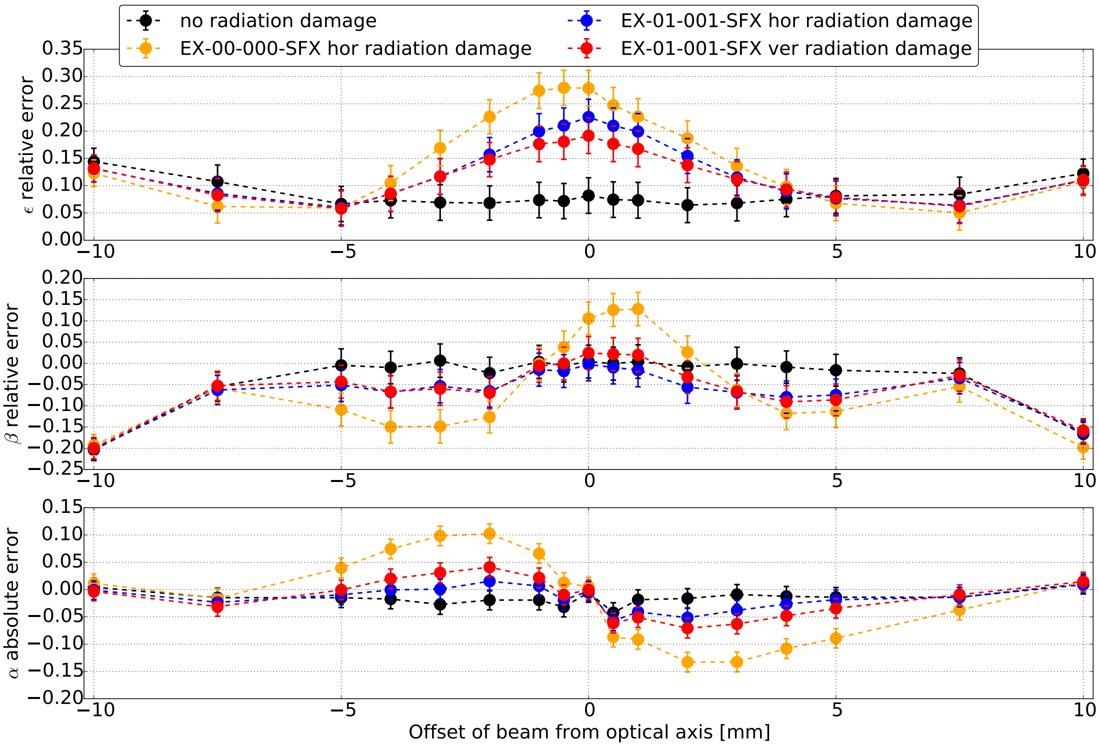

Figure 5.26: Error in the Twiss parameter reconstruction with and without radiation damage. The uncertainty shown is the result of the error propagation.

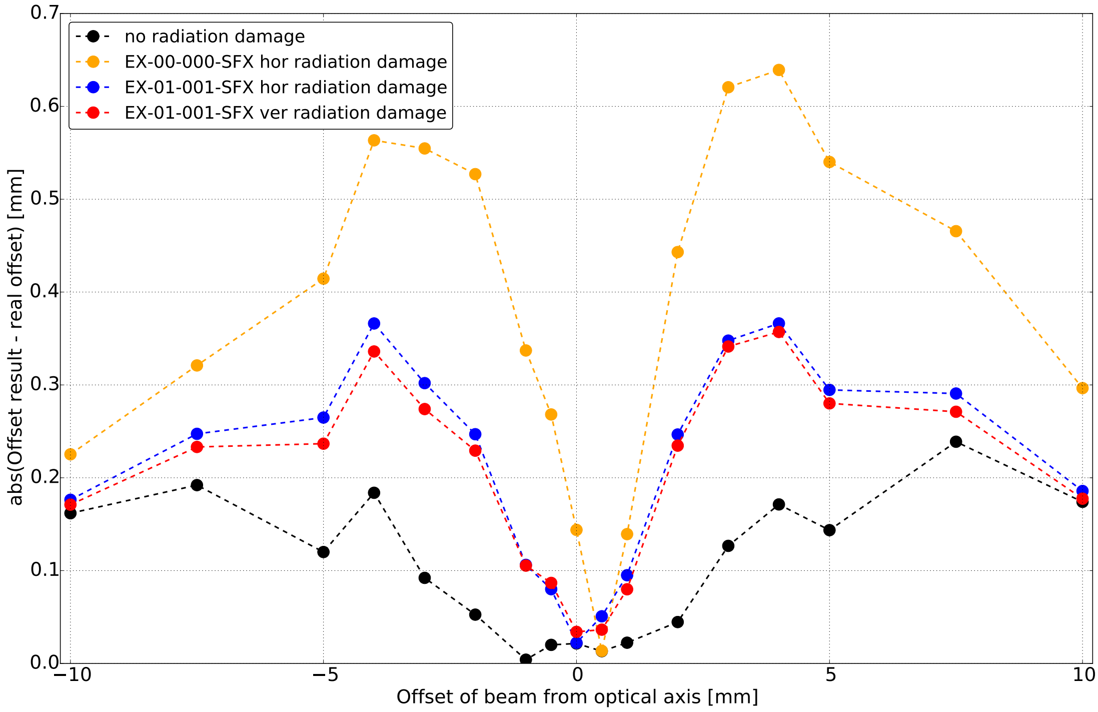

Figure 5.27: Absolute error in the beam offset reconstruction with and without radiation damage.

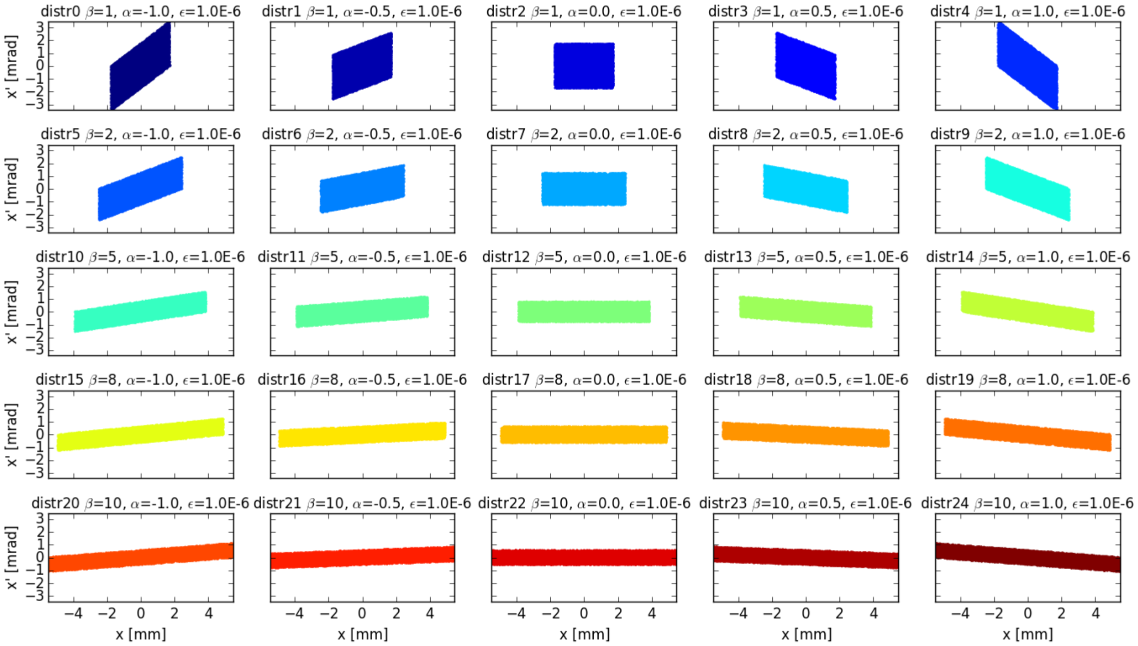

Figure 5.28: Tracked beam distributions for the bar of charge tests.

reconstruct the Twiss parameters for non-Gaussian distributions.

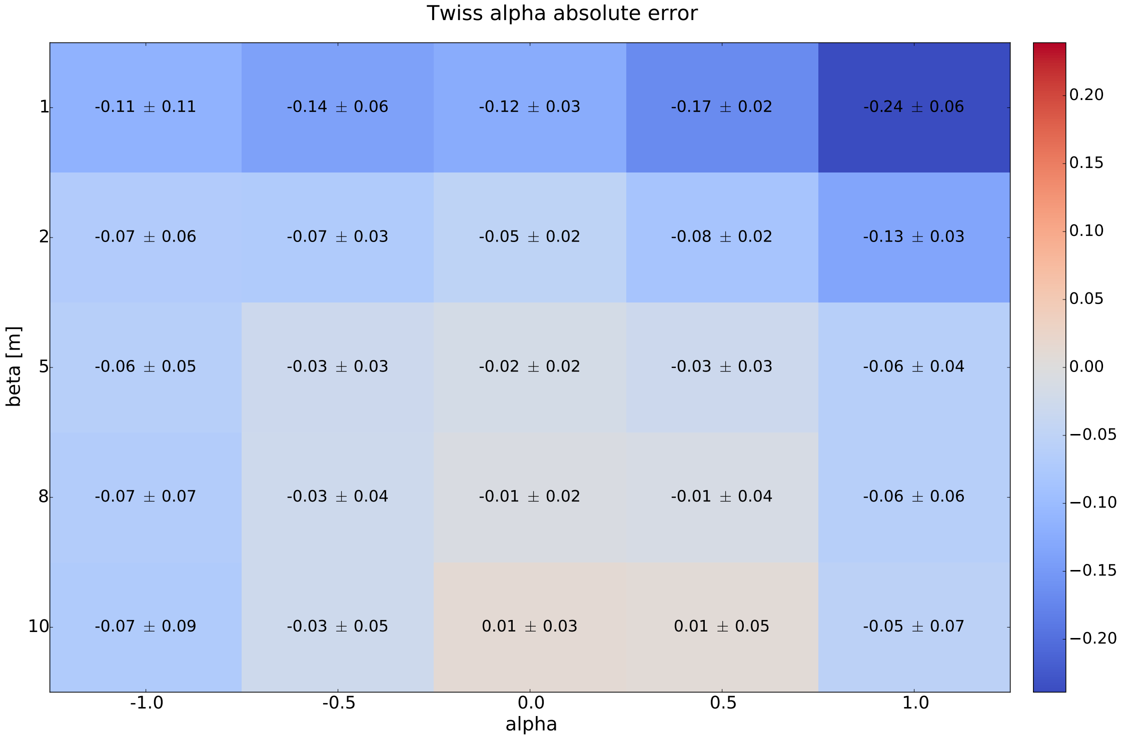

beta [m] \ alpha	-1.0	-0.5	0.0	0.5	1.0
1	-0.11 ± 0.11	-0.14 ± 0.06	-0.12 ± 0.03	-0.17 ± 0.02	-0.24 ± 0.06
2	-0.07 ± 0.06	-0.07 ± 0.03	-0.05 ± 0.02	-0.08 ± 0.02	-0.13 ± 0.03
5	-0.06 ± 0.05	-0.03 ± 0.03	-0.02 ± 0.02	-0.03 ± 0.03	-0.06 ± 0.04
8	-0.07 ± 0.07	-0.03 ± 0.04	-0.01 ± 0.02	-0.01 ± 0.04	-0.06 ± 0.06
10	-0.07 ± 0.09	-0.03 ± 0.05	0.01 ± 0.03	0.01 ± 0.05	-0.05 ± 0.07

Figure 5.29: Absolute error of the reconstructed Twiss α depending on the input beam distribution parameters, for bar of charge like distributions. The definition of a relative error does not make sense in this case, since α is also zero. The uncertainty shown is the result of the error propagation.

The real bar of charge distribution as it would be found in the extraction line does

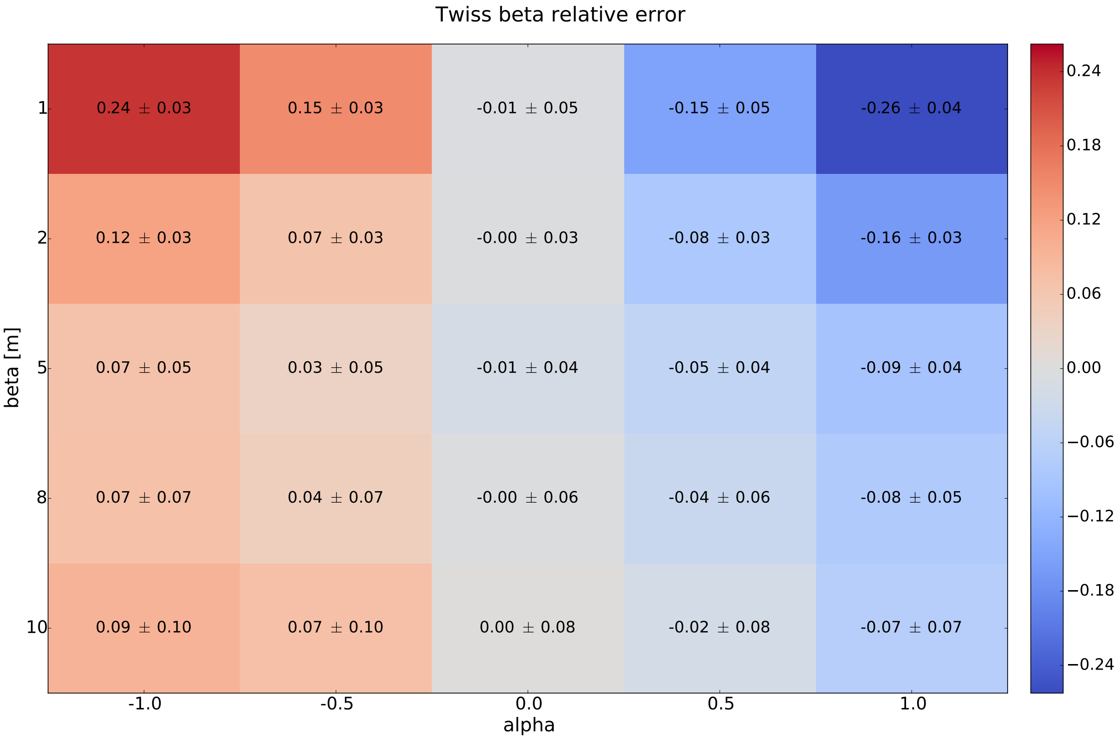

Figure 5.30: Relative error of the reconstructed Twiss β depending on the input beam distribution parameters, for bar of charge like distributions. The uncertainty shown is the result of the error propagation.

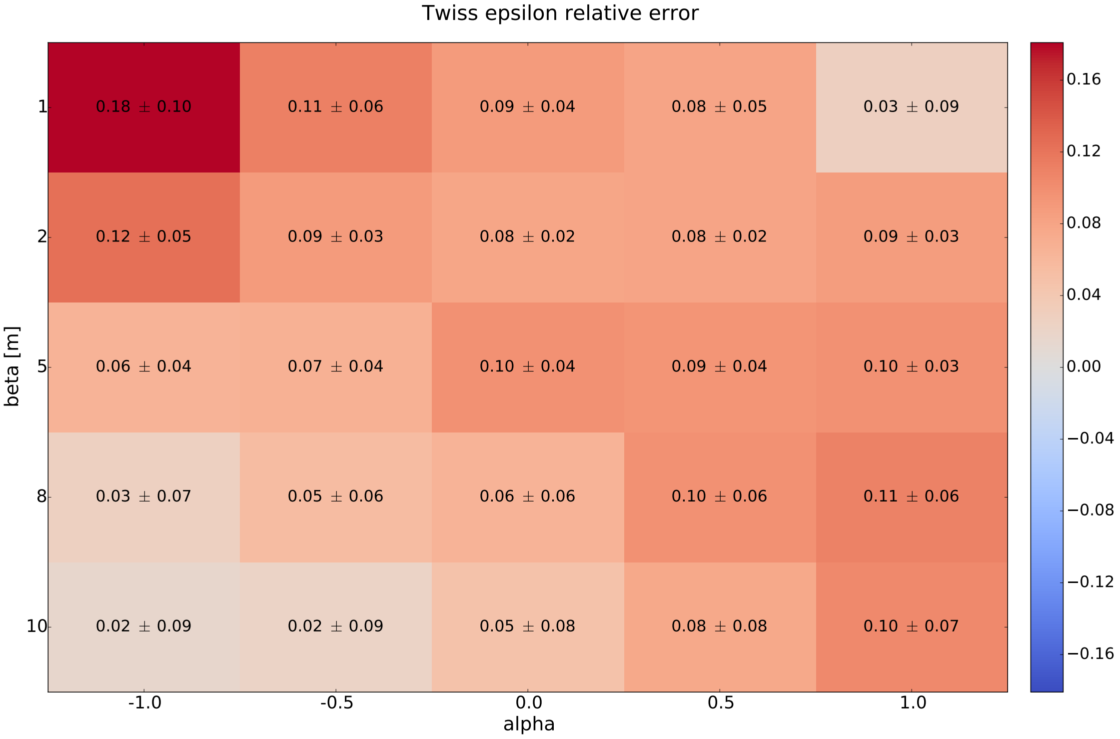

Figure 5.31: Relative error of the reconstructed Twiss ϵ depending on the input beam distribution parameters, for bar of charge like distributions. The uncertainty shown is the result of the error propagation.

however not really represent a 2D-uniform distribution. A more realistic bar of charge is shown in Fig. 5.32 (special thanks to Alexander Wastl for providing the distribution!) alongside with its reconstructed phase space ellipse. The computed ellipse fits the data quite well. Since there does not exist a definition of the emittance of the bar of charge (and therefore no *real* Twiss parameters of the distribution), no assessment of the reconstruction errors can be made.

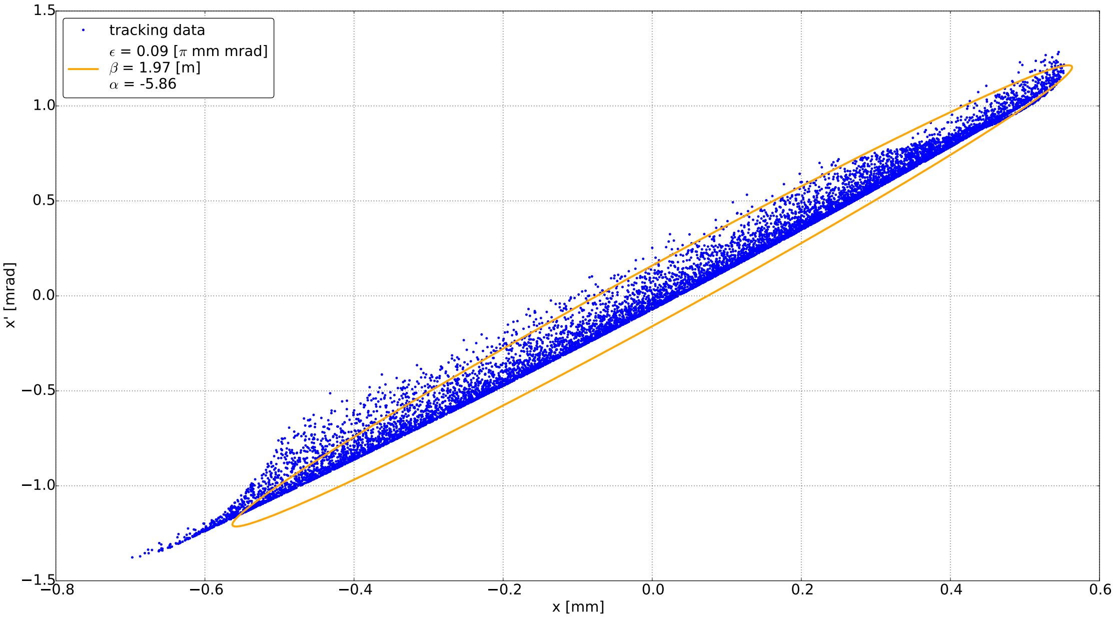

Figure 5.32: More realistic bar of charge distribution (result of a complete extraction particle tracking simulation) and the resulting phase space ellipse after simulating a quadrupole scan.

5.4.7 Visualization

After the analysis is performed by the tool, the raw data as well as the analysis result are presented to the user in an overview plot (an example of a 120 MeV/n carbon ion scan is shown in Fig. 5.33). The overview plot is divided into four subplots and an overview table.

The upper two subplots show the variance of the measured beam distributions as a function of the normalized quadrupole strength kl for the horizontal and vertical plane. The errorbars show the standard error calculated by the error propagation. If the curve fit worked, the resulting parabola is shown as well. The user can immediately judge if the scan was performed around the beam waist.

In the bottom two subplots the measured beam center is shown as a function of the normalized quadrupole strength, for both planes. Additionally the linear fit curve is shown as well.

The table on the right side shows information about the beam (the cycle code, energy and degrader), followed by the scanned quadrupole and the used beam monitor. Since the correct detection of the used quadrupole and monitor is essential for the calculation of the transfer matrix, this serves as a confirmation to the user, that the right elements were found. Underneath the results of the analysis are shown for both planes: geometric and normalized emittances, α, β and the offset of the beam from the quadrupole axis.

A second plot can also be produced which serves as an indication, how well the results fit to the measurements. It shows the phase space ellipse constructed with the analyzed Twiss parameters, as well as lines representing the width measurements.

Each beam size measurement can be represented as two vertical lines in the phase space at $\pm\sigma$, since it represents the projection of the beam distribution in phase space onto the position axis. A transformation of these lines back to the start of the quadrupole, using the inverted transfer matrix, results in the lines as depicted in Fig. 5.34.

If analysis results and measurement data fit perfectly (as shown with analytically simulated data in the left subplot of Fig. 5.34), all lines should be tangents to the reconstructed phase space ellipse. How well the Ellipse and the lines match, can serve as feedback to the user how well the scan was set-up and how accurate the analysis worked.

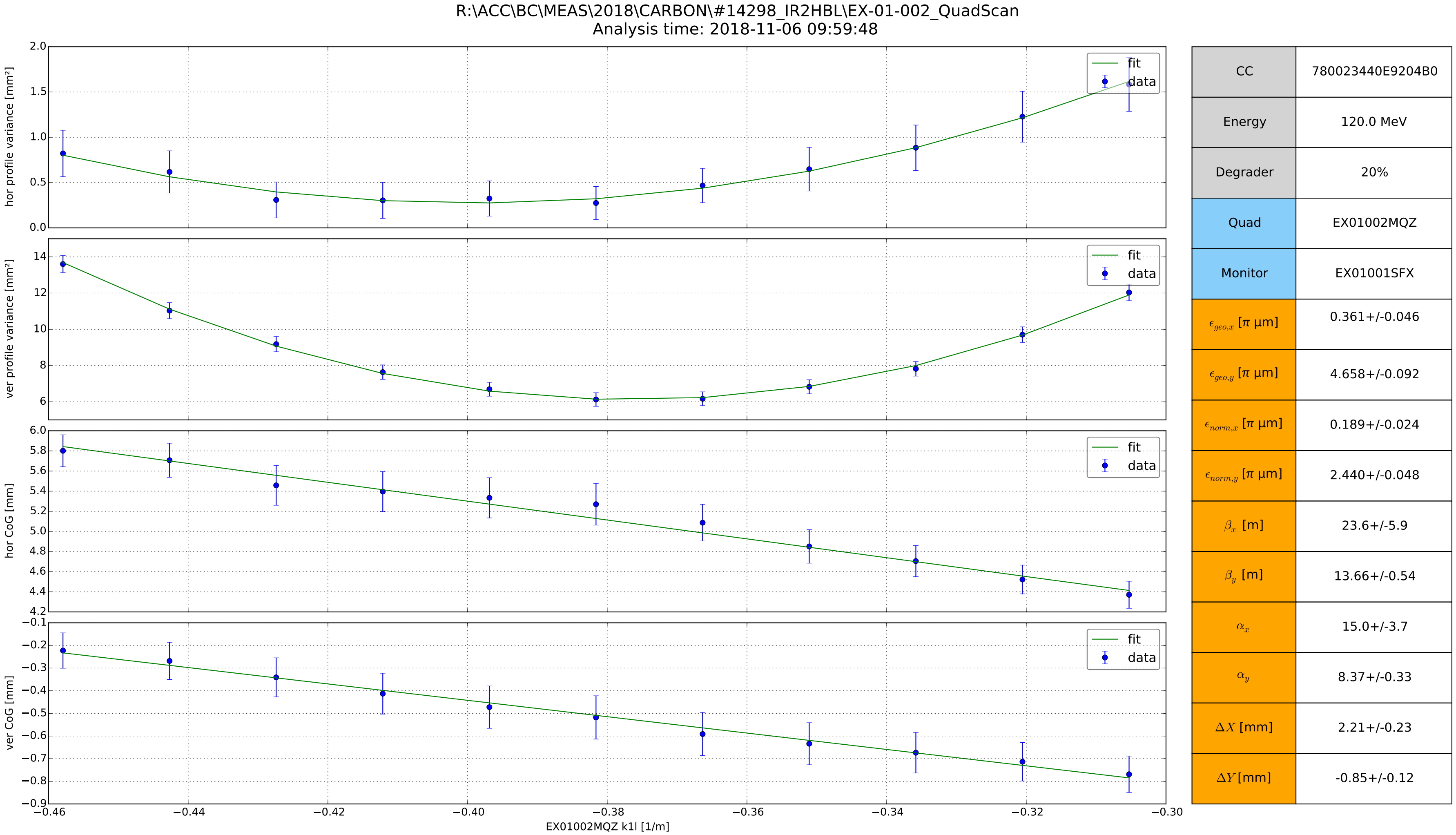

CC	780023440E9204B0
Energy	120.0 MeV
Degrader	20%
Quad	EX01002MQZ
Monitor	EX01001SFX
$\epsilon_{geo,x}$ [π µm]	0.361+/-0.046
$\epsilon_{geo,y}$ [π µm]	4.658+/-0.092
$\epsilon_{norm,x}$ [π µm]	0.189+/-0.024
$\epsilon_{norm,y}$ [π µm]	2.440+/-0.048
β_x [m]	23.6+/-5.9
β_y [m]	13.66+/-0.54
α_x	15.0+/-3.7
α_y	8.37+/-0.33
ΔX [mm]	2.21+/-0.23
ΔY [mm]	-0.85+/-0.12

Figure 5.33: Example of a summary plot produced by the `QuadScan.py` tool.

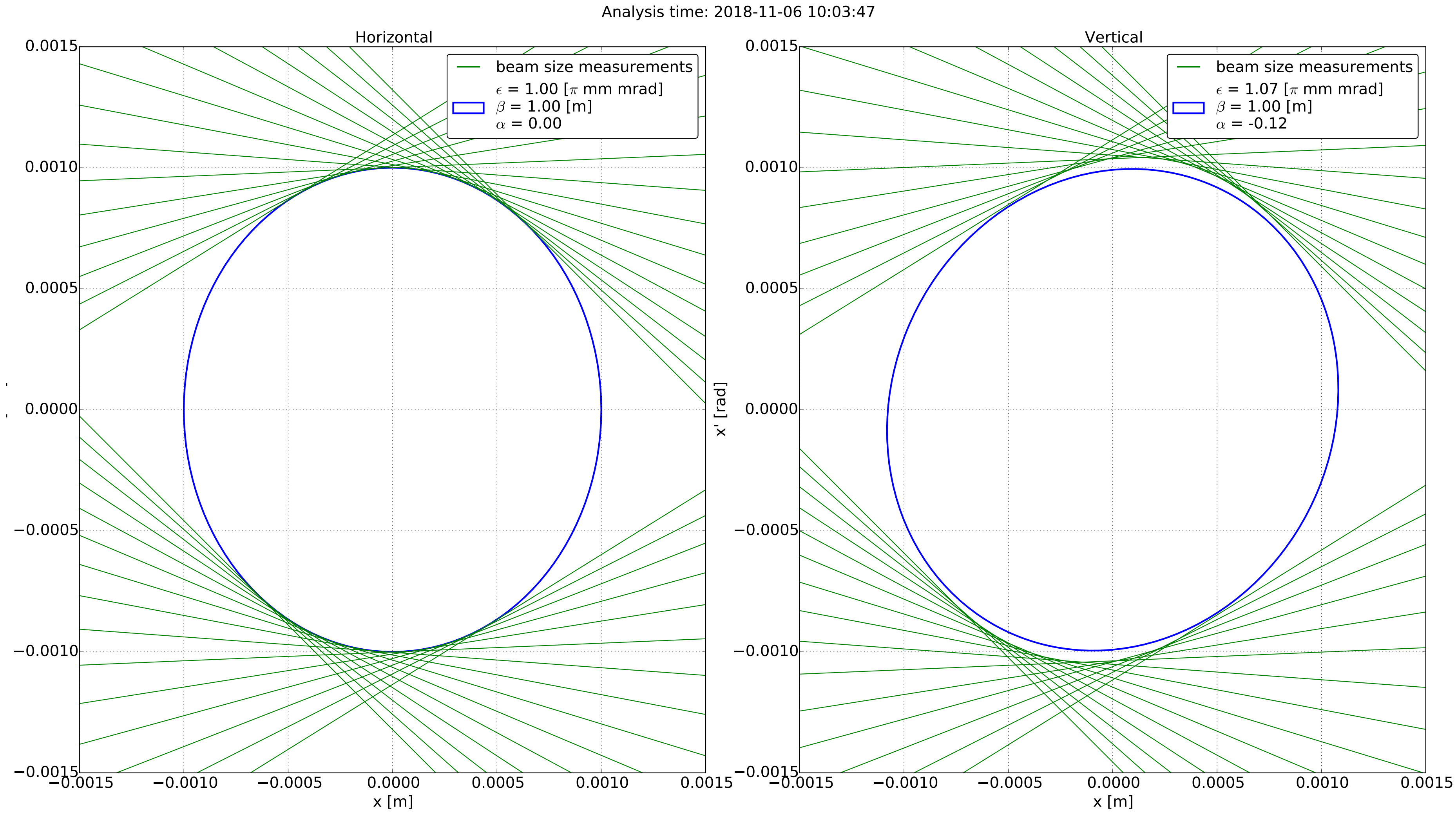

Figure 5.34: Example of a reconstructed RMS ellipse plot produced by the `QuadScan.py` tool. The horizontal plane depicts analytically simulated data with perfect matching and the vertical plane particles tracked with MADX.

5.5 Transmission analysis tool

To facilitate the easy transmission calculation of large amounts of beam current measurements, the PACMAN level three tool `Transmission.py` was developed during this thesis. Additionally, code for transmission analysis was also built into the analysis tool for daily quality assurance data, to allow the user to observe changes of the transmission values over time.

The transmission analysis tool automatically collects all current transformer data (CTA and CTS), analyzes the single measurements using the PACMAN level two `CTA.py` and `CTS.py` modules and groups the data according to the measured particle type, energy and degrader setting. Subsequently the average intensities as well as the single beam transmissions are calculated. The correlation which measurements are taken during the same accelerator cycle can be either done using the time stamp of the measurements or the unique *beamstamp* identifier.

An example of an output plot produced by the transmission analysis tool is shown in Fig. 5.35 for two degrader/particle/energy combinations. The tool can show an arbitrary number of combinations. The top subplot shows the average intensity through the LEBT, LINAC and MEBT current transformers as well as at the MR CTS at injection, flatbottom, flattop and the overall extracted intensity, calculated with the implemented RF train. The bottom subplot shows the average transmission between two consecutive intensity monitors. If the user is not interested in the transmissions between some of the monitors, or would for example rather have an overall transmission through several stages, the monitors can also be selectively added and removed.

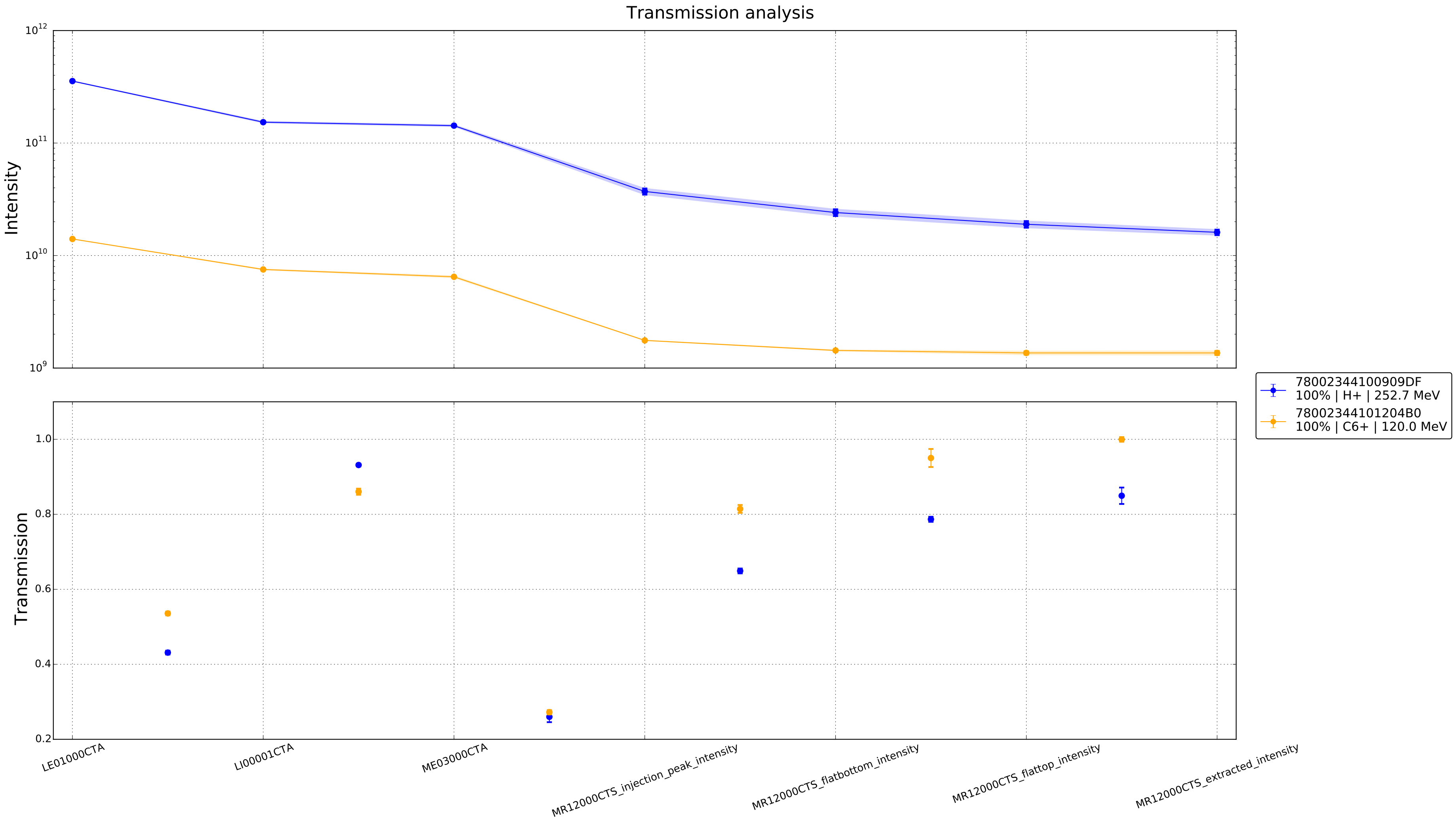

Figure 5.35: Example of the output plot produced by the `Transmission.py` module for a 252.7 MeV proton beam and a 120 MeV/n carbon ion beam, both at degrader setting 100 %.

6 Measurement results and conclusion

In this chapter the measurement analysis results obtained by the developed analysis tools and the `InjectorEmittance.py` module shall be presented, together with conclusions for the different developed tools and ideas for further improvement.

6.1 Injector emittance

The emittance of the two used sources (S1 and S2) was measured with the slit-grid method. Into the obtained phase-space distributions, the RMS ellipse was fitted using the `InjectorEmittance.py` module. The 90 % ellipse was calculated by enlarging the RMS ellipse by a factor of $\sqrt{-2\ln(0.1)} \approx 2.15$ (see eq. A.5). This is the number of standard deviations which would cover 90 % of the probability distribution when assuming a 2D Gaussian distribution. The complete derivation of this factor has been carried out in the appendix in Sec. A.3.

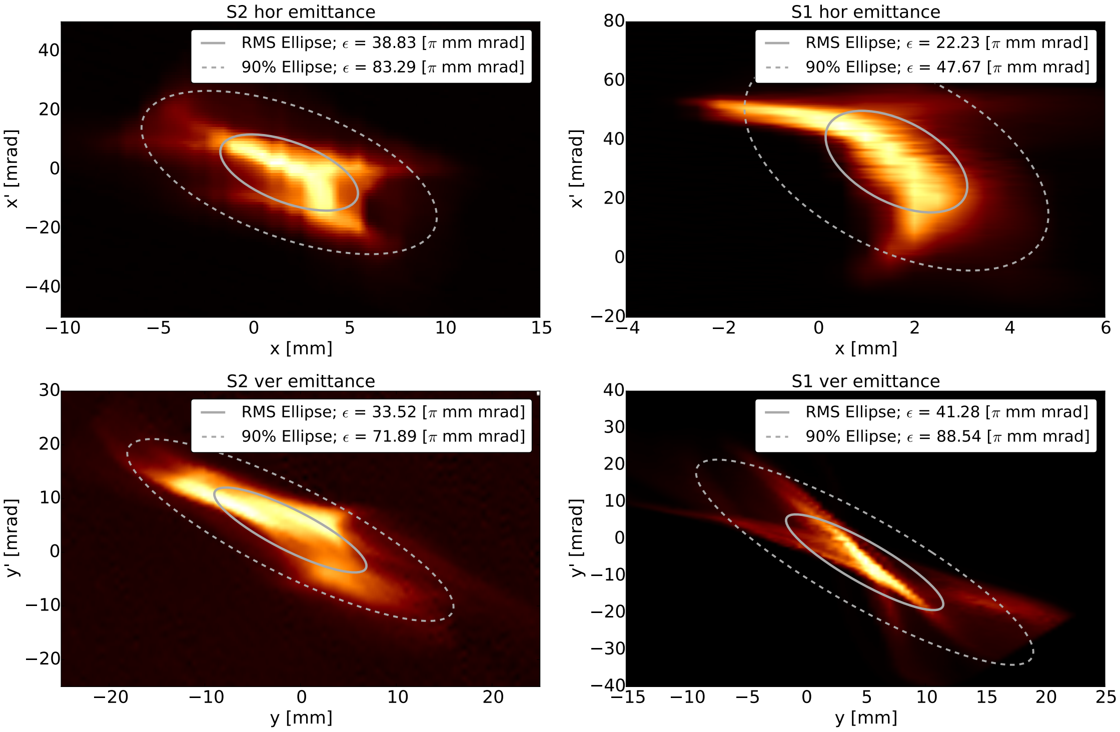

Figure 6.1: Phase space diagrams for Source 1 and Source 2 measured with the slit-grid method. The fitted RMS ellipse as well as the extrapolated 90 % ellipse are also shown.

In Table 6.1 the result for the 90 % geometric emittance are summarized. The requirement, as stated in Table 2.2, that more than 90 % of the beam fits within 180 π mm mrad is fulfilled for both sources in both planes.

Source	**90 % emittance [π mm mrad]**	
	H	V
S1	47.67	88.54
S2	83.29	71.89

Table 6.1: Slit-grid source emittance measurement results.

6.2 Synchrotron emittance

The developed analysis tool for the synchrotron emittance was used extensively during the commissioning of the carbon ion beam, as well as for repetitive quality assurance measurements of the proton beam.

All measurements presented in this section were taken with a scraper speed of 0.02 m/s, a scraping duration of 10 s and a manually set scraper plate start position of ±45 mm. The timing events used for the insertion of the scraper plates were *StartEVS*[1] for flattop measurements and *StopMultiturn*[2] for flatbottom measurements.

6.2.1 Protons

In Table 6.2 the results of the measurement analysis for the proton beam are shown. The measurements were performed for all degrader settings at the highest and lowest clinically used extraction energy as well as for flatbottom (7 MeV) with the exception of degrader 100 %, where the currently restricted range of the scraper was not sufficient for a proper measurement. The comparison to the design was performed against the normalized design emittance value of 0.519 π mm mrad.

When discussing the results, it should be noted that the machine settings differ between the clinically used degrader settings 10 % and 20 % and the two higher settings 50 % and 100 %.

For degrader 100 the horizontal emittance is significantly larger than for the other degrader settings which could be due to space charge effects: at higher intensities the repulsive forces that the particles exert on each other can lead to an increase of the emittance. Especially for the (compared to carbon ions) light protons this could play a significant role.

When we compare the change of the emittance from flatbottom to flattop between the horizontal and vertical plane, it can be seen that while the vertical flatbottom emittance is usually smaller, the vertical flattop emittance is overall considerably larger than the horizontal one. Additionally the vertical emittance increases from

---

[1] The EVS (energy verification system) is activated after the acceleration is finished and is therefore a suitable timing event for flattop measurements.

[2] This timing event marks the end of the multiturn injection procedure and is therefore a suitable timing event for flatbottom measurements. At this stage the beam has not yet been captured by the synchrotron RF cavity.

degrader	energy [MeV]	geometric H	geometric V	normalized H	normalized V	% of design H	% of design V
100 %	62	2.08	2.11	0.77	0.78	148	150
	252	1.57	1.40	1.23	1.09	236	210
50 %	7	12.98	7.22	1.59	0.88	-	-
	62	1.25	2.34	0.46	0.86	89	167
	252	0.85	1.25	0.66	0.97	128	188
20 %	7	13.96	5.88	1.71	0.72	-	-
	62	1.19	3.24	0.44	1.20	85	231
	252	0.65	1.35	0.51	1.05	98	203
10 %	7	12.86	7.90	1.57	0.97	-	-
	62	1.00	2.71	0.37	1.00	71	193
	252	0.60	1.62	0.47	1.27	90	244

Table 6.2: Synchrotron emittance measurement results (in π mm mrad) for the proton beam taken during extended quality assurance measurement sessions. The 7 MeV values represent flatbottom measurements.

flatbottom to flattop, which is counter intuitive since the emittance should actually decrease due to losses associated with the RF capture and the acceleration. In general, this hints at either a vertical instability or the crossing of a vertical tune resonance when going from injection to extraction tunes. For the proton beam it was confirmed to be a vertical instability due to measured vertical oscillations of the beam during the whole cycle.

6.2.2 Carbon ions

The measurements for the carbon ion beam, as summarized in Table 6.3, were taken during the commissioning phase. As for the proton beam, flatbottom measurements for degrader 100 % were not possible. The comparison to the design was performed against the normalized design emittance value of 0.7482 π mm mrad.

degrader	energy [MeV/n]	geometric H	geometric V	normalized H	normalized V	% of design H	% of design V
100 %	120	1.36	4.29	0.71	2.25	95	300
	400	0.56	2.08	0.57	2.13	76	284
20 %	7	16.11	5.82	1.97	0.71	-	-
	120	1.15	4.93	0.60	2.59	80	345
	400	0.53	2.29	0.54	2.34	72	313

Table 6.3: Synchrotron emittance measurement results (in π mm mrad) for the carbon ion beam taken during the commissioning phase.

After the commissioning of the multiturn injection for the carbon ion beam, the precise measurements of the synchrotron flattop emittance lead to the identification of unacceptable results in the vertical plane. This resulted in a recommissioning phase of the synchrotron setpoints to identify more suitable machine parameters.

If one compares the degrader 20 proton and carbon measurements, it can be seen that the normalized emittances at flatbottom and the horizontal emittance at flattop are very comparable between the two particle types. For the carbon beam however, the vertical emittance increases drastically during the acceleration. This hints again either at an instability, the crossing of a tune resonance line or a mismatch between the injector and the synchrotron during the multi-turn injection. An instability can be ruled out, since vertical oscillations of the beam could not be measured.

Scans of the injection and extraction tune settings were performed and a good new set point was found which leads to a decrease in the vertical emittance at the cost of a slight increase in horizontal emittance and a decrease in the flattop intensity in the synchrotron. The new measured emittances are shown in Table 6.4. The increase in the horizontal emittance actually led to the favorable situation that the emittance is approximately equal in both planes.

		geometric		**normalized**		**% of design**	
degrader	**energy [MeV/n]**	H	V	H	V	H	V
20 %	120	1.78	1.83	0.93	0.96	125	128
	400	0.80	0.88	0.82	0.90	109	120

Table 6.4: Synchrotron emittance measurement results (in π mm mrad) for the carbon ion beam after adapting the tune set-points.

6.2.3 Conclusion

The development of the synchrotron emittance measurement analysis module resulted in a very reliable tool, which allows the analysis of complex data with minimal required user input while still providing a lot of flexibility in the choice of analysis modes and parameters. Especially the choice to make the analysis not dependent on double-sided scraping, enables the use of partially incomplete data sets. It also allows the accumulation of a higher amount of measurement results, because the emittance value can be reconstructed from each single scraper sweep. The user-friendly analysis as well as the higher possible analysis yield make the analysis tool, besides it's use for commissioning tasks, also very attractive for repetitive quality assurance measurements to observe trends in the synchrotron emittance.

Extensive simulations led to a profound understanding of the behavior of the different analysis algorithms. It could be shown that the analysis tool can theoretically (without noise on the measured signal) reconstruct the emittance with relative errors of less than 0.5 %. These errors are very good also when compared to other synchrotron accelerators: comparison to the literature (Hunt et al. [28]) shows, that in other centers relative errors within 1 % for simulated data could be achieved. The presentation of the obtained results at the International Beam Instrumentation Conference 2018 in Shanghai to experts in the field generated very positive feedback and acknowledgement.

6.2.4 Outlook

The biggest room for improvement lies not in the analysis but rather in the measurement procedure itself. Especially the noise on the CTS signal leads to less reliable analysis results and reducing it could benefit the emittance reconstruction significantly. Additionally in the current set-up, the scraper plates do not move farther than the 0 mm mark (from their respective side). This results in the two obtained signals (as a function of the scraper position) having almost no overlap. Furthermore if the beam is considerably off-center one of the two scraping sweeps becomes unusable, because it does not cover the whole range. Upgrading the scrapers to extend over the 0 mm mark (for example to ±10 mm) would eliminate this problem and open new possibilities to upgrade the analysis tool. For example a combination of the two-sided and one-sided scraping analysis could be implemented, to perform a sanity check of the reconstructed emittance result directly inside the analysis tool.

The currently used values of the β-function to compute the emittance are the result of optics calculations. A measurement of the real β-function could be used to further increase the absolute accuracy of the emittance reconstruction, albeit not being necessary for comparative measurements.

To allow the complete automation of the analysis of repetitive measurements, additional functionality could be implemented into the PACMAN framework, to automatically detect that the given data stems from an emittance measurement and directly call the corresponding analysis tool.

6.3 HEBT emittance

The analysis tool for the quadrupole scans was extensively used during the carbon ion beam commissioning of the extraction line. The goal was to obtain the vertical Twiss parameters at certain locations of the transfer line and at a later stage based on those results calculate the necessary quadrupole strengths to achieve the desired spotsize of 6 mm at the isocenter.

The results are summarized in Tables 6.5 and 6.6. The huge uncertainty in the horizontal plane is due to the extremely small horizontal beam size at the monitor positions. Since this spotsize adjustment concept is anyway only used for the vertical plane, this large uncertainty is not at all concerning.

Before trying to adjust the spotsize, the obtained vertical Twiss parameters were tested for plausibility. This was done by calculating the expected beam sizes at several monitor positions with MADX, using the Twiss parameter results from the quadrupole scan as starting conditions and comparing them to actual measurements. The comparison is shown in Table 6.7 and shows an extremely good agreement between measured and calculated beam sizes. This confirms the accuracy of the analysis tool and the validity of the measurement results.

parameter	value	unit
$\epsilon_{geo,x}$	0.48 ± 0.48	π mm mrad
β_x	13.4 ± 8.6	m
α_x	6 ± 3.1	
$\epsilon_{geo,y}$	0.57 ± 0.29	π mm mrad
β_y	3.41 ± 0.87	m
α_y	-1.15 ± 0.23	

Table 6.5: Reconstructed Twiss parameters at the T2-01-000-MQZ for a 402.6 MeV/n carbon ion beam.

parameter	value	unit
$\epsilon_{geo,x}$	0.124 ± 0.055	π mm mrad
β_x	66 ± 30	m
α_x	26 ± 12	
$\epsilon_{geo,y}$	0.79 ± 0.11	π mm mrad
β_y	26.3 ± 4.2	m
α_y	-7.2 ± 1.1	

Table 6.6: Reconstructed Twiss parameters at the H2-00-001-MQZ for a 402.6 MeV/n carbon ion beam.

6.3.1 Conclusion

The developed `QuadScan.py` module provides a very robust tool for the analysis of quadrupole scans at any position of the transfer lines. The inclusion of a detailed error propagation calculation as well as direct visual feedback on how well the results fit the data, provide the user with all necessary tools to judge if the scan was performed in a proper manner and if the data can be trusted. The tool has already proven its usability, during the carbon ion beam commissioning of the extraction line, as well as in the analysis of repetitive quality assurance tests to measure the offset of the beam in the quadrupoles.

6.3.2 Outlook

A general improvement which could be made would be to implement the calculation of the transfer matrices into the PACMAN framework directly, to remove the need to use the `cpymad` package. The reason for that would be, that the installation of `cpymad` for new users usually proves very difficult and cumbersome. Since the gain of this would just be the removal of a one-time inconvenience, the necessity of this change is of low priority.

To give additional feedback about the set-up of the scan to the user, a test could be implemented, which checks if the scan was performed around the waist and throws a warning if not. Additionally an estimation on how the scanned quadrupole strength range should be adapted to cover the waist in both planes could be added

monitor	measured FWHM [mm]	expected FWHM [mm]
EX-02-001-SFX	6.4	6.42
T2-01-000-SFX	6.6	6.85
H2-00-000-SFX	9	9.12
H2-00-001-SFX	3.6	3.48
MF-03-200-DDM	4.8	4.87

Table 6.7: Measured vertical beam size (FWHM) at several key monitors in the IR2-H line compared to the expected result when propagating the Twiss parameters obtained by the quadrupole scans, showing very good agreement.

and presented to the user. The gain would be relatively minor, since the user can immediately see if the scan was performed around the waist and the estimation how to adapt the scan ranges can easily be performed by eye.

6.4 Transmission

The result for the transmission through the acceleration cycle, analyzed with the developed transmission analysis module are shown in Table 6.8. It can be seen, that for the carbon ions the transmission through the LINAC is approximately 50 % higher. Additionally the carbon ions show almost no losses during acceleration with transmission values consistently higher than 90 %.

particle	**energy**	**LINAC**	**deg. 20%**	**inj.**	**capt.**	**accel.**	**extr.**
H+	62	40	25	28	67	58	89
	148					65	93
	252					71	85
C6+	120	61	26	45	64	95	86
	268					95	89
	400					91	88

Table 6.8: Transmission values (in %) for protons and carbon ions of different extraction energies (in MeV/n). Shown are the transmission from the source through the LINAC, through the 20 % degrader and the fraction of injected, captured, accelerated and extracted beam intensity.

The transmission tool can also be used to determine the effective reduction in beam intensity by the different degrader settings. These values are important during the treatment planning. The results are summarized in Tables 6.9 and 6.10. At the MEBT CTA (which is the first current transformer after the degrader) there is no difference between protons and carbon ions. The effective degradation is consistently weaker than the nominal design setting. The clinically and patient safety relevant effective degradation at the CTS flattop level differs substantially between the two particle types. This is however not due to a fundamental difference at the degrader level but just a result of the different transmissions as shown in Table 6.8.

nominal setting	Proton	Carbon
50	65	66
20	25	26
10	14	15

Table 6.9: Effective degrader settings [%] for the proton and carbon ion beam at the MEBT CTA.

nominal setting	Proton	Carbon
50	41	64
20	27	34
10	9	18

Table 6.10: Effective degrader settings [%] for the proton and carbon ion beam at the MR CTS at flattop.

6.4.1 Conclusion

The developed `Transmission.py` module offers fast, reliable and easily accessible functionality to analyze the transmission for various data sets. It does not rely on all measurements being present, can deal with an arbitrary amount of measured beam configurations (cycle codes) and enables the user to freely combine various data sets to display them in one combined overview panel.

6.4.2 Outlook

The tool could be further improved by implementing higher level cycle code grouping options. Right now the data is grouped by degrader setting, particle type and energy. It could be beneficial to allow the user to freely choose by which cycle code parameters to group the data. Ideally this should be implemented generically at an underlying level in PACMAN to provide this functionality to multiple modules.

Furthermore, with the implementation of the SQL database for daily quality assurance data, additional methods could be implemented to calculate the transmission directly and store it in the database to save repetitive computation time further down the line.

Bibliography

[1] H. Wiedemann, *Particle Accelerator Physics*, 3rd ed. Springer, 2007.

[2] S. Y. Lee, *Accelerator Physics*, 2nd ed. World Scientific, 2004.

[3] P. J. Bryant and K. Johnsen, *The Principles of Circular Accelerators and Storage Rings.* Cambridge University Press, 1993.

[4] H. Grote and F. Schmidt, *The MAD-X Program*, European laboratory for particle physics.

[5] B. Holzer, "Transverse linear beam dynamics," CAS CERN Accelerator School, October 2016, last accessed: 2018-05-15. [Online]. Available: https://cas.web.cern.ch/schools/budapest-2016

[6] P. Bryant, L. Badano, M. Benedikt, M. Crescenti, P. Holy, A. Maier, M. Pullia, and S. Rossi, "Proton-ion medical machine study (PIMMS) part 1," CERN - PS Division, Tech. Rep., 1999.

[7] J. Buon, "Beam phase space and emittance," in *Proceedings to CAS, CERN Accelerator School Fifth General Accelerator Physics Course 1992*, S. Turner, Ed. CERN, 1994, pp. 89–115.

[8] U. Amaldi and G. Magrin, *The path to the Italian national centre for ion therapy.* TERA foundation, 2010, ISBN: 978-88-95522-44-9.

[9] "Product definition requirement specification MAPTA (level 1)," MedAustron, Tech. Rep., 2 2017.

[10] C. Lyneis, "ECR ion sources for accelerators," in *Proceedings of the 13th International Conference on Cyclotrons and their Applications, Vancouver, Canada.* World Scientific Publishing, 1992, pp. 301–307.

[11] E. Sargsyan, "Medaustron injector design report," MedAustron, Tech. Rep. 1.0, 2010.

[12] Y. Iwata *et al.*, "Alternating-phase-focused IH-DTL for an injector of heavy-ion medical accelerators," *Nuclear Instruments and Methods in Physics Research A*, vol. 569, pp. 685–696, 2006.

[13] P. Bryant and U. Dorda, "Medaustron MEBT design report," MedAustron, Tech. Rep. 1.1, 2010.

[14] U. Dorda and P. Bryant, "Medaustron synchrotron design report," MedAustron, Tech. Rep. 1.1, 2010.

[15] F. Osmic *et al.*, "Overview of the beam diagnostics in the medaustron accelerator: design choices and test beam commissioning," in *Proceedings of IPAC 2012, New Orleans, LA, USA.* CERN, 2012, pp. 774–776, paper MOPR002.

[16] P. Forck, “Lecture notes on beam instrumentation and diagnostics,” *Joint University Accelerator School*, 2007.

[17] S. Giordanengo *et al.*, “Design and characterization of the beam monitor detectors of the italian national center of oncological hadron-therapy (CNAO),” *Nuclear Instruments and Methods in Physics Research A*, vol. 698, pp. 202–207, 2013.

[18] U. Raich, “Emittance measurements,” USPAS and University of New Mexico, June 2009, last accessed: 2018-04-23. [Online]. Available: http://uspas.fnal.gov/materials/09UNM/Emittance.pdf

[19] C. Carli, A. Jansson, M. Lindroos, and H. Schönauer, “A comparative study of profile and scraping methods for emittance measurements in the PS Booster,” *Part. Accel.*, vol. 62, pp. 255–277, 2000.

[20] H. Schönauer, “BEAMSCOPE physics considerations, implementation and results of tests,” CERN, Tech. Rep., 1982.

[21] A. Wastl *et al.*, “PACMAN - the MedAustron measurement data analysis framework,” in *Proceedings of IPAC 2016, Busan, Korea.* CERN, 2016, paper WEPOR45.

[22] A. Kerschbaum, “Development and Implementation of a new Emittance Analysis Application for the MedAustron Injector Complex,” MedAustron, Tech. Rep., 2018.

[23] L. Adler *et al.*, “Synchrotron emittance analysis procedure at MedAustron,” in *Proceedings of IBIC 2018, Shanghai, China*, 2018, paper WEPC02, to be published.

[24] python. Last accessed: 2018-10-24. [Online]. Available: https://www.python.org

[25] scipy. Last accessed: 2018-10-24. [Online]. Available: https://www.scipy.org

[26] cpymad. Last accessed: 2018-10-24. [Online]. Available: https://pypi.org/project/cpymad

[27] H. Jivan, J. Mdhluli, E. Sideras-Haddad, B. Mellado, R. Erasmus, and M. Madhuku, “Radiation damage effects on the optical properties of plastic scintillators,” *Nuclear Instruments and Methods in Physics Research B*, vol. 409, pp. 224–228, 2017.

[28] J. Hunt, J. Resta-Lopez, C. Welsch, and C. Carli, “A new method for emittance reconstruction using a scraper in a dispersive region of a low energy storage ring,” in *Proceedings of IPAC2017, Copenhagen, Denmark.* CERN, 2017, pp. 429–432.

Appendix A

A.1 Intrinsic resolution of a scraping measurement

When a scraper starts slicing the beam distribution, it takes several turns for all particles to hit the plate. Due to the scraper plate moving during that time, the betatron amplitudes of the particles appear to be "smeared out" over the distance x_{max} the scraper moves during the maximum number of needed turns for complete scraping n_{max}.

For a fractional tune of $q = \frac{1}{3}$ (which would be unstable in reality) this leads to the unfortunate situation depicted in Fig. A.1, where the particles return to the same position in phase space every three turns. For the angle after n turns ϕ_n the following applies:

$$\cos(\phi_n) = \frac{r - nd}{r} = 1 - \frac{x}{r}$$

with the betatron amplitude r and the advance of the scraper per turn d. For the case of fractional tunes the maximum angle until all particles have been scraped is:

$$2\phi_{max} = 2\pi q = \frac{2\pi}{3}$$

and from that follows:

$$\begin{aligned} 1 - \frac{x_{max}}{r} &= \cos(\phi_{max}) = \cos(\pi/3) = \frac{1}{2} \\ \frac{x_{max}}{r} &= \frac{1}{2} \end{aligned}$$

This would result in a position uncertainty of the betatron amplitude of 50 %.

For non-resonant tunes, where the scraped parts do not overlap, it can be derived (please refer to the appendix of Schönauer [20] for the very lengthy derivation) that the uncertainty can be expressed as

$$\frac{x_{max}}{r} = \frac{1}{2}\left(\frac{3\pi d}{r}\right)^{2/3}$$

For this formula to be valid, the fractional part of the tune must be sufficiently far away from any resonance M/N (where N $<$ 10). This is expressed as an inequality for the difference δ of the tune from the closest resonance:

$$\delta > \frac{\left(3\pi\frac{d}{r}\right)^{1/3}}{\pi N}$$

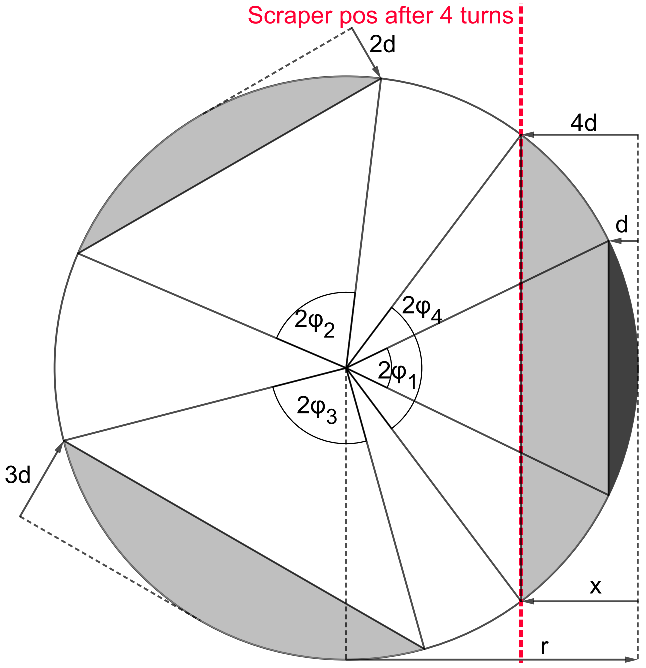

Figure A.1: The colored areas show the portion of the phase space that is scraped after 1, 2, 3 and 4 turns, with a scraper advance of d/turn. The scraper advance per turn is depicted unrealistically large for better illustration.

A.2 Error propagation for profile measurements

To estimate the uncertainty (standard error) σ_f of a function $f(x_1, x_2, ..., x_N)$ which is a function of variables x_i with their individual uncertainties σ_i, Gaussian error propagation can be used. In the case of independent variables (no correlation) and small errors σ_i (the linear approximation of f has to be close to f inside a neighborhood of radius $\sigma_1, \sigma_2, ..., \sigma_N$) the standard error of f can be calculated as:

$$\sigma_f = \sqrt{\sum_i \left(\frac{\partial f}{\partial x_i}\right)^2 \sigma_i^2} \tag{A.1}$$

A.2.1 Uncertainty of a binned measurement

A measurement with a profile monitor (such as an SFX) is equal to a binning (with a bin width h equal to the wire spacing of the monitor) of the continuous positional distribution of the beam. To estimate the uncertainty of the measured position introduced by the non-continuous binning the following estimation can be used: the binning introduces a position uncertainty in the interval of $[-h/2; +h/2]$ around the center of the bin. If one assumes that the real position is uniformly distributed on that interval with a probability function of the form:

$$p(x) = \begin{cases} 0, & \text{if} \quad x < -\frac{h}{2} \\ \frac{1}{h}, & \text{if} \quad -\frac{h}{2} \leq x \leq \frac{h}{2} \\ 0, & \text{if} \quad x > -\frac{h}{2} \end{cases}$$

Then the uncertainty on each bin is equal to the standard deviation of this distribution:

$$\sigma_x^2 = \int_{-\infty}^{+\infty} (x-\mu)^2 f(x) dx = \int_{-h/2}^{+h/2} \frac{x^2}{h} dx = \frac{h^2}{12}$$

$$\sigma_x = \frac{h}{\sqrt{12}} \tag{A.2}$$

A.2.2 Error on the mean

Let x_i be the wire positions of the profile monitor and w_i the measured counts on each wire with uncertainties in the position σ_{x_i} and in intensity σ_{w_i}. The weighted mean is calculated as:

$$m = \frac{1}{\sum_i w_i} \sum_i w_i x_i$$

According to Eq. A.1 the standard error can be calculated as:

$$\begin{aligned}
\sigma_m &= \sqrt{\sum_i \left(\frac{\partial m}{\partial x_i} \underbrace{\sigma_{x_i}}_{\text{Eq. A.2}}\right)^2 + \cancel{\sum_i \left(\frac{\partial m}{\partial w_i} \underbrace{\sigma_{w_i}}_{\text{negligible}}\right)^2}} \\
\sigma_m &= \sigma_x \sqrt{\sum_i \left(\frac{\partial f}{\partial_{x_i}}\right)^2} \\
\sigma_m^2 &= \frac{\sigma_x^2}{\left(\sum_i w_i\right)^2} \sum_j \left(\frac{\partial \left(\sum_i w_i x_i\right)}{\partial x_j}\right)^2 \\
\sigma_m^2 &= \sigma_x^2 \frac{\sum_i w_i^2}{\left(\sum_i w_i\right)^2} \\
\sigma_m &= \sigma_x \sqrt{\frac{\sum_i w_i^2}{\left(\sum_i w_i\right)^2}} \qquad \text{(A.3)}
\end{aligned}$$

A.2.3 Error on the variance

The variance and the error on the variance of the measured beam distribution can be calculated as:

$$v = \frac{1}{\sum_i w_i} \sum_i w_i (x_i - m)^2$$

$$\sigma_v = \sqrt{\underbrace{\sum_i \left(\frac{\partial v}{\partial x_i}\sigma_{x_i}\right)^2}_{1} + \underbrace{\left(\frac{\partial v}{\partial m}\sigma_m\right)^2}_{2} + \cancel{\sum_i \left(\frac{\partial v}{\partial w_i}\sigma_{w_i}\right)^2}}$$

$$1: \quad \sum_i \left(\frac{\partial v}{\partial x_i}\sigma_{x_i}\right)^2 = \frac{4\sigma_x^2}{\left(\sum_i w_i\right)^2} \sum_i w_i^2 (x_i - m)^2$$

$$2: \quad \left(\frac{\partial v}{\partial m}\sigma_m\right)^2 = \frac{4\sigma_m^2}{\left(\sum_i w_i\right)^2} \left(m \sum_i w_i - \sum_i w_i x_i\right)^2$$

$$\sigma_v = \frac{2}{\sum_i w_i} \sqrt{\sigma_x^2 \sum_i w_i^2 (x_i - m)^2 + \sigma_m^2 \left(m \sum_i w_i - \sum_i w_i x_i\right)^2} \tag{A.4}$$

A.3 2D-Gauss encircling radius

In this section the derivation of the radius, which covers a fraction p of the probability of a 2D Gaussian beam distribution, shall be presented.

A 2D Gaussian probability density function is defined as:

$$f(x, y) = \frac{1}{2\pi\sigma^2} e^{-\frac{x^2+y^2}{2\sigma^2}} dx dy$$

Transformation to polar coordinates:

$$f(r, \phi) = \frac{1}{2\pi\sigma^2} e^{-\frac{r^2}{2\sigma^2}} r dr d\phi$$

Integrate over ϕ:

$$f(r) = \int_{\phi=0}^{\phi=2\pi} \frac{1}{2\pi\sigma^2} e^{-\frac{r^2}{2\sigma^2}} r dr d\phi = \frac{r}{\sigma^2} e^{-\frac{r^2}{2\sigma^2}} dr$$

The covered fraction p is the integral over the probability density up to the corresponding radius r_p:

$$p = \int_0^{r_p} \frac{r}{\sigma^2} e^{-\frac{r^2}{2\sigma^2}} dr = 1 - e^{-\frac{r_p^2}{2\sigma^2}}$$

And finally we arrive at the radius r_p which covers the fraction p of the whole distribution:

$$r_p = \sqrt{-2\ln(1-p)}\sigma \tag{A.5}$$